THE MONTANA ALPS: KILOMETER-SCALE RECUMBENT FOLDING AND TECTONIC ATTENUATION IN THE ANACONDA RANGE, SOUTHWESTERN MONTANA

by

Bryce Alan Neal

A thesis submitted in partial fulfillment
of the requirements for the degree

of

Master of Science

in

Earth Sciences – Geology

MONTANA STATE UNIVERSITY
Bozeman, Montana

May 2022

DEDICATION

I dedicate this manuscript to all the people I’ve met in Bozeman who’ve seen me, changed me, and helped me better connect with myself, others, and the world at large. While this work is at best an attempt at understanding and is inherently limited by the vastness of the knowledge we have yet to acquire, I am proud of myself for having the courage to tell a story even when things felt fragmentary, uncertain, and even flat out wrong. I couldn’t have done this without all the support and love I’ve received from so many others over the past two years.

ACKNOWLEDGEMENTS

I would like to sincerely thank my advisor, Drew Laskowski, for his support and guidance throughout this project. I would also like to thank our colleagues Jeff Lonn, Colleen Elliot, and Katie McDonald at the Montana Bureau of Mines and Geology for their support of our EDMAP proposal and assistance during the field season. I am particularly grateful for email correspondence with Jeff Lonn, who's knowledge of regional geology and previous mapping in the Carpp Ridge 7.5' quadrangle were integral to synthesizing this complex field area. A major thanks is owed to field assistants Will Burrell, Mia Wafer, and Tia Goebel, who provided both good company in the field and fruitful discussion at puzzling outcrops. This is especially true for Will Burrell, who spent eight weeks during summer 2021 mapping very challenging terrain and accompanying me on some, in retrospect, inadvisable traverses. I am also very grateful for laboratory assistant Samantha Dittrich, whose meticulous work in the newly minted MSU zircon separation lab was an invaluable part of this project. A big thank you to committee members Devon Orme and Mary Hubbard for their thoughtful comments on this manuscript and assistance with petrographic analysis, geochronology, and microstructural interpretation. I would also like to acknowledge funding from the U.S. Geological Survey EDMAP program, the Geological Society of America, the Tobacco Root Geological Society, and NSF-EAR 2050246 for support of the Arizona LaserChron Center. Finally, I want to thank my current roommates for their encouragement over the past year and my family in Maine for their continued love and support.

TABLE OF CONTENTS

TABLE OF CONTENTS (CONTINUED)

LIST OF FIGURES

Figure Page

LIST OF FIGURES (CONTINUED)

Figure Page

CHAPTER ONE

GENERAL INTRODUCTION

Over a century since the foundational mapping of Emmons and Calkins (1913) in the Philipsburg 1:125,00 quadrangle of SW Montana, the complex geology of the Anaconda Range has continued to prove enigmatic. Situated in the exhumed footwall of the ~53 Ma Anaconda metamorphic core complex (AMCC) (O'Neill et al., 2004; Grice, 2006; Foster et al., 2010; Howlett et al., 2021), the core of the Anaconda Range contains ductiley deformed greenschist-upper amphibolite facies mid-crustal rocks interrupting an otherwise brittle fold-thrust belt system. While some workers (e.g. Lidke and Wallace, 1992; Wallace et al., 1992) have interpreted these rocks in terms of fold-thrust belt mechanics, more recent work (e.g. Lonn et al., 2003; Lonn and McDonald, 2004; Grice, 2006) has highlighted the pervasive nature of ductile deformation throughout the AMCC footwall. Mesoproterozoic Belt Supergroup-Paleozoic strata throughout the Anaconda Range have been severely attenuated by bedding-parallel ductile fabrics, and while the nature of this attenuation is certainly tectonic, the mechanisms behind it remain poorly constrained, especially in the western Anaconda Range outside of the ~75-74 Ma Lake of the Isle shear zone (LISZ) (Grice, 2006)

Out-of-sequence thrusting (Lidke and Wallace, 1992) and synorogenic extension (Lonn and McDonald, 2004) have been invoked to explain observed attenuation in the western Anaconda Range, however, both interpretations ignore pervasive, kilometer-scale recumbent folding documented throughout the region. First documented by Flood (1974) and in further detail by Wiswall (1976) and Wallace et al. (1992), the Fishtrap recumbent anticline (FRA) is a kilometer-scale, NW-verging recumbent fold spectacularly exposed in mountainsides throughout the west-central Anaconda Range. It is cored by the Prichard Formation and likely involves the entire Belt section exposed in this region. While the nature and geometry of the FRA remains controversial, especially considering its opposite vergence, it is clearly a similar-style fold with a thickened hinge zone and thinned limbs. Given the size of this structure, it stands to reason that the FRA could attenuate section at considerable scale. This idea could be easily tested by determining A) whether bedding-parallel ductile fabrics are axial planar to the fold and B) whether ductile fabrics are wrapped around its hinge. Further, the age of FRA-related deformation remains only somewhat well constrained, making it difficult to integrate this structure into regional tectonic models.

The Carpp Ridge 7.5’ quadrangle, located just south of Philipsburg, Montana, provides an excellent opportunity to study the relationship between attenuation and recumbent folding. Here, the Missoula Group has been thinned to ~230 meters compared to ~3000 meters east of the regionally extensive Georgetown-Philipsburg thrust system, and the FRA is well-exposed just south of the quadrangle. In this contribution, we hypothesize that Belt-Paleozoic strata in the Carpp Ridge area were attenuated on the upper limb of the FRA, and we present evidence to suggest bedding-parallel ductile fabrics are axial planar to the fold. Further, we present new U-Pb geochronology data from several Eocene-aged cross-cutting intrusions that suggest this deformation to be Late Cretaceous in age. Given our observations in the Carpp Ridge quadrangle, the FRA likely extends north of the extent mapped by Flood (1974) and Wallace et al. (1992), and is coaxial with tight, west-verging upright folds that, at least at the mesoscale, refold FRA-related ductile fabrics and may refold the larger-scale structure. The FRA could be continuous with the southern LISZ in the eastern Anaconda Range, which has been interpreted as a double gneiss dome comparable to those documented in the Aegean (Kruckenberg et al., 2011) and the French Massif Central (Rey et al., 2011) (Jeff Lonn, *pers. comm.*). NW-vergent recumbent folding may have accompanied isostasy/buoyancy driven doming of the middle crust during a phase of Late Cretaceous decompression documented throughout the Cordilleran hinterland. This process could have been driven by delamination of lithospheric mantle (Wells and Hoisch, 2008) or arc-root foundering (DeCelles et al., 2009; DeCelles and Graham, 2015) beneath an orogenic plateau (“Nevadaplano” of DeCelles, 2004) comparable to the modern Andean Altiplano-Puna plateau. We can only speculate on the tectonic processes that drove recumbent folding and gneiss doming in this region, and further work is needed to properly constrain the relationship between the FRA and the LISZ as well as the tectonic conditions under which both formed.

REFERENCES CITED

DeCelles, P. G., Ducea, M. N., Kapp, P., and Zandt, G., 2009, Cyclicity in Cordilleran orogenic systems: Nature Geoscience, v. 2, no. 4, p. 251-257.

DeCelles, P. G., and Graham, S. A., 2015, Cyclical processes in the North American Cordilleran orogenic system: Geology, v. 43, no. 6, p. 499-502.

Emmons, W. H., and Calkins, F. C., 1913, Geology and ore deposits of the Philipsburg quadrangle, Montana: U.S. Geological Survey Professional Paper 78, 300 p.

Flood, R. E., 1974, Structural geology of the upper Fishtrap Creek area, central Anaconda Range, Deer Lodge County, Montana: Missoula, University of Montana, M.S. thesis, 71 p., map scale 1:62,500.

Foster, D. A., Grice, W. C., Jr., and Kalakay, T. J., 2010, Extension of the Anaconda metamorphic core complex: 40Ar/39Ar thermochronology and implications for Eocene tectonics of the northern Rocky Mountains and the Boulder batholith: Lithosphere, v. 2, no. 4, p. 232-246.

Grice, W. C., Jr., 2006, Exhumation and cooling history of the Middle Eocene Anaconda metamorphic core complex, western Montana: Gainesville, University of Florida, M.S. thesis, 260 p., map scale 1:100,000.

Howlett, C. J., Reynolds, A. N., and Laskowski, A. K., 2021, Magmatism and Extension in the Anaconda Metamorphic Core Complex of Western Montana and Relation to Regional Tectonics: Tectonics, v. 40, no. 9.

Kruckenberg, S. C., Vanderhaeghe, O., Ferré, E. C., Teyssier, C., and Whitney, D. L., 2011, Flow of partially molten crust and the internal dynamics of a migmatite dome, Naxos, Greece: Tectonics, v. 30, no. 3.

Lidke, D. J., and Wallace, C. A., 1992, Rocks and structure of the north-central part of the Anaconda Range, Deer Lodge and Granite Counties, Montana: U.S. Geological Survey Bulletin 1993, 31 p., scale 1:24,000.

Lonn, J., and McDonald, C., 2004, Geologic map of the Kelly Lake 7.5' quadrangle, western Montana: Montana Bureau of Mines and Geology Open-File Report 500, 15 p., 1 sheet, scale 1:24,000.

Lonn, J. D., McDonald, C., Lewis, R. S., Kalakay, T. J., O'Neill, J. M., Berg, R. B., and Hargrave, P., 2003, Geologic map of the Philipsburg 30' x 60' quadrangle, western Montana: Montana Bureau of Mines and Geology Open-File Report 483, 1 sheet, scale 1:100,000.

O'Neill, J. M., Lonn, J. D., Lageson, D. R., and Kunk, M. J., 2004, Early Tertiary Anaconda Metamorphic Core Complex, southwestern Montana: Canadian Journal of Earth Sciences, v. 41, no. 1, p. 63-72.

Rey, P. F., Teyssier, C., Kruckenberg, S. C., and Whitney, D. L., 2011, Viscous collision in channel explains double domes in metamorphic core complexes: Geology, v. 39, no. 4, p. 387-390.

Wallace, C. A., Lidke, D. J., Elliott, J. E., Desmarais, N. R., Obradovich, J. D., Lopez, D. A., Zarske, S. E., Heise, B. A., Blaskowski, M. J., and Loen, J. S., 1992, Geologic map of the Anaconda-Pintlar wilderness and contiguous roadless area, Granite, Deer Lodge, Beaverhead, and Ravalli counties, western Montana: U.S. Geological Survey Miscellaneous Field Studies map MF-1633-C, 36 p., map scale 1:50,000.

Wells, M. L., and Hoisch, T. D., 2008, The role of mantle delamination in widespread Late Cretaceous extension and magmatism in the Cordilleran orogen, western United States: Geological Society of America Bulletin, v. 120, no. 5-6, p. 515-530.

Wiswall, C. G., 1976, Structural styles of the southern boundary of the Sapphire tectonic block, Anaconda-Pintlar Wilderness Area, Montana: Missoula, University of Montana, M.S. thesis, 62 p., map scale 1:48,000.

CHAPTER TWO

THE MONTANA ALPS: KILOMETER-SCALE RECUMBENT FOLDING AND TECTONIC ATTENUATION IN THE ANACONDA RANGE, SOUTHWESTERN MONTANA

Contributions of Authors and Co-Authors

Manuscript in Chapter 2

Author: Bryce A. Neal
Contributions: Conceptualization, Methodology, Field Mapping, Laboratory Analysis, Writing – Original Draft Preparation, Writing – Reviewing and Editing, Project Administration, Funding Acquisition.

Co-Author: Andrew K. Laskowski
Contributions: Supervision, Conceptualization, Methodology, Field Mapping, Writing – Reviewing and Editing, Project Administration, Funding Acquisition.

Co-Author: Jeffrey D. Lonn
Contributions: Conceptualization, Methodology, Previous Work, Regional Knowledge

Co-Author: William B. Burrell
Contributions: Field Mapping

Co-Author: Samantha R. Dittrich
Contributions: Laboratory Analysis

Manuscript Information Page

Bryce A. Neal[1], Andrew K. Laskowski[1], Jeffrey D. Lonn[2], William B. Burrell[1], Samantha R. Dittrich[1]

[1]Department of Earth Sciences, Montana State University, Bozeman, MT, United States
[2]Montana Bureau of Mines and Geology, Butte, MT, United States

Status of Manuscript:
__X_ Prepared for submission to a peer reviewed journal
___ Officially submitted to a peer reviewed journal
___ Accepted by a peer-reviewed journal
___ Published in a peer-reviewed journal

ABSTRACT

The Eocene Anaconda metamorphic core complex (AMCC) is the most recently documented metamorphic core complex in the North American Cordillera. While much work has focused on constraining the nature and timing of core complex extension, earlier deformation preserved in its footwall is not as well understood. The AMCC footwall contains an anomalously thin, mid-crustal section of Mesoproterozoic Belt Supergroup and Paleozoic strata. While the tectonic nature of this thinning is generally accepted, the mechanisms behind it remain enigmatic. Geologists from the Montana Bureau of Mines and Geology hypothesize that footwall strata were attenuated along the upper limb of the Fishtrap recumbent anticline (FRA), a kilometer-scale NW-verging recumbent fold exposed throughout the southwestern AMCC footwall. New geologic mapping in the Carpp Ridge 7.5' quadrangle and U-Pb geochronology better constrain the nature and timing of tectonic attenuation in this complex area. Two generations of folds deformed rocks in the quadrangle: F_1 recumbent folds with S_1 axial planar fabrics associated with the FRA, and F_2 upright folds with S_2 axial planar fabrics that refold the FRA. These deformations are likely Late Cretaceous in age based on dates from cross-cutting intrusions, although a foliation sub-parallel to S_1 in a 51.87 Ma granodiorite stock in the FRA hinge suggests localized Eocene deformation. Elsewhere in the field area, the same granodiorite crosscuts S_1 fabrics. F_1 folds and S_1 fabrics transpose, attenuate, and omit Belt strata in the southeastern portion of the quadrangle, suggesting that recumbent folding is intimately associated with tectonic attenuation. Further, west-vergent F_1 and F_2 folds may be decoupled from regional east-vergent tectonics and instead related to gneiss-doming in the ~75-74 Ma Lake of the Isle shear zone. Gneiss-doming and associated development of the FRA may have been driven by widespread decompression of the Cordilleran middle crust during Late Cretaceous time, perhaps in response to delamination of lithospheric mantle or arc-root foundering beneath the Cordilleran magmatic arc of SW Montana.

INTRODUCTION

Cordilleran metamorphic core complexes (MCCs) of western North America (Figure 1) represent focal points of high magnitude extension in the Earth's crust following prolonged Jurassic-Paleogene orogenesis (e.g. Davis and Coney, 1979; Crittenden et al., 1980; Wernicke, 1981). First recognized in the North American Cordillera, these features are characterized by domal uplifts consisting of a highly metamorphosed footwall, a mylonitic low-angle detachment fault, and an unmetamorphosed hanging wall (Coney et al., 1980). Exhumed footwall rocks of North American Cordilleran core complexes often record Mesozoic deformational histories that pre-date core complex extension, providing natural laboratories to study mid-crustal conditions in the hinterland (e.g. Platt et al., 2015; Wrobel et al., 2021). While much study has focused on the mechanics of core complex extension in this orogen, comparatively little work has been done on the nature and timing of pre-extensional footwall deformation related to orogenesis. Crustal thickening and magmatism associated with contraction pre-conditioned the Cordilleran crust for subsequent core complex extension and exhumation (e.g. Howlett et al., 2021; Wrobel et al., 2021), therefore, understanding pre-extensional footwall deformation is critical to 1) better understand mid-crustal behavior during orogenesis and 2) elucidate the processes that drive high-magnitude extension in orogens.

Previous studies of Cordilleran MCC footwalls have documented considerable ductile deformation, yet this has been explained in terms of both pre-core complex contraction and syn-core complex extension. In the footwall of Ruby-East Humboldt MCC of eastern Nevada, Maccready et al. (1997) documented several oppositely verging recumbent folds, one of which folds a synkinematic Eocene orthogneiss. They interpreted these folds as evidence of mid-crustal

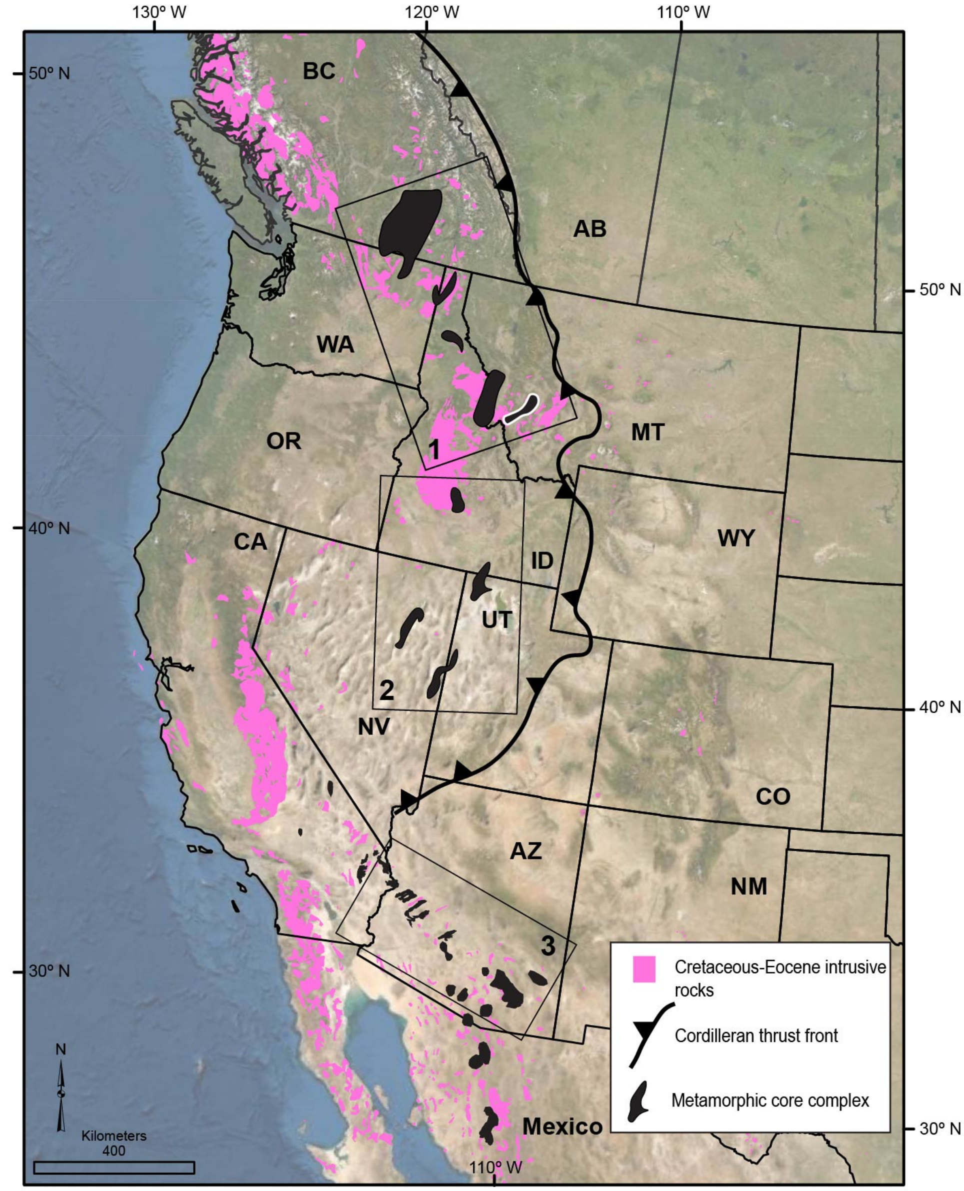

Figure 1: Tectonic map of the western United States modified from Howlett et al. (2020) showing distribution of metamorphic core complexes in relation to Cretaceous-Eocene intrusive rocks and the Cordilleran thrust front. MCC with white outline represents the Anaconda metamorphic core complex. Basemap is satellite imagery from Esri/NOAA.

flow beneath highly extended upper crust during Eocene-early Oligocene core complex extension. Also in the Ruby-East Humboldt MCC, Long and Kohn (2020) proposed that extremely attenuated and magmatically weakened footwall strata had undergone thrust sub-parallel distributed ductile thinning during a phase of Cretaceous decompression around ca. 85-60 Ma. Further, they proposed a kinematic link between thrust sub-parallel stretching in the Cordilleran hinterland and shortening in the Sevier fold-thrust belt. In the northern Snake Range MCC of eastern Nevada, mapping by Wrobel et al. (2021) revealed the presence of Late Cretaceous mid-crustal deformation, including regional scale recumbent folding and deep-seated thrusting that roughly coincided with burial and amphibolite facies metamorphism of footwall strata. The authors suggest that this phase of crustal thickening primed the northern Snake Range MCC for subsequent Cenozoic extension.

Many of the deformational features described above are present in the footwall of the Anaconda MCC (AMCC) of SW Montana, the most recently documented MCC in the North American Cordillera (Lonn et al., 2003; O'Neill et al., 2004) (Figure 1). Much like the Cordilleran core complexes described previously, most work in the AMCC has focused on determining the nature and timing of core complex extension (Grice, 2006; Foster et al., 2010; Howlett et al., 2020; Howlett et al., 2021), with less emphasis on pre-extensional deformation in the exhumed footwall. The AMCC footwall consists of a complexly deformed, highly metamorphosed, and extremely attenuated package of Mesoproterozoic Belt Supergroup, Paleozoic passive margin, and Mesozoic continental strata intruded by voluminous Cretaceous-Paleogene plutons. In total, the Belt Supergroup section exposed in the AMCC footwall is 4,000 meters thick compared to 6,100 meters west of the regionally extensive Georgetown-Philipsburg thrust system (Lonn et al., 2003). Further, strata of the Missoula Group have been thinned from ~3000 meters to ~60-500 meters in the same area (Emmons and Calkins, 1913; Poulter, 1956; Csejtey, 1968; Heise, 1983; Lonn and McDonald, 2004). Various hypotheses have been proposed to explain these discrepancies. In their foundational mapping of the Philipsburg 1:125,000 quadrangle, Emmons and Calkins (1913) related this thinning to erosion of the Missoula Group section and the development of a pre-middle Cambrian angular unconformity that cuts down-section to the east. Later mapping in the Anaconda-Pintler Wilderness Area by Lidke and Wallace (1992) and Wallace et al. (1992) identified several thin and incomplete sections of the upper, middle, and lower Missoula Group below the unconformity, indicating that erosion hypothesized by Emmons and Calkins (1913) did not cut very deep. Instead, the authors proposed that Missoula Group strata were tectonically attenuated by a series of out-of-sequence thrust faults that omit section, and that the pre-middle Cambrian unconformity was the result of tectonic dislocation rather than erosion. Re-mapping of the Philipsburg quadrangle by Lonn et al. (2003) and high resolution mapping in the Kelly Lake 7.5' quadrangle by Lonn and McDonald (2004) rejected the out-of-sequence thrusting hypothesis in favor of Cretaceous synorogenic extension. Lonn and McDonald (2004) reinterpreted the younger-over-older East Fork branch thrust of Lidke and Wallace (1992) and Wallace et al. (1992) as the Sawed Cabin detachment, a bedding-parallel low-angle normal fault that abruptly juxtaposes the Missoula Group over the underlying Piegan Group. This structure, as well as the broader Belt-Paleozoic section in the AMCC footwall, is characterized by bedding-parallel, pure-shear dominated ductile shear zones and bedding-parallel faults that omit section. Cross-cutting plutons constrain the age of this deformation to the Late Cretaceous, and thermochronologic studies by Desmarais (1983), Grice

(2006), and Foster et al. (2010) identify a Late Cretaceous exhumation event recorded in rocks of the western AMCC footwall. Lonn and McDonald (2004) speculate that the footwall section was attenuated and exhumed during extensional collapse of the Sevier hinterland, however, distributed ductile thinning in the style of Long and Kohn (2020) has also been proposed as a plausible mechanism (Jeff Lonn, *pers. comm.*).

More recently, geologists from the Montana Bureau of Mines and Geology have hypothesized that the AMCC footwall section was thinned along the upper limb of the Fishtrap recumbent anticline (FRA), an anomalous NW-verging recumbent fold visible in mountainsides throughout the west-central Anaconda Range (Jeff Lonn, *pers. comm.*). Mapping by Flood (1974) and Wiswall (1976) in the Warren Peak and Kelly Lake 7.5' quadrangles identified pervasive planar fabrics and mesoscopic folds related to the FRA. They hypothesized that the fold formed during Late Cretaceous contraction via gravitational sliding and frontal buttressing within the decollement zone of the Sapphire tectonic block of Hyndman et al. (1980), perhaps against an unexposed basement high. This inhibited eastward transport and resulted in the observed NW-vergence. Wallace et al. (1992) interpreted the FRA as a fold nappe formed via buttressing against a blind ramp they inferred to be beneath the nappe. Highly ductile rocks to the west and below the ramp lost their ability to transfer stress and movement to more competent rocks to the east and above the ramp, resulting in decoupled deformation at different structural levels. Continued movement of plastically deformed rocks up the ramp may have been accommodated by NW-vergent recumbent folding. The authors speculate that this ramp connects to the thrust-cored south-vergent Mill Creek nappe mapped by Emmons and Calkins (1913) and in more detail by Heise (1983) to the northeast on Mt. Haggin, just south of Anaconda, MT.

There has been no attempt in the literature to relate observed tectonic attenuation in the AMCC footwall to recumbent folding during contractional deformation, and we hypothesize that folding was the driving mechanism behind tectonic attenuation in this region. While folding is synonymous with structural thickening, similar folds are characterized by relative thinning of limbs and thickening of hinges (Ramsay, 1967). Both Flood (1974) and Wiswall (1976) documented mesoscopic similar folds in Belt strata associated with the FRA, so it would stand to reason that the structure could attenuate section at a much larger, perhaps even regional scale. Exposures of the fold axis and lower overturned limb in the southeastern Anaconda Range and another recumbent fold in the Flint Creek Range to the north have led some to speculate that the FRA is a structure of regional significance (Jeff Lonn, *pers comm.*). This idea could be tested by determining whether bedding-parallel attenuation fabrics are axial planar to the FRA, and whether these fabrics are wrapped around the hinge of the fold. Further, the timing of recumbent folding remains poorly constrained. In the Bitterroot lobe of the Idaho Batholith, Desmarais (1983) dated deformation observed in high-grade rocks of the Missoula and Piegan Groups as prior to and continuing through 78 Ma on the basis of U-Pb ages obtained from a foliated granodiorite. In the northeastern Anaconda Range, Grice (2006) used U-Pb ages from cross-cutting intrusions to date tectonic attenuation of high-grade Belt strata in the Lake of the Isle shear zone (LISZ) to 75-74 Ma. Further, Naibert et al. (2010) used $^{40}Ar/^{39}Ar$ and paleomagnetic data from the Philipsburg Batholith to determine that movement along the Georgetown thrust had ceased by 75 Ma. While cross-cutting intrusions in the west-central AMCC footwall have led many workers to believe that folding is associated with Late Cretaceous deformation discussed above, absolute ages of intrusions in this area are still unknown and their interactions with planar fabrics and other structures remain poorly documented. Developing a detailed chronology of these structures is critical to integrating the FRA into regional tectonic models.

The Carpp Ridge 7.5' quadrangle (Figure 2, 3), located in the west-central Anaconda Range just south of Philipsburg, MT, provides an ideal place to study deformation in the AMCC footwall. It is host to an extremely attenuated, ~230 meter thick Missoula Group section (Lonn and Lewis, 2009) in the footwall of the Georgetown thrust, and provides easy access to the northern half of the Warren Peak 7.5' quadrangle where the hinge of the FRA is spectacularly exposed. Much of the deformation in this area has been attributed to development of the Georgetown thrust and a series of NNE plunging upright folds, however, mesoscopic west-vergent folds in nearby quadrangles indicate that the FRA may extend north to Carpp Ridge. It is also host to numerous undated cross-cutting intrusions, which can provide detailed age constraints on deformation in the area. High-resolution geologic mapping in the Carpp Ridge quadrangle was conducted to test the connection between the FRA and observed tectonic attenuation in the Belt-Paleozoic section. Structural fabrics and the relationship between cross-cutting intrusions and fabrics were documented to develop a relative chronology of deformation in the area. Further, U-Pb geochronology was used to date several cross-cutting intrusions to better constrain the timing of deformation in the west-central Anaconda Range. Our results suggest that the Belt-Paleozoic section in Carpp Ridge was attenuated on the upper limb of the FRA during Late Cretaceous time, and that NW-vergent, kilometer-scale recumbent folding in the AMCC footwall may be related to gneiss-doming in the LISZ during a phase of Late Cretaceous decompression.

GEOLOGIC SETTING

The AMCC is situated within the Helena salient, a forelandward-convex bend in the North American Cordilleran retroarc fold-thrust belt inherited from the earlier Helena embayment of the Belt Supergroup (Harrison et al., 1974) (Figure 1, 2). This feature is bounded to the north by the Lewis and Clark line, a Proterozoic-Holocene zone of strike-slip, dip-slip, and oblique slip faulting extending from eastern Idaho to central Montana (Wallace et al., 1990), and to the south by the southwest Montana transverse zone, a Late Cretaceous-Paleogene zone of imbricated north-dipping oblique-slip faults that separates allochthonous rocks to the north from basement-involved thrust plates to the south (Schmidt and O'Neill, 1982, Structural evolution of the southwest Montana transverse zone. In: Blake, R. (Ed.), Geologic Studies of the Cordilleran Thrust Belt 1, Rocky Mountain Association of Geologists Field Guidebook, vol. 1, p. 193-218.; O'Neill et al., 1990). These two zones merge into the north-trending Lombard thrust, the principal thrust fault of the Helena salient. Sevier thrust-belt structures in this region were subsequently overprinted by both thick-skinned contractional and Cenozoic extensional tectonism.

The AMCC is characterized by an unmetamorphosed hanging wall, a mylonitic detachment fault, and a highly metamorphosed footwall (Figure 2). The hanging wall consists of detached blocks of Mesoproterozoic-Mesozoic rock covered by Cenozoic syntectonic clastic, volcaniclastic, and volcanic strata. (O'Neill et al., 2004; Foster et al., 2010). Mapping by Elliott and Lonn (in review) in the Long Peak 7.5' quadrangle just southeast of Carpp Ridge assigned clastic deposits of the Big Hole valley to the Miocene Sixmile Creek Formation. The detachment fault zone is east-dipping and consists of a broad zone of greenschist facies mylonites, cataclasite, and breccia from structurally lower to higher levels. Slip lineations documented in the Paleocene Pintler Creek Batholith near the detachment suggest that extension was likely NW-SE directed (Howlett et al., 2020). Further thermochronologic work by Foster et al. (2010)

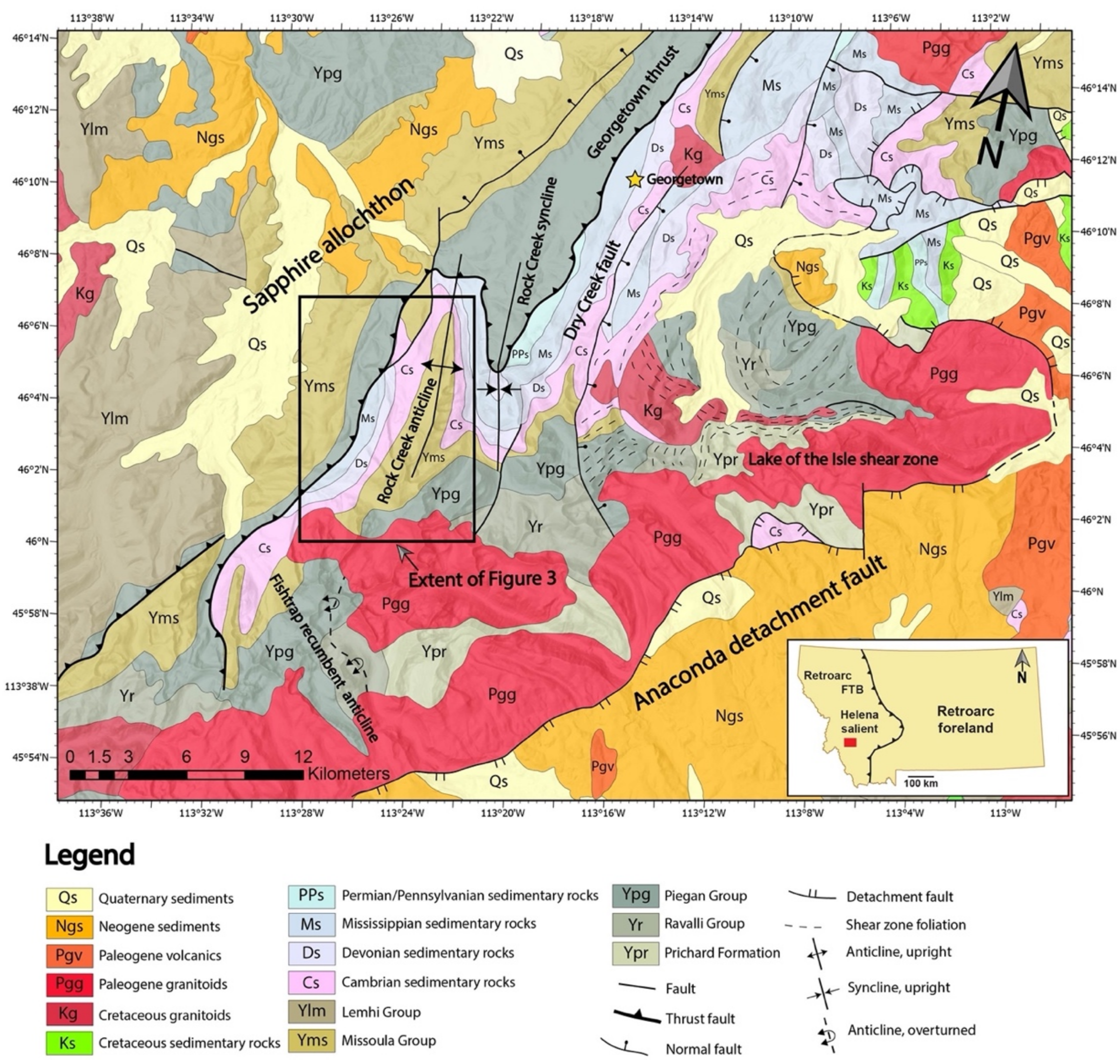

Figure 2: Regional geologic map of the AMCC footwall. Red rectangle in inset shows location of Figure 2 relative to major tectonic features of Montana. Black-outlined rectangle shows location of the Carpp Ridge 7.5' quadrangle. The footwall consists of complexly deformed Mesoproterozoic-Mesozoic metasedimentary strata intruded by Late Cretaceous-Eocene plutons. Abbreviations: FTB – fold-thrust belt. Bedrock geology data sourced from the Montana Bureau of Mines and Geology, Wallace et al. (1992), and Kalakay et al. (2014). Basemap and hillshade sourced from Esri/NOAA.

and Howlett et al. (2021) indicate that core complex extension likely began at 53 Ma and continued well into the Oligocene. Biotite $^{40}Ar/^{39}Ar$ cooling ages from rocks collected on an east-west transect across the AMCC footwall by Foster et al. (2010) young to the east and define an exhumed partial retention zone. They interpreted an ~53 Ma cooling age from a sample at the base of this partial retention zone as marking the onset of extension. Zircon (U-Th)/He thermal modeling by Howlett et al. (2021) further corroborated this finding, identifying a phase of rapid cooling from ~60-45 Ma associated with crystallization of the Pintler Creek batholith and initial exhumation along the Anaconda detachment, followed by a second phase of slower cooling from ~45-25 Ma associated with footwall unroofing. This extension was likely synchronous with the Bitterroot core complex to the west on the basis of similar cooling histories between the two, which has led some to suggest that the Anaconda and Bitterroot complexes are an integrated extensional system (Grice, 2006).

In the Anaconda and Flint Creek ranges, the footwall is characterized by complexly deformed Belt Supergroup, Paleozoic passive margin, and Lower Cretaceous continental strata. These rocks have been tectonically attenuated by bedding-parallel ductile shear zones and brittle faults that omit section, reducing the entire Belt Supergroup section to a thickness of <4000 meters (Lonn et al., 2003; Lonn and Lewis, 2009; Lonn and Johnson, 2010). In the eastern Anaconda Range, Grice (2006) documented considerable ductile attenuation, boudinage, and isoclinal folding of Belt and Paleozoic strata in the LISZ, which is 75-74 Ma based on dates from an ~75 Ma foliated quartz diorite dike and the cross-cutting ~74 Ma Storm Lake stock. In the western Anaconda Range, mapping by Lonn and McDonald (2004) in the Kelly Lake 7.5' quadrangle documented highly strained contacts between the Missoula and Piegan groups, as well as the Piegan and Ravalli groups. They interpreted the Missoula-Piegan contact as the Sawed Cabin detachment, a low-angle normal fault, based on complete omission of the Snowslip and Shepard formations. Similarly-strained Late Cretaceous plutons in the area mapped by Desmarais (1983) suggest that the Sawed Cabin detachment is Late Cretaceous in age. Attenuated footwall rocks are bound to the west by the >75 Ma Georgetown thrust, a regionally extensive structure that places Belt strata of the Sapphire allochthon over the Paleozoic section (Lonn et al., 2003; Naibert et al., 2010). The attenuated section and associated structures in the Anaconda and Flint Creek ranges are further folded by west-verging recumbent folds as well as a series of NNE plunging upright folds that fold the Georgetown thrust (Csejtey, 1968; Flood, 1974; Wiswall, 1976; Heise, 1983; Baken, 1984; Lidke and Wallace, 1992; Lonn et al., 2003). All aforementioned structures are cut by a series of northeast-striking high angle normal faults that offset middle to late Eocene intrusive rocks (Wallace et al., 1992).

Two phases of metamorphism have been recognized throughout the footwall of the AMCC and around the Idaho Batholith to the west: a Late Cretaceous prograde dynamothermal event related to observed deformation and a subsequent thermal event associated with the intrusion of Late Cretaceous-Eocene plutons. West of the Georgetown thrust, in the Bitterroot lobe of the Idaho Batholith, Desmarais (1983) documented sillimanite-grade assemblages in highly foliated metasedimentary rocks of the Belt Supergroup. A northwest striking foliation concordant to wall-rocks was also observed in a granodiorite suite dated to 78 Ma (Desmarais, 1983). In the west-central Anaconda Range, Flood (1974) observed amphibolite facies assemblages in Belt metapelites and calc-silicates, which were determined to have formed at temperatures and pressures around 550º-650º C and 2-4 kilobars. In the LISZ, Grice (2006) documented sillimanite-grade, middle-upper amphibolite facies assemblages in highly foliated metasedimentary rocks of the Belt and Paleozoic sections. This phase of metamorphism was determined to be coincident with 75-74 Ma shear zone development, and likely took place at temperatures and pressures around 750º-825ºC and 3.2-5.3 kilobars. Earlier kyanite-bearing assemblages were also documented, perhaps related to a Barrovian-type dynamothermal event associated with tectonic loading during Late Cretaceous thrusting. Similar kyanite-bearing assemblages have also been observed in Cretaceous metasedimentary rocks of the Flint Creek range (Buckley, 1990). These rocks are further overprinted by greenschist facies mylonites of the Anaconda detachment. Relative to the detachment, footwall prograde metamorphism appears to increase from west to east. West of the Georgetown thrust, on the eastern edge of the Sapphire allochthon, strata have been metamorphosed to greenschist facies (Lonn et al., 2003). Subsequent contact metamorphism associated with Late Cretaceous-Eocene plutons in the Anaconda and Flint Creek ranges is generally restricted to small contact aureoles, and likely occurred at temperatures and pressures around 550º-700ºC and 1-3 kb (Wallace et al., 1992).

Voluminous magmatism affected the Anaconda and Flint Creek ranges during Late Cretaceous-Eocene time. The Cretaceous phase was coincident with inboard migration of the Cordilleran magmatic arc into the retroarc fold-thrust belt, resulting in fault-controlled emplacement of notable SW Montana intrusive suites such as the Boulder and Pioneer batholiths (Kalakay et al., 2001; Lageson et al., 2001). In the Flint Creek Range, this magmatism is represented by the granodioritic-monzogranitic Philipsburg Batholith, Mt. Powell Batholith, and Royal Stock in the footwall of the AMCC (Allen, 1966; Csejtey, 1968; Lonn et al., 2003; Elliott et al., 2013). Two K-Ar dates of 76.7 and 74.0 Ma for the Philipsburg Batholith were calculated by Hyndman et al. (1972), and an $^{40}Ar/^{39}Ar$ age of 74.77 Ma was calculated by Naibert et al. (2010). Fission track dates for the Royal Stock and Mt. Powell Batholith were calculated by Baty (1973) to 66.4 and 62.1 Ma respectively. Naibert et al. (2010) suggest that emplacement of the Mt. Powell batholith is younger than 65.4 Ma based on $^{40}Ar/^{39}Ar$ dates from the adjacent Philipsburg batholith, and Elliott et al. (2013) further suggest that emplacement is pre-53 Ma based on AMCC-related detachment faults that cut the batholith.

Several Late Cretaceous-Eocene intrusive suites are exposed in the Anaconda Range. Near the LISZ, Grice (2006) dated the non-foliated, granodioritic Storm Lake stock to 74.6 Ma. East of the LISZ, Foster et al. (2007) dated the Hearst Lake plutonic suite to ~53 Ma, coincident with the onset of AMCC extension. To the southwest, Howlett et al. (2021) dated two-mica granites of the Pintler Creek batholith to 60.87 and 62.7 Ma. They also dated two dacite dikes to 51.04 and 52.75 Ma. This generation of dikes appears to be coeval with the Eocene Lowland Creek volcanic field west of Butte, MT, which was active from 52.9 to 48.6 Ma (Dudás et al., 2010) and synchronous with calc-alkaline Kamloops-Absaroka-Challis magmatism. Currently, no geochemical data exists for Eocene intrusive rocks in the Anaconda Range, making correlation with the Lowland Creek volcanic field uncertain.

METHODS

Field Methods

We conducted 1:24,000 scale geologic mapping in the Carpp Ridge 7.5' quadrangle using the StraboSpot 2 iPad app (https://strabospot.org/) to determine structural style and to document cross-cutting relationships between intrusive rocks and planar fabrics. Several representative hand samples were collected from each lithology to assist with unit descriptions, and thin sections were obtained to assist with unit identification and determination of fabric relationships. We used structural data collected in the field to construct an E-W oriented cross-section to illustrate our interpretation of structural style and kinematics.

Igneous Zircon U-Pb Geochronology

Three samples were collected from plutons and dikes for U-Pb zircon geochronology. We separated zircons from bulk samples using standard rock crushing techniques, a Wilfley table, Frantz magnetic separator, and heavy liquids at Montana State University. For each sample, 50 high quality zircons were mounted alongside SLmix (563.2 ± 4.2 Ma, Gehrels et al. (2008)), R33 (420.53 ± 0.16 Ma, Mattinson (2010)) and FC (1098.47 ± 0.33 Ma, Mattinson (2010)) zircon standards. Mounted zircons were polished to a depth of ~20 µm and sent to the Arizona LaserChron Center at the University of Arizona for imaging and analysis. Cathodoluminescence (CL) and backscattered electron (BSE) images were taken of each mount using a Hitachi 3400N SEM and a Gatan CL2 detector system. BSE images were used to target individual zircons for isotopic analysis and specific age domains in each zircon were identified using CL images. A Photon Machines Analyte G2 Excimer equipped with HelEx ablation cell was used to laser ablate each zircon to a spot diameter of 20 microns and a depth of 10 microns for ~10 seconds following methods outlined by Gehrels et al. (2008). Ablated material was transferred in helium to the plasma source of an attached Element2 HR single-collector ICP-MS, and signal intensities for U, Th, Pb, and Hg isotopes were measured using an SEM. Sensitivity with a laser energy density of ~5 J/cm^2, a repetition rate of 8 hz, and an ablation time of ~10 seconds was ~58,000 cps/ppm. We reduced data using AgeCalcML (https://www.kurtsundell.com/agecalcml) following reduction and reporting procedures outlined by Gehrels et al. (2008) and Horstwood et al. (2016). “Best Ages” were calculated for each standard and unknown based on $^{206}Pb/^{238}U$ ages for analyses < 900 Ma and $^{206}Pb/^{207}Pb$ ages for analyses > 900 Ma. Preliminary filters rejected analyses with >20% discordance, >5% reverse discordance, or >10% internal (measurement) uncertainty. All uncertainties were reported at 2-sigma error. We created concordia plots to further examine discordance in each dataset and used CL images to identify/remove analyses that may have been affected by ablation of xenocrystic cores and/or multiple age domains. Probability density plots were constructed to identify the youngest grain populations in each sample, which were interpreted to represent the crystallization age. Weighted-mean ages for zircon standards SLmix, R33, and FC analyzed in this study are 557.8 ± 10.61 Ma (MSWD = 0.03), 424.13 ± 9.18 Ma (MSWD = 0.07), and 1099.31 ± 44.87 Ma (MSWD = 0.02) respectively.

RESULTS

Geologic Mapping

The Carpp Ridge 7.5’ quadrangle is bisected by the Georgetown thrust (Figure 3). The footwall and hanging wall of this structure preserve slightly different stratigraphic sections with similar structural styles. To the west, the footwall features complexly deformed rocks characteristic of the AMCC footwall, while the hanging wall to the east preserves lightly metamorphosed strata of the Sapphire allochthon. These rocks appear to have been folded by the same deformation that folded rocks in the Georgetown footwall.

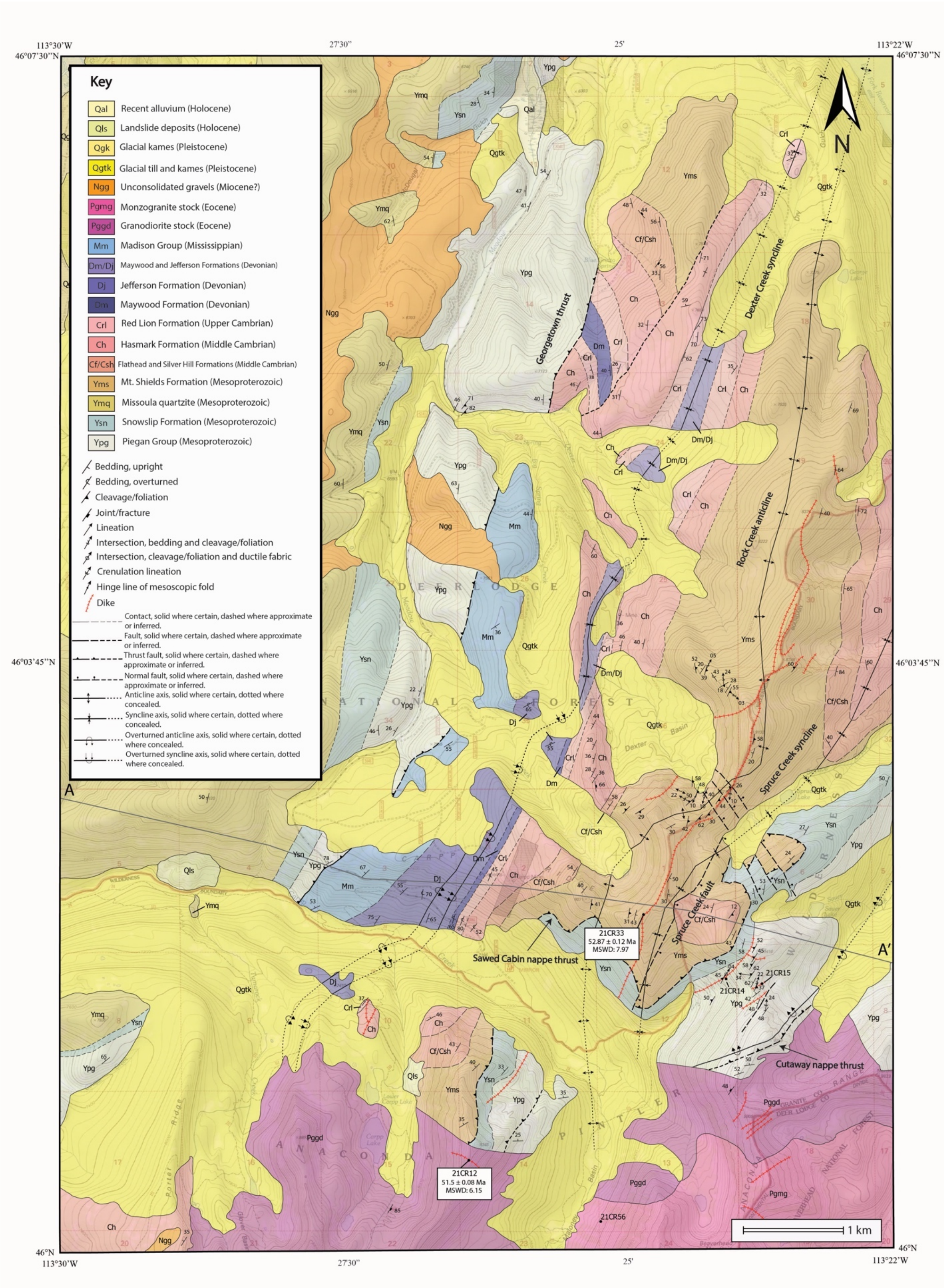
Key
Qal Recent alluvium (Holocene)
Qls Landslide deposits (Holocene)
Qgk Glacial kames (Pleistocene)
Qgtk Glacial till and kames (Pleistocene)
Ngg Unconsolidated gravels (Miocene?)
Pgmg Monzogranite stock (Eocene)
Pggd Granodiorite stock (Eocene)
Mm Madison Group (Mississippian)
Dm/Dj Maywood and Jefferson Formations (Devonian)
Dj Jefferson Formation (Devonian)
Dm Maywood Formation (Devonian)
Crl Red Lion Formation (Upper Cambrian)
Ch Hasmark Formation (Middle Cambrian)
Cf/Csh Flathead and Silver Hill Formations (Middle Cambrian)
Yms Mt. Shields Formation (Mesoproterozoic)
Ymq Missoula quartzite (Mesoproterozoic)
Ysn Snowslip Formation (Mesoproterozoic)
Ypg Piegan Group (Mesoproterozoic)
Bedding, upright
Bedding, overturned
Cleavage/foliation
Joint/fracture
Lineation
Intersection, bedding and cleavage/foliation
Intersection, cleavage/foliation and ductile fabric
Crenulation lineation
Hinge line of mesoscopic fold
Dike
Contact, solid where certain, dashed where approximate or inferred.
Fault, solid where certain, dashed where approximate or inferred.
Thrust fault, solid where certain, dashed where approximate or inferred.
Normal fault, solid where certain, dashed where approximate or inferred.
Anticline axis, solid where certain, dotted where concealed.
Syncline axis, solid where certain, dotted where concealed.
Overturned anticline axis, solid where certain, dotted where concealed.
Overturned syncline axis, solid where certain, dotted where concealed.
113°30'W
46°07'30"N
27'30"
25'
113°22'W
46°03'45"N
46°N
N
Georgetown thrust
Dexter Creek syncline
Rock Creek anticline
Spruce Creek syncline
Spruce Creek fault
Sawed Cabin nappe thrust
Cutaway nappe thrust
A
A'
21CR33
52.87 ± 0.12 Ma
MSWD: 7.97
21CR12
51.5 ± 0.08 Ma
MSWD: 6.15
21CR14
21CR15
21CR56
1 km

Figure 3 (Previous page): 1:24,000 scale geologic map of the Carpp Ridge quadrangle in the west-central Anaconda metamorphic core complex. Location and age details of U-Pb geochronology samples are shown in white boxes. A-A' line corresponds to cross section in Figure 18.

Stratigraphy of the Georgetown Thrust Footwall

The footwall of the Georgetown thrust is characterized by an upright and locally overturned section of Belt-Paleozoic metasedimentary strata intruded by numerous plutons, dikes, and sills. Ten Mesoproterozoic-Mississippian units were identified in the area based on stratigraphy of Lonn et al. (2003) and Lonn and Lewis (2009): Mesoproterozoic Piegan Group, Mesoproterozoic Mt. Shields and Snowslip formations of the Missoula Group, Cambrian Flathead, Silver Hill, Hasmark, and Red Lion formations, Devonian Maywood and Jefferson formations, and Mississippian Madison Group.

The Piegan Group (Figure 4A) is characterized by highly foliated, interbedded white quartzite and grey calcareous argillite. No attempt was made to subdivide Piegan strata into the Helena and Wallace formations, as correlation in this region has proven difficult (Jeff Lonn, *pers. comm.)*. Non-polygonal "crinkle cracks", as described by Winston et al. (2016), and molar tooth structures are present throughout the unit. In some areas, Piegan strata display considerable bedding transposition, mylonitization, and small, rootless isoclines.

Strata of the Piegan Group grade conformably into the Snowslip Formation, the basal Missoula Group. The Snowslip Formation is characterized by a lower succession of interlaminated green and black argillites. Further up-section, this succession is interbedded with thicker quartzite beds, then transitions to a succession of maroon argillites interbedded with quartz granule conglomerate. Ripples, mud cracks, and mud rip-up clasts are common throughout this unit. Snowslip argillites are slightly foliated and appear phyllitic.

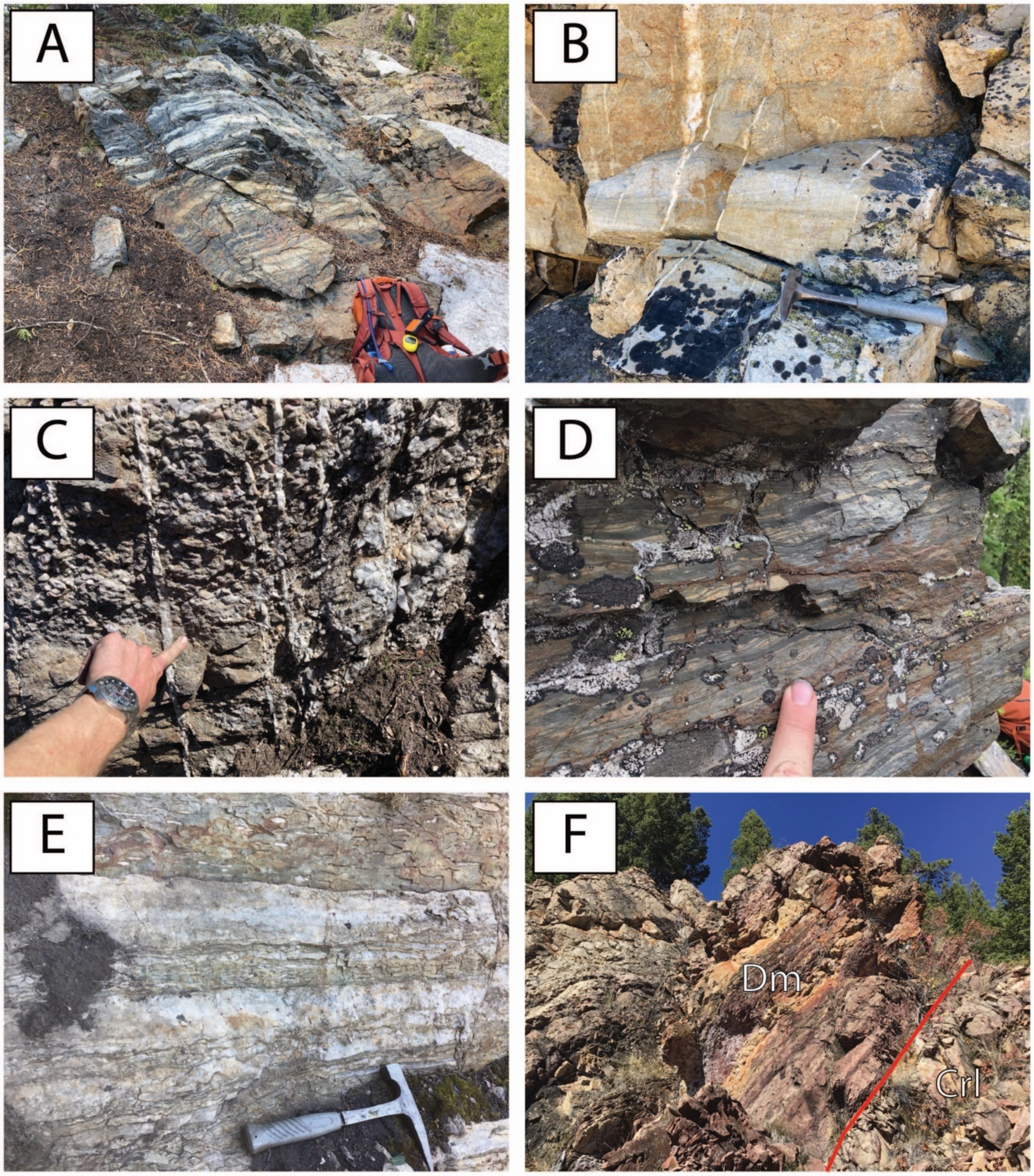
A
B
C
D
E
F
Dm
Crl

Figure 4 (Previous page): Assorted field photos from the footwall of the Georgetown thrust. A) Deformed interbedded white quartzite and grey calcareous argillite of the Piegan Group. B) Cross-laminated quartzite of the Mt. Shields Formation with abundant tension gashes. C) Quartz-pebble conglomerate of the Flathead Formation with bedding-perpendicular quartz veins. D) Lenticular-bedded slate of the Silver Hill Formation. E) Interbedded white limestone and wavy-laminated siliceous material of the Red Lion Formation. F) Well-exposed unconformable contact between the Devonian Maywood and Upper Cambrian Red Lion Formations.

The Snowslip Formation is separated from the Mt. Shields Formation by a bedding-parallel discontinuity, referred to as the Sawed Cabin detachment by Lonn and Lewis (2009) and the East Fork branch thrust by Lidke and Wallace (1992), that omits most of the Snowslip Formation and the entire overlying Shepard Formation. In the southeastern Carpp Ridge quadrangle, we did not observe any apparent fault rocks along this discontinuity at the locality described by Lonn and Lewis (2009) along the crest of the Anaconda Range, however, Lidke and Wallace (1992) described zones of sheared and cleaved rock measuring 1-10 meters thick in the Snowslip Formation below the discontinuity south of Spruce Lake. Above this fault, the Mt. Shields Formation (Figure 4B) consists of massive, grey-white cross-laminated quartzite and siltite with abundant red mud chips. Slightly to the north, in the Dexter Basin, this unit consists of interbedded grey quartzite and phyllite with occasional ripple marks. These successions may correspond to the informal Mt. Shields member 1 and member 2 respectively. In thin section, these rocks appear sub-arkosic and are predominantly composed of poorly sorted, sub-rounded quartz grains with minor microcline, quartz lithics, and mafic phases supported by a sericite matrix. Foliation is weakly developed and defined by aligned elongate quartz, sericite, and syn-metamorphic muscovite grains. Total thickness of the entire Missoula Group section along the crest of the Anaconda Range is ~230 meters.

A regionally developed pre-middle Cambrian angular unconformity separates the Mt. Shields Formation from the overlying Middle Cambrian Flathead Formation (Figure 4C). The Flathead Formation consists of a basal quartz pebble conglomerate and massive quartzite. Graded beds are well developed along the eastern limb of the Spruce Creek syncline (Figure 3). The quartz pebble conglomerate is well exposed on the western flank of the Maloney Basin and along the crest of the Anaconda Range in the southern part of the quadrangle. In the northern part of the quadrangle (Figure 3), in the hills east of Blue Grotto Spring, the Flathead Formation is characterized by bold, blocky outcrops of massive pink-weathering quartzite with prominent SE dipping joints. In thin section, Flathead rocks are pure quartz arenites containing very coarse sand-sized, angular to subrounded grains with sutured grain boundaries and undulatory extinction.

The Middle Cambrian Silver Hill Formation (Figure 4D) conformably overlies the Flathead Formation. This unit is stratigraphically equivalent to the Wolsey Formation east of the Anaconda Range. Basal Silver Hill strata consist of interbedded orange-weathering white quartzite and purple argillites. Up-section, this succession grades into thinly laminated, rusty-weathering micaceous black slate and quartzite. Quartzite laminations appear lenticular and sometimes resemble bedding-parallel fabrics, making it difficult to determine whether this structure is depositional or tectonic in origin. The top of the Silver Hill Formation is characterized by a light-grey, wavy-laminated limestone that is almost indistinguishable from the Upper Cambrian Red Lion Formation, which is also present in the field area.

Conformably overlying the Silver Hill Formation is the Middle Cambrian Hasmark Formation, which is stratigraphically equivalent to the Meagher Formation east of the Anaconda

Range. The base of the Hasmark Formation is characterized by a tan to light-grey colored ooidal dolostone. In thin section, ooids are made of xenotopic dolomite and surrounded by a recrystallized calcite matrix. The middle consists of a thin grey zone of massive dolostone containing white, “twig-like” protrusions. The upper Hasmark is characterized by a bright, cream-weathering ooidal dolostone similar to the base. Zones of malachite and azurite mineralization are present throughout the unit.

Above the Hasmark Formation is the conformably overlying Upper Cambrian Red Lion Formation (Figure 4E, F). It is stratigraphically equivalent to the Snowy Range Formation east of the Anaconda Range. The base is characterized by calcareous maroon argillites and closely spaced yellow limestone beds containing small, maroon pebbles and wavy interlaminated siliceous and dolomitic material. Up-section, spacing between limestone beds and laminations increases, and at the top, this succession grades into a small, ~3-meter-thick clastic horizon that is well-exposed along the north side of Carpp Creek. This horizon is characterized by interbedded yellow, maroon, and purple calcareous pebble-conglomerate and sandstone.

A major unconformity representing transgression of the Kaskaskia cratonic sequence (Sloss, 1963) separates the Cambrian and Devonian sections in the quadrangle. The Middle Devonian Maywood Formation unconformably overlies the Red Lion Formation and is characterized by a basal succession of thinly laminated red calcareous shale interbedded with yellow calcareous sandstone (Figure 4F). This succession grades up into interbedded calcareous sandstones. Conformably overlying the Maywood Formation is the Upper Devonian Jefferson Formation. This unit is poorly exposed in the quadrangle, but generally consists of dark gray, massive dolostone interbedded with limestone in some areas. The Mississippian Madison Group conformably overlies the Devonian section, and is characterized by grey, well-bedded fossiliferous limestone containing crinoids, bryozoans, and brachiopods.

The Georgetown footwall section is intruded by several Eocene-aged stocks, dikes, and sills. The extreme southern part of the quadrangle consists of two plutons: a locally foliated biotite-hornblende granodiorite and a non-foliated biotite monzogranite. Intrusive relationships between these two bodies are unclear, but in most places, the monzogranite appears to intrude the granodiorite. It is also possible that two units are part of a composite zoned intrusion (Figure 2). Dikes and sills have a similar composition to the plutons and may be comagmatic with them.

Stratigraphy of the Georgetown Thrust Hanging Wall

The hanging wall of the Georgetown thrust is characterized by a west-dipping panel of upright Piegan and Missoula Group strata. Its stratigraphy is very similar to the footwall with some notable exceptions. Piegan Group strata consist of thin, rhythmic laminations of yellow dolomitic and grey calcareous argillites (Figure 5A). In some areas, strata appear foliated and display considerable bedding transposition, small rootless isoclines, and protomylonitic fabrics. The Snowslip Formation is similar to its equivalent in the footwall and is characterized by thinly inter-laminated maroon argillites and pinkish-white sub-arkosic siltite (Figure 5B). Up-section, thicker beds of sub-arkose become more dominant over thinly laminated argillite. In contrast to the footwall, the Snowslip Formation is not phyllitic, indicating sub-greenschist facies metamorphic conditions.

Conformably overlying the Snowslip Formation is the Missoula quartzite (Figure 5C), an informal unit designated for this study. Lonn et al. (2003) mapped these rocks as the Mt. Shields and

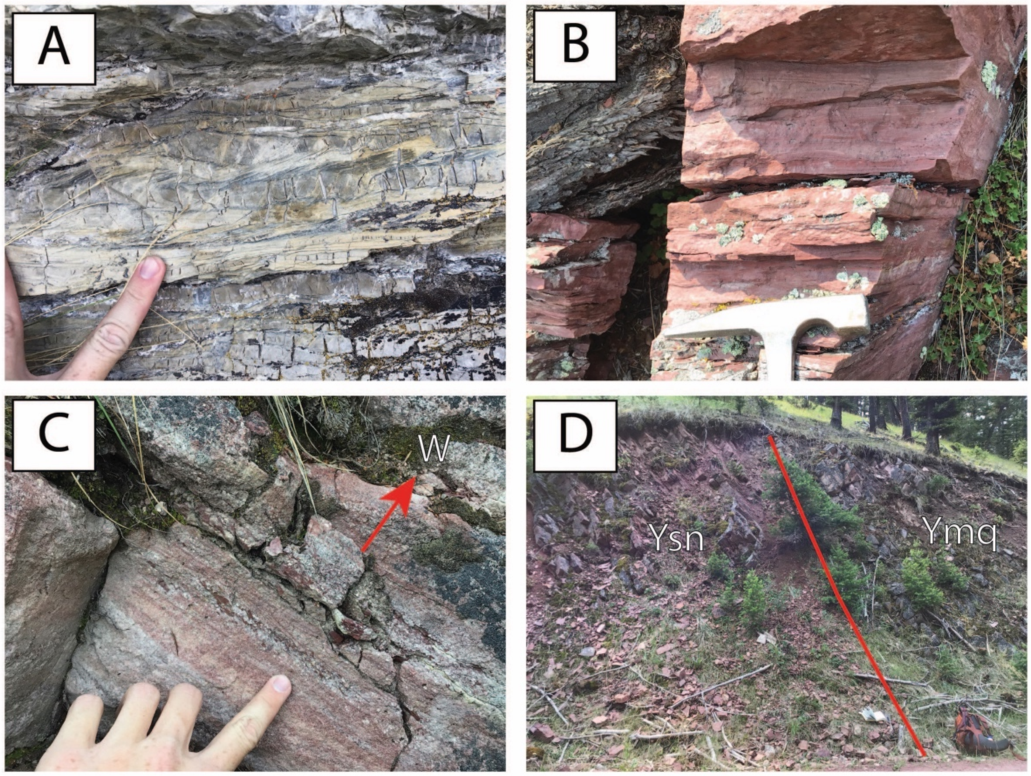

Figure 5: Assorted field photos from the hanging wall of the Georgetown thrust. A) Transposed interbedded grey calcareous argillites and yellow dolomites of the Piegan Group. A small rootless isocline is visible with an attenuated overturned limb. B) Maroon argillite of the Snowslip Formation. C) Inverse grading in the Missoula quartzite. Subtle cross-laminations suggest tops-to-west, indicated by red arrow. D) Well-exposed conformable contact between the Snowslip Formation and the Missoula quartzite.

Bonner formations, however, recent recognition of the Lemhi subbasin of the Belt Supergroup by Burmester et al. (2016) has brought these designations into question. These rocks are much coarser grained than equivalent Mt. Shields and Bonner formations and may represent a transitional phase between more proximal Lemhi strata to the west and distal Belt strata to the east (Jeff Lonn, *pers. comm.)*. This package was transported ENE along the Georgetown thrust, bringing it in close juxtaposition with distal Belt strata. The basal Missoula quartzite (Figure 5C,

D) is characterized by poorly sorted pebble conglomerate consisting of sub-rounded to rounded grains of quartz, feldspar, lithic fragments, and red-mud chips likely reworked from the underlying Snowslip Formation. The conglomerate grades into interbedded couplets of maroon cross-laminated sandstone and coarser-grained white grits containing small pebbles and mud-chips similar to the underlying pebble conglomerate. These couplets show inverse grading, and cross-laminations indicate tops-to-west. The rest of the unit is characterized by cross-bedded sub-arkoses that transition into texturally mature quartz arenites further up-section.

Structure

Thrust faults, F_1 overturned and recumbent folds, ductile shear zones, F_2 upright folds, and high-angle faults deform the Belt-Paleozoic section in the Carpp Ridge quadrangle. Thrust faults are folded by both overturned and upright folds, and high-angle faults cut thrust faults and folds. Bedding-parallel attenuation fabrics in the Piegan and Missoula groups are axial planar to the FRA, and these fabrics are also present in a locally foliated granodiorite stock mapped in the southern part of the field area, where it intrudes the hinge of the FRA.

The Georgetown thrust places Piegan Group strata on top of the Madison Group in the southern and central parts of the quadrangle, and Piegan Group on the Mt. Shields through Paleozoic section in the north (Figure 3). In the southern part of the field area, Piegan strata within meters of the Georgetown thrust appear highly flattened and sheared, although what component of this flattening is related to thrusting versus subsequent deformation is unclear. Strata at this locality also dip 78º to the northwest, exceeding typical thrust fault dips. Further to the north, the thrust cuts across an overturned NE-verging syncline cored by the Maywood

Formation (Figure 3). The syncline and the thrust are cut by a NE-striking high-angle fault, although cross-cutting relationships with the thrust itself are obscured by Quaternary glacial till. Mapping by Lonn and McDonald (2004) southeast of Carpp Ridge documented NE-striking high-angle faults that cut the Georgetown thrust, and mapping in the east-adjacent Storm Lake quadrangle by Lidke and Wallace (1992) and Lonn et al. (2003) show that the Georgetown thrust is folded into the western limb of the F_2 Rock Creek anticline (RCA) and adjacent Rock Creek syncline (Figure 2) . The steepness of the Georgetown thrust may be the result of both folding and subsequent faulting, however, in the southern part of the quadrangle where the fault is well-exposed, no normal faults were documented near the thrust. Assuming that there are no underlying thrust ramps causing this rotation, subsequent folding is likely responsible for the steep dip.

Two generations of folds were observed in the Carpp Ridge quadrangle: F_1 asymmetric folds with bedding-parallel S_1 axial planar cleavage and transposition fabrics, as well as F_2 upright folds that deform earlier fabrics. S_1 is well-developed in the Piegan Group along the crest of the Anaconda Range, and alternating zones of high and low strain are apparent from south to north (Figure 6). At Locality 1 (Figure 6), NNE-dipping Piegan strata appear highly attenuated and mylonitized. Quartzite beds have been stretched and thinned, while considerable grain-size reduction has occurred in argillites. Bedding has been completely transposed by S_1 at this locality. At Locality 2 (Figure 6), NNE-dipping bedding is still transposed, however, the deformation appears transitional between mylonitization and cataclasis (Figure 7). At the top of

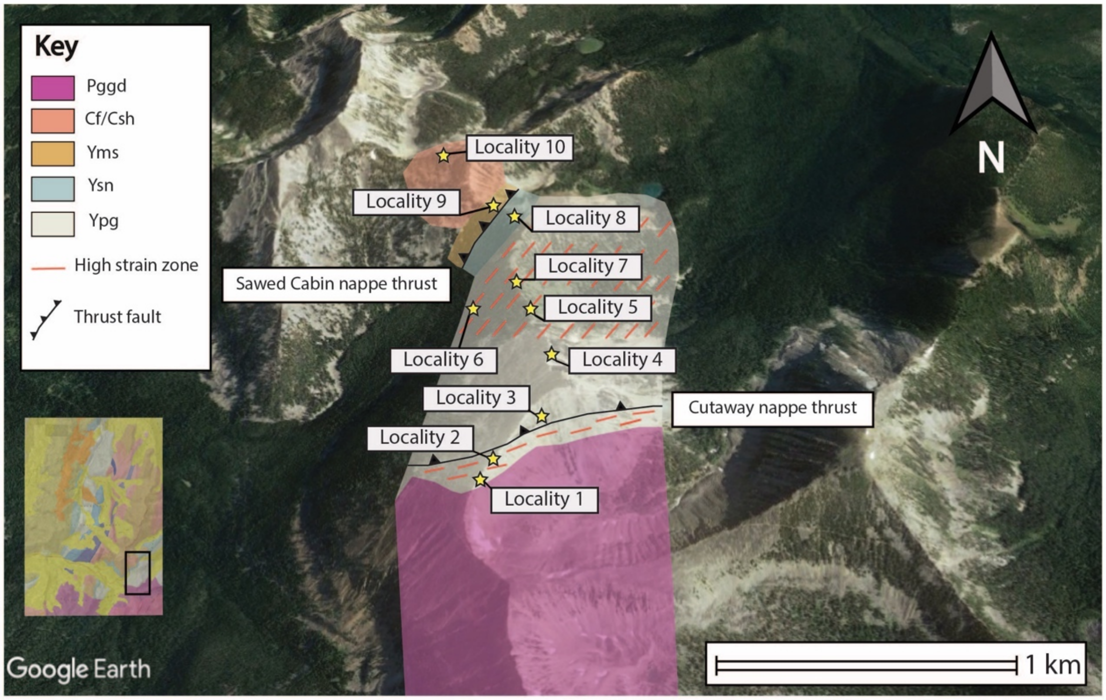

Figure 6: Strip map of the Anaconda Range in the southeastern Carpp Ridge quadrangle showing localities discussed in text. Orientation of high strain zone markers in the Piegan Group coincides with the orientation of S_1. Imagery sourced from Google Earth.

the outcrop in Figure 7, white quartzite beds have been disaggregated into chaotic blocks surrounded by incompetent argillite. Below this zone, beds have been folded into a series of NNW-verging isoclines with S_1 axial planar cleavage and highly attenuated lower limbs. The lower limb of this fold has itself been folded into a rootless isocline with axial planar cleavage parallel to bedding, and below the isocline, bedding appears completely transposed into a protomylonitic fabric. The degree of transposition decreases below this zone, with thick quartzite beds at the base of the outcrop remaining largely intact. To the north at Locality 3 (Figure 6), the attitude of bedding in the Piegan Group changes from E-striking, NNE-dipping to SW-striking,

Figure 7: F_1 rootless isoclines and associated axial planar S_1 cleavage and transposition fabrics. These folds root into a zone of cataclasite and proto-mylonite where bedding has been almost completely transposed. Photo facing WNW.

NW dipping (Figure 3, 6). A NW-dipping angular discontinuity defines this transition along the south cliff face of the unnamed peak (Figure 8), and Lidke and Wallace (1992) report that the structure is highly strained and crenulated. Above this discontinuity, the degree of transposition decreases considerably, with bedding appearing undulose but largely intact (Locality 4, Figure 6). When observed from the south, the cliff face resembles a macroscopic F_1 NW-verging recumbent fold similar to the FRA, and the angular discontinuity is likely an incipient NW-directed ductile nappe thrust with a highly attenuated NNE-dipping lower limb, although it is unclear whether bedding is overturned on this limb. We refer to the discontinuity as the Cutaway nappe thrust (CNT), a reinterpretation of the Cutaway branch thrust of Lidke and Wallace (1992), and the larger fold as the Cutaway recumbent anticline (CRA). It is intruded by a non-foliated granodiorite stock to the west but is likely present on the western side of the Maloney

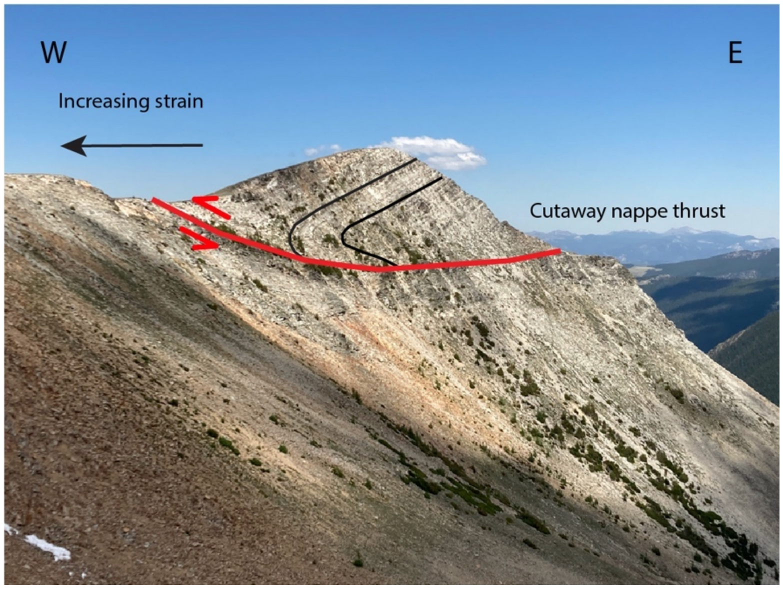

Figure 8: Cliffside exposure of the F_1 CRA and associated CNT. Transposition is stronger on the lower limb than the upright limb. Photo facing NE.

Basin as evidenced by bedding discordance in the Piegan Group (Figure 3). We infer that it has been folded by the F_2 RCA due to its change in orientation. Lidke and Wallace (1992) made a similar inference to the east, where the CNT appears folded by the F_2 Sauer Creek anticline.

Further north at Locality 5 (Figure 6), lightly transposed bedding in the Piegan Group transitions into a zone of bedding-parallel shortening and boudinage. Deformation here appears ductile, although an S_2 cleavage oriented 025/37º cuts across NW-dipping S_1 fabrics. At Locality 6 (Figure 6) in the Carpp Creek cirque, zones of intense mylonitization and boudinage have transposed bedding into S_1, which is typically oriented 212/50º. The angle between bedding and S_1 in this area is around 10º-20º. A single sigma porphyroclast associated with S_1 shows apparent sinistral, top-to-NW kinematics, however, lineations are poorly developed in these outcrops, making it difficult to determine transport direction. At Locality 7 (Figure 6), the angle between bedding and S_1 is between 5º-20º and calculated lineations defined by the intersection of bedding and S_1 plunge ~60º to the WNW.

Continuing north along the crest of the Anaconda Range at Locality 8 (Figure 6), S_1 fabrics at a low angle to bedding continue through the Piegan Group and into the Snowslip Formation, where an S_1 foliation oriented 208/28º at a 28º angle to bedding was documented. Like the Piegan Group, strain partitioning is evident, however, it is not as pronounced. The Snowslip section here appears typical, but ~120 meters upsection at Locality 9 (Figure 6), phyllitic red and purple argillites transition into fine-grained, well sorted quartzite more typical of the Mt. Shields Formation. Only 90 meters further up-section, these quartzites transition to quartzite and quartz-pebble conglomerate of the Flathead Formation. West of Philipbsurg, MT, a type-section in the John Long Mountains describes a quartzite rich interval at the top of the Snowslip Formation, however, it occurs ~760 meters above the base (Lonn and Lewis, 2009). Further, in the headwall of the Spruce Creek cirque, Lidke and Wallace (1992) observed 1-10 meter thick shear zones in argillites of the Snowslip Formation just below the overlying Mt. Shields Formation. They also observed small quartz veins and pods in the Mt. Shields that terminate just above the Snowslip. Given evidence of S_1 fabrics, bedding-parallel shear zones, and tectonic attenuation of the Snowslip and Mt. Shields formations, as well as the entirely missing Shepard Formation, we refer to this feature as the Sawed Cabin nappe thrust (SCNT), another incipient NW-directed ductile thrust associated with F_1 folding. This interpretation is a revision of the Sawed Cabin detachment of Lonn and McDonald (2004). Like the CNT, this feature is present on the western side of the Maloney Basin, where it has been folded by the F_2 RCA. North of the SCNT, in the core of a faulted F_2 syncline at Locality 10 (Figure 6), an axial planar S_2 cleavage oriented 036/12 was documented in the Silver Hill Formation at 30º to bedding.

In the Maloney Basin, just south of the quadrangle's southern boundary, the hinge zone of the FRA is spectacularly exposed in the face of an unnamed peak (Figure 9A). Here, the fold is cored by argillites and quartzites of the Piegan group and displays considerable thickening in the fold hinge and ductile deformation throughout. Bedding in this area is highly transposed and often difficult to differentiate from cleavage and other fabrics, however, a series of parasitic S-folds on the upper limb of the FRA display well-developed S_1 fabrics. Attitudes of S_1 axial planar foliation are around 200/20º (Figure 9B), and angles between bedding and foliation are variable, ranging between 10º-40º. Hinge lines on smaller parasitic folds plunge ~18º towards 237 and are sub-parallel to the calculated fold axis, which plunges 10º towards 231 (Figure 9B). Interlimb angles are ~65º. In thin section, folded Piegan strata from this area display an S_1 transposition fabric defined by strain partitioned zones of grain-size reduced calcite and asymmetric quartz grains. Asymmetric tremolite sigma porphyroclasts suggest sinistral, SW-directed transport, although lineations were not apparent in outcrop.

A series of outcrops in the FRA hinge display informative relationships between S_1 and S_2 fabrics. At one locality, S_1 transposition fabrics and an F_1 rootless isocline in the Piegan Group are refolded by mesoscopic upright F_2 folds (Figure 10). At another locality, bedding-cleavage relationships between S_1 and S_2 are well-exposed. Here, bedding is oriented 227/74º, S_1 is oriented 221/25º, and S_2 is oriented 027/61º (Jeff Lonn, *pers. comm.*). Sub-vertical bedding at this locality is almost entirely transposed by $S_{1.}$ Bedding and S_1 define an intersection lineation plunging 03º towards 228, and bedding and S_2 define an intersection lineation plunging 22º

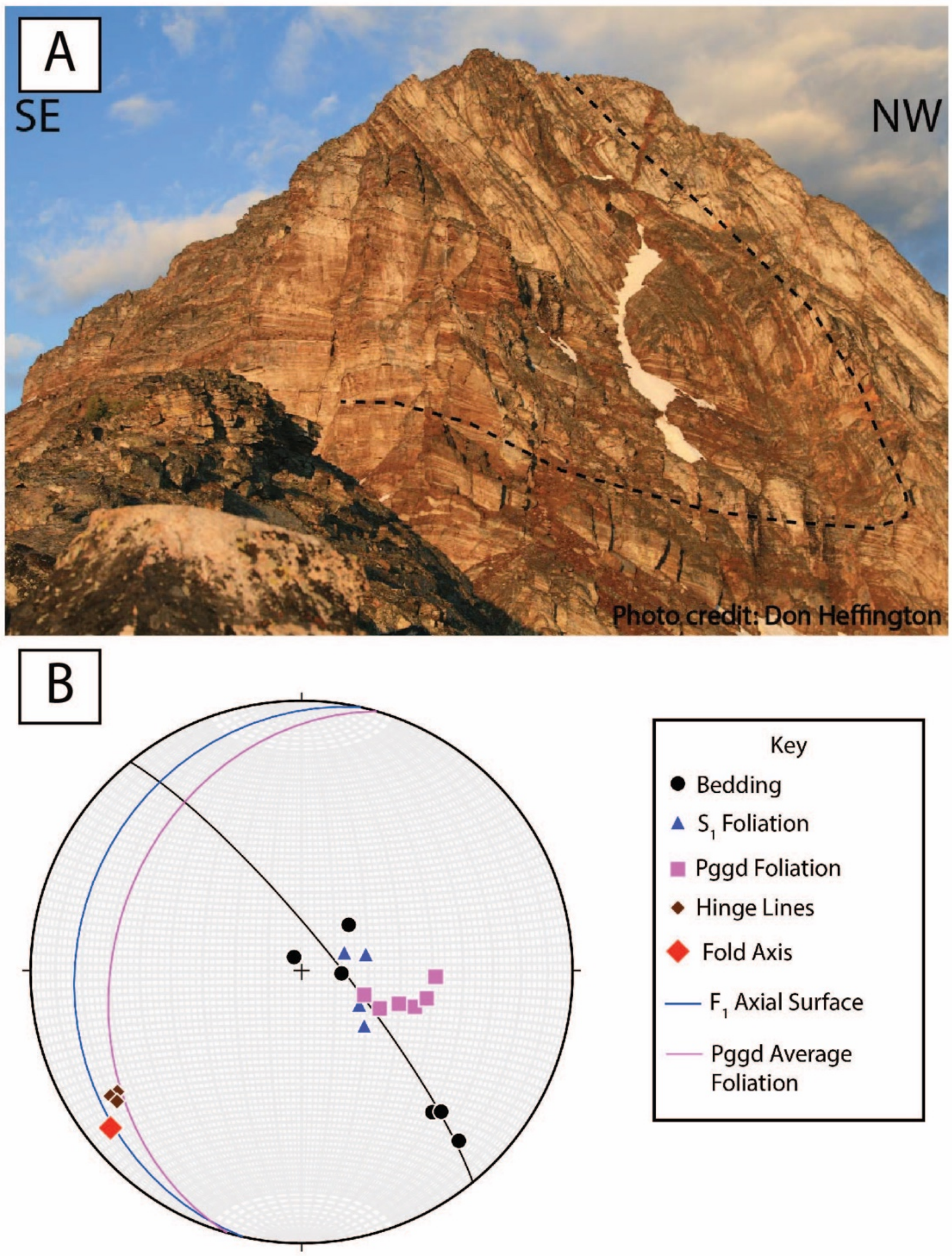

Figure 9: A) Hinge zone of the F_1 FRA exposed on an unnamed peak in the south-adjacent Warren Peak 7.5' quadrangle. The axial surface has been gently refolded by F_2 folds. Photo facing SSW. Photo credit: Don Heffington. B) Pi-diagram showing data from parasitic S-folds in the FRA hinge. Fold axis plunges 10º towards 231. Hinge lines of smaller parasitic folds are subparallel to the calculated fold axis. Axial surface is oriented 193/17º and Pggd average foliation is oriented 196/31º.

Figure 10: S_1 transposition fabrics and an F_1 rootless isocline re-folded by F_2 folds in the Piegan Group.

towards 040. This is consistent with orientation of macroscopic F_1 and F_2 fold axes reported by Flood (1974) and Lonn et al. (2003).

A biotite-hornblende granodiorite intrudes Piegan strata in the hinge zone of the FRA. While Lidke and Wallace (1992) and Wallace et al. (1992) reported this intrusion as non-foliated, high resolution mapping has revealed a moderately-developed proto-mylonitic foliation sub-parallel to S_1 axial planar fabrics in the Piegan Group. The foliation appears subtle in outcrop, but where it is well exposed, it is defined by joint surfaces oriented ~203/25º (Figure 11). Aligned biotite and small quartz a porphyroclasts are discernible in outcrop, however, no shear sense indicators were apparent. The foliation is crosscut by a later set of steeply dipping joints. In thin section, these fabrics are clearly solid-state and related to dynamic recrystallization processes. Between sections from different localities, the degree of foliation development and recrystallization is variable. In one section, subgrains with a subtle grain-shape

Figure 11: NW-dipping foliation surfaces sub-parallel to S_1 in biotite-hornblende granodiorite of the Warren Peak 7.5' quadrangle. Photo facing N.

preferred orientation have fully replaced original quartz porphyroclasts. In another, quartz grains are still intact and surrounded by small subgrains rims. Feldspars in both sections are relatively undeformed and show some evidence of brittle fracturing. While quartz microstructures in these samples are difficult to characterize, they may represent both subgrain rotation and bulging recrystallization as defined by Hirth and Tullis (1992) and Stipp et al. (2002).

S_2 cleavage is well-developed in interbedded quartzites and phyllites of the Mt. Shields Formation in the east-central portion of the quadrangle. Several outcrops along the rim of the Dexter Basin suggest an asymmetric fold geometry not apparent in outcrop. At one locality, phyllitic cleavage is oriented 014/39º and intersects NW dipping bedding at a high angle (Figure 12C), suggesting that bedding is upright. The angle between bedding and cleavage is ~57º, and intersection lineations plunge 7º towards 023. Just to the southeast, phyllitic cleavage is oriented 059/18º and intersects NE dipping bedding at a low angle, suggesting that bedding is overturned (Figure 12D). The angle between bedding and cleavage is ~45º, and intersection lineations plunge 14º towards 003. Further southeast, cleavage is nearly perpendicular to bedding at an angle of ~83º, suggesting that this outcrop may represent the hinge zone of a large-scale fold. Intersection lineations are horizontal and trend towards 205. This locality roughly coincides with the approximate hinge of the RCA , a gently NE-plunging F_2 macroscopic fold (Figure 12A, B). East of the hinge, bedding dips to the ENE and cleavage dips to the NW. Cleavage also appears slatey rather than phyllitic. At one locality along the eastern limb of the RCA, the angle between cleavage oriented 218/60º and bedding is ~87º, with cleavage steeper than bedding. Intersection lineations plunge 20º toward 026. Further southeast, the angle between bedding and cleavage decreases to ~66º, with cleavage steeper than bedding. Intersection lineations plunge 9º towards 017. Evidence from this traverse suggests that cleavage is axial planar to the F_2 RCA, intersection lineations are subparallel to its fold axis, and that asymmetric folds are developed along its limbs.

In the Dexter Basin cirque, on the western limb of the RCA, a pair of apparently W-verging asymmetric Z-folds are well-exposed (Figure 13A). Ripple marks on the overturned limb of one fold suggest both are anticlines. In contrast to similar folds in the Piegan Group, folds in the Mt. Shields Formation have a chevron-like geometry, with most deformation facilitated by competence contrasts between quartzite and slate beds rather than ductile flow. Interlimb angles are ~48º. On average, axial planar cleavage is oriented 025/55º and measured hinge lines plunge 06º towards 201 (Figure 13B). This cleavage is parallel to S_2 cleavage observed on the limbs

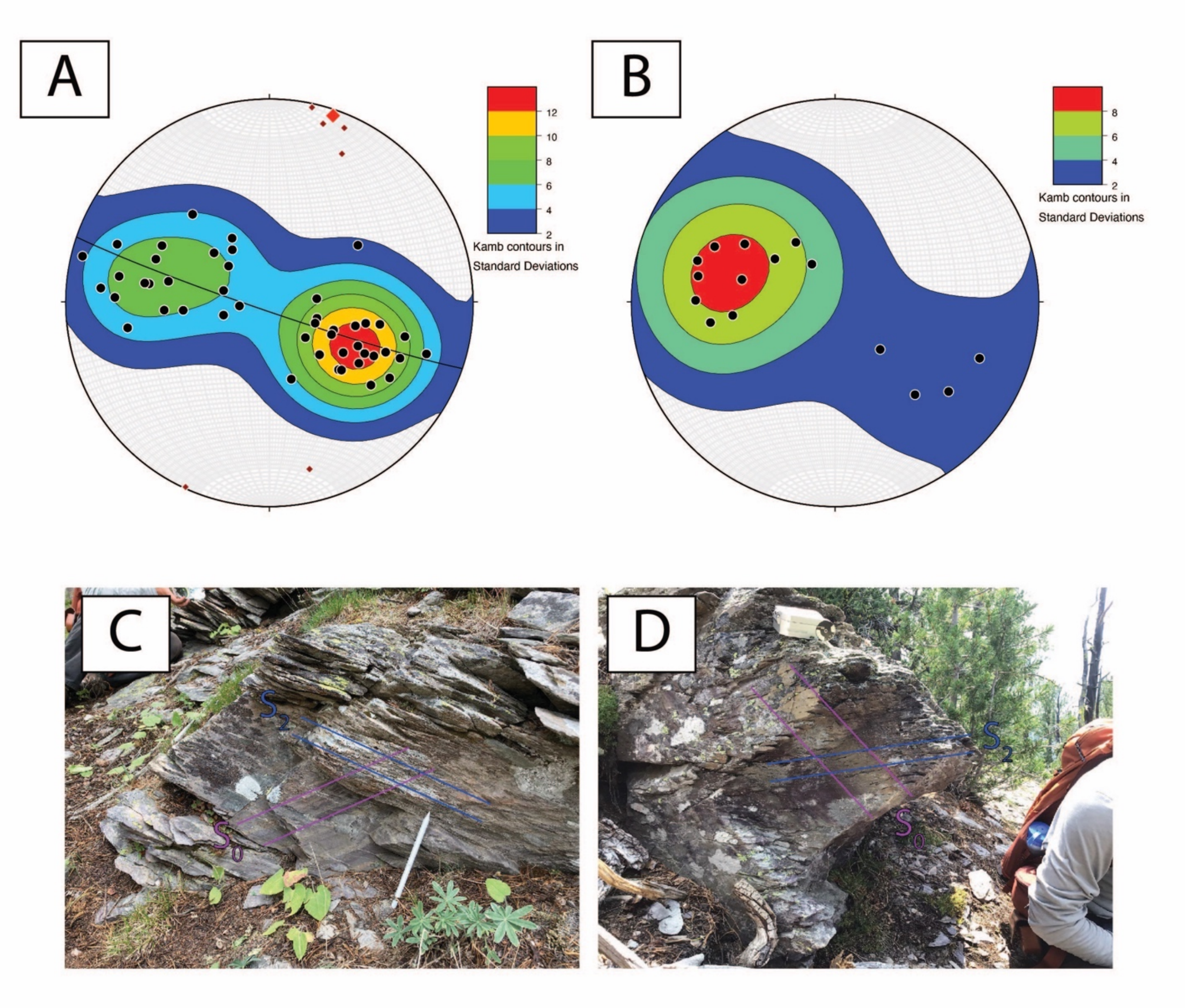

Figure 12: A) Pi-diagram showing bedding in the F_2 RCA. Large red diamond represents the calculated fold axis, which plunges 03º towards 019. Smaller maroon diamonds represent calculated intersections between bedding and S_2 and are mostly sub-parallel to the fold axis. B) Equal-area stereonet showing S_2 cleavage in the RCA. S_2 dips to the west on the eastern limb, while it dips to the east on the western limb. C) Upright limb of an asymmetric fold parasitic to the larger FRA. S_2 is steeper than bedding. Photo facing NE D) Overturned limb of the same asymmetric fold near location of C. Bedding is steeper than S_2. Photo facing SW.

of the RCA. Just south of the F_2 folds, another outcrop of the Mt. Shields Formation displays a weakly crenulated phyllitic cleavage oriented 229/50º that transposes bedding. Crenulation

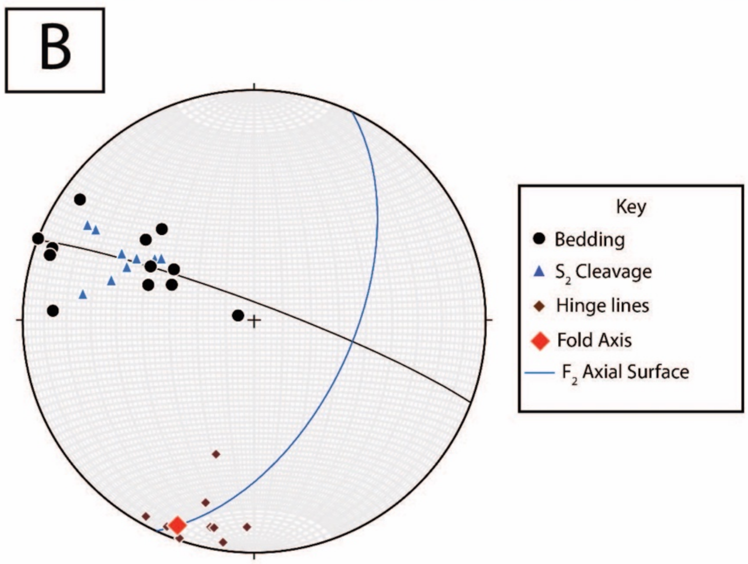

Figure 13: A) West-verging F_2 fold in the Mt. Shields Formation on the western limb of the RCA. Photo facing WNW. B) Pi-diagram showing data from two F_2 folds in the Dexter Basin. Fold axis plunges 06º towards 201. Measured hinge lines are roughly concordant to the fold axis. Axial surface is oriented 025/55º.

lineations plunge ~20º towards 302. We interpret the NW-dipping phyllitic cleavage as an S_1 fabric that has been crenulated by S_2.

At higher structural levels in the hanging wall of the Georgetown thrust, a steeply SE dipping S_2 cleavage oriented ~030/75º is well-developed in Piegan strata (Figure 14B). Angles between bedding and cleavage range between 50º-70º. Piegan strata here make up the eastern limb of the Meadow Creek syncline, a broad F_2 fold that extends west of the quadrangle with a fold axis oriented 01º/017, similar to the RCA (Figure 14A). Intersection lineations between bedding and S_2 plunge gently to both the NE and SW. The amplitude of F_2 folding decreases to the east, suggesting tighter folding at deeper structural levels.

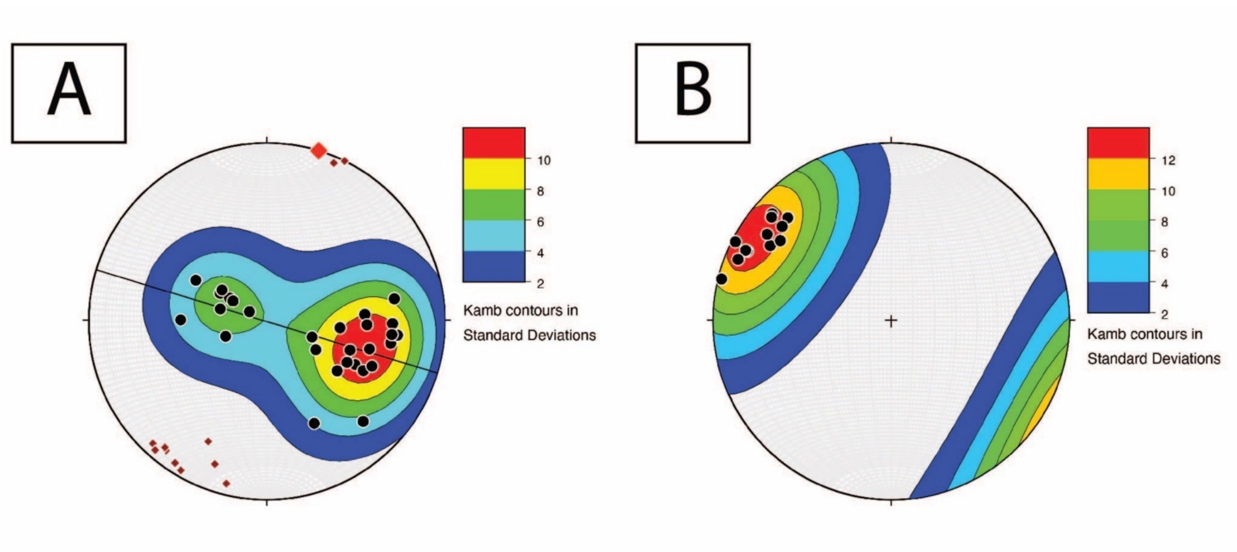

Figure 14: A) Pi-diagram showing bedding in the F_2 Meadow Creek syncline. Large red diamond represents the calculated fold axis, which plunges 01º towards 017. Smaller maroon diamonds represent calculated intersections between bedding and S_2, with the majority plunging gently SW. B) Equal-area stereonet showing steeply dipping S_2 cleavage.

S_1 and S_2 fabrics are not well-developed in the Paleozoic section, with some exceptions. In the northern part of the quadrangle, near Blue Grotto Spring, fractures oriented 317/44º and

035/48º intersect bedding in the Flathead Formation at 70-80º angles. We interpret these as S_2 cleavage planes. Boudinage likely related to S_1 was observed at one locality in the Hasmark Formation along the west flank of Warren Peak, although boudins axes were not exposed well enough to take accurate measurements.

A series of high-angle faults cut the Georgetown thrust, ductile nappe thrusts, and folds in the Carpp Ridge quadrangle. The most prominent and well-exposed of these faults is the Spruce Creek fault (Figure 3), which cuts the eastern limb of the RCA and juxtaposes strata of the Mt. Shields and Flathead formations. The fault plane is well exposed along the headwall of the Spruce Creek cirque and has an attitude of 012/42º (Figure 15). Slickenfibres on fault mirrors at this locality plunge 55º towards 120º, suggesting oblique-slip normal-sense motion. Immediately north, a series of NW trending normal faults cut the Snowslip and Mt. Shields in an anticline adjacent to the Sauer Creek syncline. Notably, the faults cut an extensive granodiorite dike in the hinge zone of the Rock Creek anticline. The relationship of these faults to the Spruce Creek fault is unclear. Due to their NW trend, it is possible that they cut the Spruce Creek fault, although cross-cutting relationships are obscured by Quaternary glacial till. To the south near Locality 6 (Figure 6), a smaller fault cuts the Piegan Group. Here, the fault plane is oriented 033/53º and is defined by a broad zone of cataclasite. Given its orientation, this feature is likely a synthetic subsidiary of the Spruce Creek fault. In the foothills near Blue Grotto spring, another NE trending fault creates complex relationships between an overturned syncline cored by the Maywood Formation and the NE-plunging Dexter Creek syncline (Figure 3). While this fault is largely implied by changes in bedding attitude, fault mirrors were documented in the Flathead Formation near its contact with the Hasmark Formation. Lonn et al. (2003) interpreted this fault as cutting the Georgetown thrust beneath Quaternary glacial till, and our mapping supports this interpretation.

Figure 15: Iron-oxide stained, polished fault surface associated with the Spruce Creek fault. Slickenfibres on this surface plunge 55º towards 120. Photo facing NE.

U-Pb Geochronology

Three igneous samples were collected for U-Pb geochronology to better constrain the age of deformation in the Carpp Ridge area, specifically the age of F_1 and F_2 folding. All three samples appear to be coeval with ~53 Ma Hearst Lake plutonic suite in the eastern Anaconda Range (Foster et al., 2007) and several ~51-52 Ma dacite dikes just south of the field area (Howlett et al., 2021). These intrusions likely formed during initial exhumation of the AMCC at ~53 Ma. For detailed data tables of each sample, see Appendix 1. For concordia plots of data interpreted to represent the crystallization age of each sample, see Appendix 2.

Sample 21CR12

Sample 21CR12 (Figure 16A) was collected from a rhyolite dike intruding Pggd in the southern part of the quadrangle (Figure 3). It is a porphyritic rhyolite composed of medium-grained quartz, microcline perthite, plagioclase, and biotite phenocrysts with minor hornblende and titanite in an aphanitic, quartz-rich groundmass. Groundmass make up ~60% of the sample. Quartz phenocrysts appear strained and exhibit undulose extinction, and surrounding groundmass is often in optical continuity with phenocrysts. Plagioclase phenocrysts display complex zonation and are often fractured. Some feldspar grains have experienced sericitic alteration, likely through hydrothermal processes. Zircons display simple igneous zoning and U-Pb dates range from 54.07 ± 0.54 to 49.35 ± 0.66 Ma (n=49). One core was dated to 149.9 ± 14.8 Ma, however, this analysis was rejected by the AgeCalc data reduction routine due to high $^{206}Pb/^{238}U$ error. Several analyses were removed manually due to high discordance and high $^{207}Pb/^{235}U$ error relative to most analyses. Mixing of age domains during ablation may be responsible for observed discordance. Two distinct age populations were identified from this sample, and the weighted-mean age for 33 grains representing the youngest population is 51.5 ± 0.08 Ma (MSWD = 6.15) (Figure 17). This age is interpreted as the crystallization age for sample 21CR12.

Sample 21CR33

Sample 21CR33 (Figure 16B) was collected from an extensive granodiorite dike that intrudes the hinge of the RCA (Figure 3). At one locality along the Dexter Basin ridgeline, the attitude of the dike is 193/44º, discordant to S_2 cleavage. The dike is also cut by a late NW-trending normal fault just north of Spruce Lake. Sample 21CR33 is a hydrothermally altered biotite granodiorite with medium-grained quartz and plagioclase phenocrysts and minor muscovite in an aphanitic, quartz-rich groundmass. Groundmass makes up ~30% of the sample.

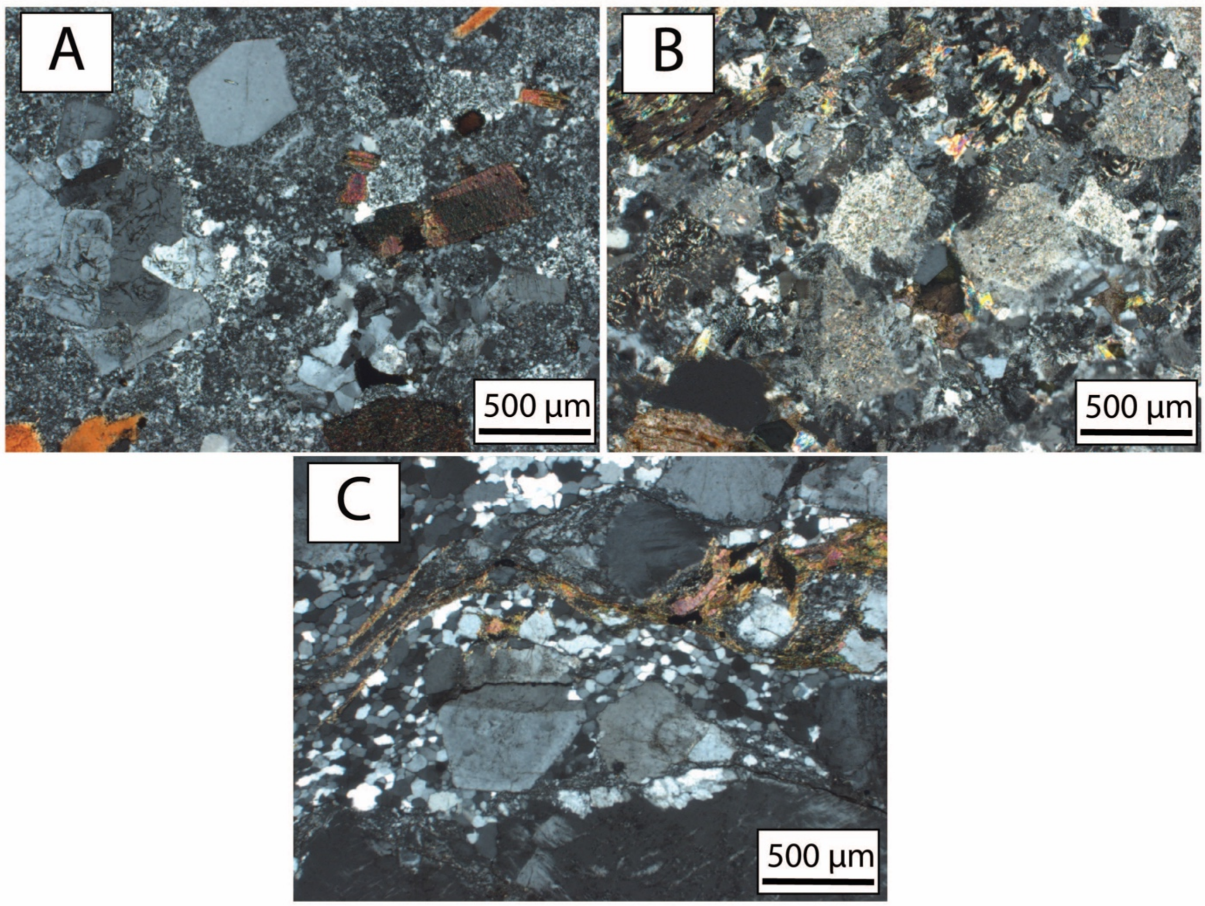

Figure 16: Thin section photomicrographs taken of each U-Pb geochronology sample. A-C correspond to 21CR12, 21CR33, and 21CR35 respectively.

Quartz phenocrysts are rounded and appear unstrained. Plagioclase phenocrysts have experienced a high degree of sericitic alteration, often obscuring original grain geometries. Myrmekite texture is present in some grains. Zircons display both simple igneous growth and oscillatory zoning, often nucleating around inherited cores. U-Pb dates range from 58.91 ± 0.6 -

51.63 ± 0.42 Ma (n=38). A population of Paleo/Mesoproterozoic xenocrystic cores was identified with ages ranging from 1737.31 ± 10.58 - 1310.13 ± 11.94 Ma (n=5). These cores were likely derived from surrounding Belt strata. One of these cores is surrounded by an 81.94 ± 0.93 Ma overgrowth, probably related to Late Cretaceous magmatism in the region. Another population of xenocrystic cores was identified with ages ranging from 63.81 ± 0.71 - 59.48 ± 0.89 Ma. These ages roughly coincide with weighted-mean ages of the Paleocene Pintler Creek Batholith, a two-mica granite dated by Howlett et al. (2021) to 60.87 Ma and 62.7 Ma. Several analyses were removed manually due to high discordance and high $^{207}Pb/^{235}U$ error relative to most analyses. Mixing of age domains during ablation may be responsible for observed discordance. Two distinct age-populations were identified from this sample, and the weighted-mean age for 23 grains representing the youngest population is 52.87 ± 0.12 Ma (MSWD = 7.97) (Figure 17). This age is interpreted as the crystallization age for Sample 21CR33.

Sample 21CR35

Sample 21CR35 (Figure 16C) was collected from a moderately foliated biotite granodiorite stock (Pggd, Figure 3) just south of the Carpp Ridge quadrangle in the FRA hinge. Where it is most well-developed, this foliation appears protomylonitic, with incipient plagioclase porphyroclasts and aligned biotite grains. The foliation is roughly concordant to S_1 in surrounding Piegan strata, although it is only locally developed in the FRA hinge. Sample 21CR35 is a medium-grained equigranular biotite granodiorite composed of quartz, plagioclase, microcline perthite, biotite, and minor hornblende. Quartz grains appear strained and display undulose extinction. In some parts of the sample, quartz grains have been recrystallized into foliation parallel zones of subgrains, while in others, they form smaller veins between larger quartz grains. Deformation lamellae appear moderately developed in some quartz phenocrysts. Plagioclase phenocrysts are common, and some display complex zonation. Biotite "ribbons"

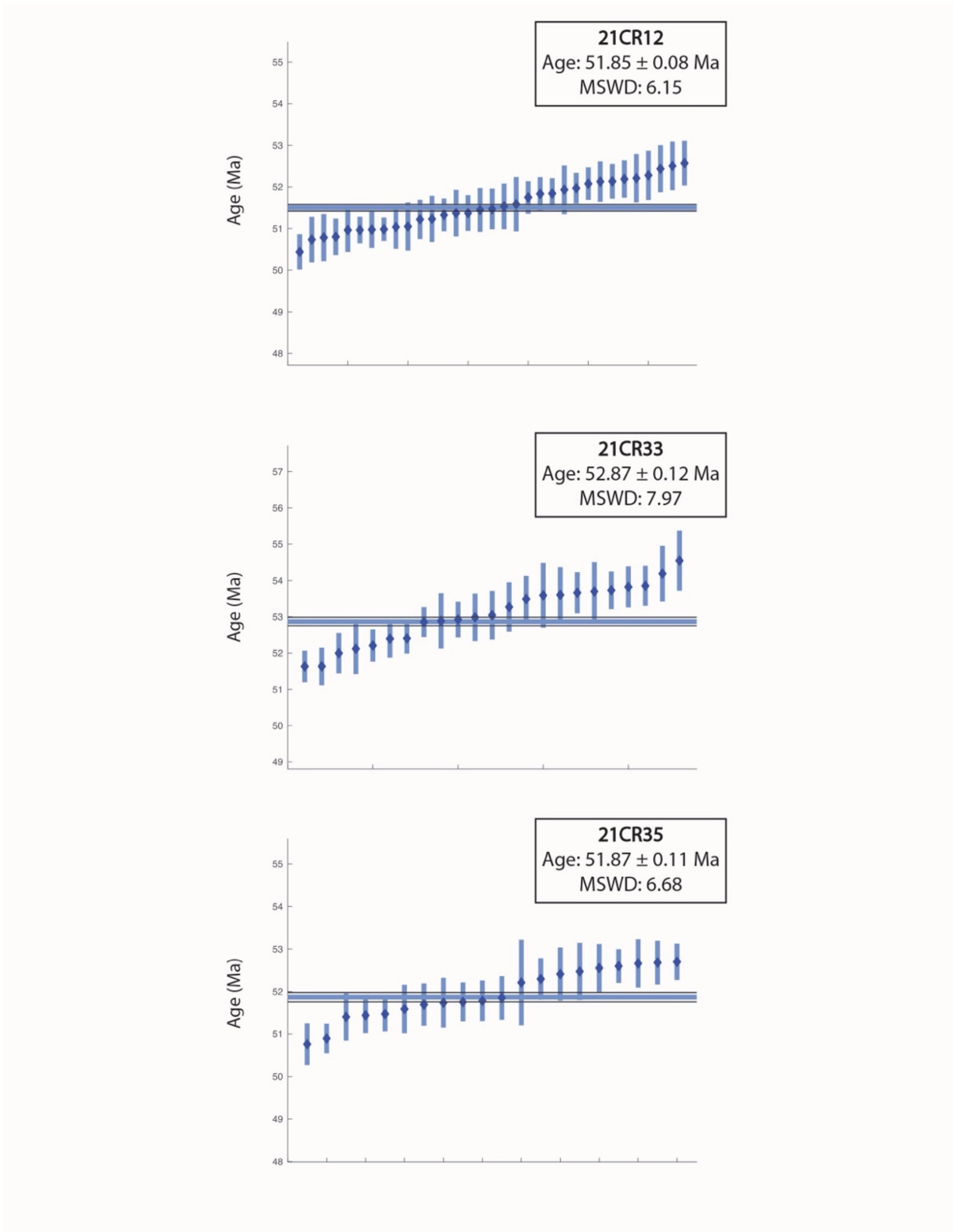

Figure 17: Igneous zircon U-Pb geochronology weighted mean plots from cross-cutting dikes and intrusions in the Carpp Ridge 7.5' quadrangle. Error is 2-sigma. High MSWD values for all samples may relate to mixing between different age domains during laser ablation.

occur within subgrain zones, often in alignment with rotated quartz grains. Zircons display both simple igneous growth and oscillatory zoning, often nucleating around inherited cores. U-Pb dates range from 57.23 ± 1.39 - 50.76 ± 0.48 Ma (n=37). Two Paleoproterozoic xenocrystic cores were identified with ages of 1857.5 ± 8.3 and 1847.8 ± 16.0 Ma respectively, however, these analyses were rejected by the AgeCalc data reduction routine due to high discordance. A Neoproterozoic core dated to 709.6 ± 5.2 Ma with a 70.0 ± 0.73 Ma rim was also identified, however, the core analysis was also rejected by AgeCalc due to high discordance. Two Late Cretaceous cores, dated to 101.55 ± 0.91 and 83.08 ± 2.75 Ma, were identified, as well as a Paleocene population of grains with ages ranging from 63.78 ± 0.87 - 60.61 ± 0.71 Ma (n=6). These ages are coincident with the age of the Paleocene Pintler Creek Batholith. Several analyses within the 57.23 ± 1.39 - 50.76 ± 0.48 Ma population were removed manually due to high discordance and high $^{207}Pb/^{235}U$ error relative to most analyses. Mixing of age domains during ablation may be responsible for observed discordance. Two distinct age-populations were identified from this sample, and the weighted-mean age for 23 grains representing the youngest population is 51.87 ± 0.11 Ma (MSWD = 6.68) (Figure 17). This age is interpreted as the crystallization age for Sample 21CR35.

DISCUSSION

Chronology of Deformation

Deformation in the Carpp Ridge quadrangle is mostly Late Cretaceous in age, with some minor Eocene deformation in the hinge zone of the FRA. Development of the Georgetown thrust is constrained by $^{40}Ar/^{39}Ar$ ages and magnetic fabric data collected by Naibert et al. (2010) from the ~75 Ma Philipsburg batholith, which intrudes the Georgetown thrust in the Flint Creek

Range. While the pluton was likely emplaced along a fault-bend fold involving the Cable Mountain anticline, magnetic fabrics strongly suggest that no internal deformation related to the Georgetown thrust occurred in the Philipsburg batholith. Taking this into account, thin-skinned Sevier thrusting along Georgetown thrust had likely ceased by 75 Ma.

The timing of F_1 and F_2 are constrained by field observations and geochronology from this study and the work of Grice (2006). At the outcrop scale, F_2 folds deforms F_1 rootless isoclines and associated S_1 transposition fabrics. At macroscopic scale, the FRA axial surface appears to be slightly deflected, perhaps by subsequent re-folding associated with the RCA (Jeff Lonn, *pers. comm.*). This is consistent with the interpretation of Wiswall (1976), who observed S_1 transposition fabrics refolded by F_2 mesoscopic folds. A 52.87 Ma non-foliated granodiorite dike (Sample 21CR33) crosscuts the RCA in the central part of the quadrangle, suggesting that F_1 and F_2 deformation had ceased before ~53 Ma. While no upper bound to this deformation was identified in the field area, Grice (2006) dated tectonic attenuation within the LISZ in the eastern AMCC footwall to ~75-74 Ma based on an ~75 Ma foliated quartz diorite dike and the cross-cutting ~74 Ma Storm Lake stock. Further, the Mill Creek nappe, a thrust-cored fold nappe exposed along the south face of Mt. Haggin, is intruded by a non-foliated quartz diorite pluton similar to the Storm Lake stock. While no explicit structural connection between the FRA, the LISZ, and the Mill Creek nappe has been made, the character of deformation is similar, therefore, we infer that F_1 and F_2 folding in the field area is likely Late Cretaceous in age, and that this deformation largely ceased by ~53 Ma. Evidence for Eocene deformation does exist in the FRA hinge based on a 51.87 Ma age from a lightly foliated biotite-granodiorite stock concordant to S_1 (Sample 21CR35, Pggd), however, this foliation is only locally developed.

Everywhere else in the field area, no foliation was observed in the stock, and along the crest of the Anaconda Range, non-foliated biotite-granodiorite was observed cross-cutting Piegan strata with well-developed mylonitic S_1 fabrics (Locality 1, Figure 6), suggesting that F_1 folding largely predated Eocene magmatism. How this solid-state fabric formed is unclear, however, it could be related to slight reactivation of the FRA during AMCC extension, which initiated around 53 Ma (Grice, 2006; Foster et al., 2010; Howlett et al., 2021). Dike ages are roughly synchronous with pluton emplacement, particularly the 51.5 Ma rhyolite dike (Sample 21CR12) that intrudes Pggd. The 52.87 Ma non-foliated granodiorite dike is cut by NW-trending normal faults that also cut across F_2 folds, strongly suggesting that these features post-date both thrusting and folding. While contact relations between the Spruce Creek and the 52.87 granodiorite dike are unclear, it cuts an F_2 syncline which suggests it likely formed after 53 Ma and prior to the NW trending faults.

Structural and Kinematic Interpretation

To illustrate structural style and kinematics, an E-W oriented cross section was constructed approximately perpendicular to the strike of major structural features (A-A’, Figure 3, Figure 18) in the quadrangle. At least four deformations affected the field area, beginning with east-directed thrusting on the Georgetown thrust during development of the Sevier fold-thrust belt. While no constraints exist on burial depth for these rocks, thermobarometric work by Grice (2006) on Late Cretaceous-aged upper amphibolite facies assemblages in the LISZ suggest that rocks in this area were exhumed from a maximum crustal depth of ~10-16 km along the Anaconda detachment fault. The Belt-Paleozoic section in Carpp Ridge only attained greenschist-lower amphibolite facies conditions based on muscovite and tremolite assemblages

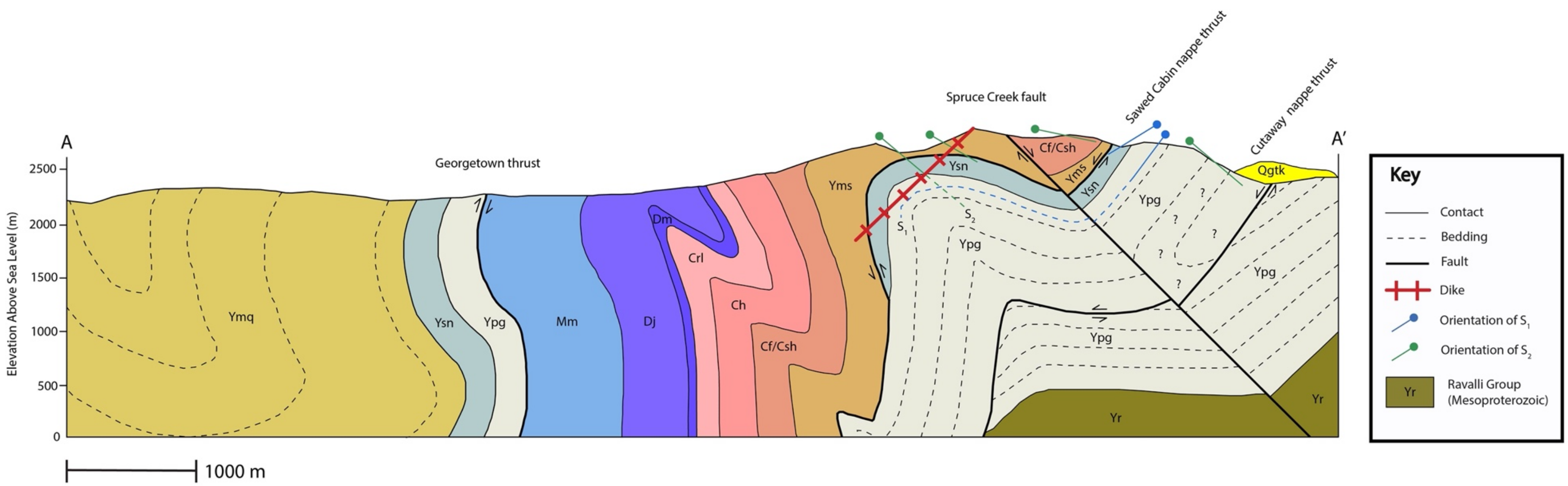

Figure 18: Cross section along A-A’ in Figure 3. F_2 upright folds control regional structure at this scale. The FRA is not depicted on this section due to its scale, but Piegan and Ravalli strata in the RCA likely core it at depth. Question-marked area in the Piegan Group above the CNT represents the geometry of the F_1 CRA. No vertical exaggeration.

in meta-argillites of the Mt. Shields Formation and Piegan Group, however, evidence for ductile deformation and recumbent folding following thin-skinned thrusting suggests that these rocks were likely near the brittle-ductile transition zone during Late Cretaceous time. The Georgetown thrust is folded by later F_2 macroscopic folds (Figure 18), as evidenced by mapping in the Storm Lake area by Lidke and Wallace (1992) and Lonn et al. (2003). It may be folded by F_1 folds at depth, although this has never been documented, perhaps due to intervening plutons.

Thrusting was followed by NW-vergent recumbent folding associated with the F_1 FRA and CRA. S_1 fabrics tectonically attenuated the Missoula and Piegan groups and are axial planar to F_1 folds in the FRA hinge. They are also sub-parallel to west-directed ductile nappe thrusts that thin and omit section (Figure 18). While our interpretation of these features as west-directed ductile thrusts associated with the propagation of F1 folds is still speculative and only somewhat constrained, we prefer this model over east-directed thrusts proposed by Lidke and Wallace (1992) and bedding-parallel detachments proposed by Lonn and McDonald (2004) for several reasons. Outcrop scale observations in the Piegan Group consistently reveal rootless isoclines with an axial planar, bedding-parallel fabric that, in some places, progresses into bedding transposition and mylonitization. The limbs of these folds are attenuated, and this attenuation is especially pronounced in lower limbs, which root into a protomylonitic zone at one locality (Figure 7). While topping indicators are absent on the north-dipping panel in the footwall of the CNT where an overturned limb might be expected, the overall geometry of the CRA is highly suggestive of an F_1 fold that formed in a similar manner to rootless isoclines. Further, the CNT is sub-parallel to S_1, suggesting coeval development, although it should be noted that no shear sense indicators have been reported from this structure, making sense of shear uncertain. It may also be possible that the CRA is a thrust-cored fold nappe similar to the Mill Creek nappe as depicted by Emmons and Calkins (1913) on their E-E' cross-section, and further corroborated by Heise (1983). At this time, we prefer the former idea, that the CNT and CRA are an integrated feature associated with F_1 folding. The relationship of the CRA to the FRA is currently unclear, however, it may be a drag fold parasitic to the FRA. Further, Lidke and Wallace (1992) reported another discontinuity structurally below that CNT that they referred to as the Cutaway thrust. They believed that this feature was an east-directed thrust fault similar to their Cutaway branch thrust that placed the Piegan Group over the Mt. Shields Formation, and it is depicted on their B-B' section as merging with the Cutaway branch thrust at depth. Subsequent investigation by Lonn et al. (2003) revealed that this feature is the strained contact between the Piegan and Ravalli groups, although there is no abrupt stratigraphic break or angular discordance like there is with the CNT or SCNT. Given this evidence, we treat the Piegan-Ravalli contact as a stratigraphic contact (Figure 18). Wallace et al. (1992) report that this contact is tightly folded into the FRA south of the Carpp Ridge quadrangle.

While the relationship between F_1 folding and the SCNT is not as clear as the CBNT, its parallelism with S_1, evidence for both ductile and brittle shear, and similar geometry to the CBNT lead us to interpret it as another F_1 nappe thrust. Lonn and McDonald (2004) interpreted this feature as a bedding-parallel detachment fault in the Kelly Lake 7.5' quadrangle, while Lidke and Wallace (1992) interpreted it as east-directed thrust fault they referred to as the East Fork branch thrust. In the Kelly Lake area, southeast of Carpp Ridge, the SCNT clearly cuts down section, placing quartzite of the Missoula Group on top of the Piegan Group. We interpret this relationship at depth in our A-A' section (Figure 18). In the Carpp Ridge quadrangle, this fault places quartzite of the Mt. Shields Formation on top of the Snowslip Formation, likely omitting the upper Snowslip and overlying Shepard Formation. While this fault clearly cuts down-section and displays younger-over older relationships, its association with S_1 fabrics suggests that this feature may be related to F_1 recumbent folding. Bedding-parallel normal faults and detachments like those proposed by Lonn and McDonald (2004) are uncommon and mechanically complicated, and the interpretation of Lidke and Wallace (1992) results in overly-complex structural relationships. We posit that, given the nature and scale of F_1 folding in the quadrangle, interpreting bedding-parallel faults and shear zones in terms of folding results in a sounder, albeit incomplete, understanding of deformation in this area. While interpreting the SCNT as a younger-over-older thrust may be problematic, the propensity of ductile deformation in incompetent strata of the Piegan Group and overlying Snowslip Formation combined with the complex nature of F_1 recumbent folding may result in complicated thrust relationships.

An alternative folding-related explanation for the CNT and SCNT is that they represent zones of focused ductile flow with the limbs of the FRA. Ductile deformation in the field area is mostly localized in incompetent argillites of the Piegan-Snowslip succession that have been "sandwiched" between more competent quartzites of the Missoula and Ravalli Groups. The strained Piegan-Ravalli contact and the SCNT may therefore bound a zone of ductile flow within the upper limb of the FRA, and these boundary conditions may have enhanced ductile flow enough to omit most of the Snowslip Formation and the entire Shepard Formation. Wiswall (1976), using the fold classification regime of Donath and Parker (1964), observed passive flow and passive slip style folding in Piegan strata, and quasi-flexural style folding in the FRA as a whole. Clearly, bulk rheology of the Belt Supergroup played a considerable role in the geometry of F_1 folding, and it is possible that the CNT and SCNT could be passive surfaces that focused ductile flow of incompetent units in the FRA. This explanation may be more fitting for the SCNT than the CBNT, since no clear evidence of F_1 folding was documented around the SCNT.

Fold-related attenuation along the limbs of large, similar-style recumbent folds is not uncommon in the footwalls of Cordilleran metamorphic core complexes. In the Ruby-East Humboldt MCC of eastern Nevada, the south-verging Winchell Lake nappe ductiley thinned Neoproterozoic-Mississippian sedimentary strata from an original thickness of ~8 km to only a few hundred meters (McGrew et al., 2000; Colgan et al., 2010; Henry et al., 2011; Long and Kohn, 2020). Further, Wrobel et al. (2021) documented considerable limb thinning and hinge thickening of Eocambrian strata in the O'Neill Peak Recumbent Syncline, another large recumbent fold in the footwall of the Northern Snake Range MCC of eastern Nevada. While similar tectonic attenuation has also been documented in the basal parts of thrust sheets (Miller and Gans, 1989; Yonkee, 2005; Long and Kohn, 2020), the demonstrated axial planar relationship between S_1 and F_1 folding strongly suggests the Belt-Paleozoic section in Carpp Ridge has been thinned along the upper limb of the FRA.

NW-vergent recumbent folding was followed by WSW-vergent upright folding. Macroscopic F_2 folds such as the RCA refolded the FRA and associated structures, as well as the Georgetown thrust. Moderately SE-dipping axial planar S_2 cleavage and west-vergence observed in parasitic folds on the lower limb of the RCA suggest that this fold is west-verging, and we depict it as such on our A-A' section (Figure 18). West-vergence of F_1 and F_2 folds in the AMCC footwall has proven difficult to explain. The Cordilleran fold-thrust belt displays prominent east-vergence, and many workers (Baken, 1984; Lidke and Wallace, 1992; Wallace et al., 1992) have modeled west-vergence in this area in terms of fold-thrust belt mechanics. While this interpretation is certainly valid in some parts of the Anaconda and Flint Creek ranges, the propensity of ductile deformation and recumbent-folding in the broader AMCC footwall suggests that fold-thrust belt mechanics may not fully explain observed deformation.

In the Selkirk mountains of British Columbia, a prominent zone of structural divergence known as the Selkirk fan features SW-verging, hinterland-directed folds associated with distributed ductile deformation in the Omineca belt that transition to NE-verging, foreland-directed folds associated with thin-skinned thrusting (Gibson et al., 2008). A similar fan structure, however, has not been observed in the AMCC footwall or the broader Helena salient, and many workers in the southern Canadian Cordillera (Brown and Lane, 1988; Gibson et al., 2008) have interpreted SW-vergent folds in terms of terrane accretion along the western Laurentian margin. The AMCC is located inboard of Cordilleran accreted terranes, so this model likely does not apply.

Interestingly, the structure of the LISZ in the eastern Anaconda Range is reminiscent of double gneiss domes described in the Aegean (Kruckenberg et al., 2011), and the French Massif Central (Rey et al., 2011). In these settings, upper crustal extension is compensated by oppositely verging flows in the mid to lower crust. When these flows viscously collide, they rotate upward into two subdomes separated by a steep median high-strain zone. Unpublished N-S cross-sections across the LISZ suggest two sub-domes converging on a highly appressed syncline (Jeff Lonn, *pers. comm*.). The LISZ may therefore represent a steeply dipping median high-strain zone similar to those predicted by numerical models of Rey et al. (2011) and observed in gneiss domes of the Naxos metamorphic core complex by Kruckenberg et al. (2011). Extreme tectonic attenuation, high-grade metamorphism, and melt-present deformation in the LISZ documented by Grice (2006) suggest conditions amenable to gneiss dome formation existed in the AMCC footwall during Late Cretaceous time. Further, regional map patterns suggest that the southern sub-dome may be continuous with the FRA (Jeff Lonn, *pers. comm.*). Flood (1974) documented Prichard Formation in the core of the fold, and subsequent mapping has documented both the FRA fold axis and overturned limb in the Prichard Formation southeast of Carpp Ridge (Jeff Lonn, *pers comm.*) (Figure 2). North of the Anaconda detachment fault, overturned Prichard strata core a large, NE-SW oriented homocline involving the Lower Belt, Ravalli, Piegan, and Missoula groups (Figure 2), and this map pattern may reflect the FRA. Wallace et al. (1992) also interpreted the FRA as part of a larger dome on their C-C' cross section, and further suggested that the fold is part of a larger complex consisting of multiple large-scale recumbent folds. Further, our mapping strongly suggests that FRA-related deformation extends north of its previously mapped extent, although we were unable to locate the axial trace as Flood (1974) and Wallace et al. (1992) did, perhaps because rocks exposed in the Carpp Ridge area are at higher structural levels. Clearly, the FRA is a kilometer-scale fold, and due to its scale, is not depicted on our A-A' section. Given the relationship between large-scale recumbent folding and possible gneiss doming in the AMCC footwall, the FRA may have formed in response to buoyancy and/or isostasy driven flow during decompression of the Cordilleran middle crust. West-vergent folding was likely decoupled from regional, east-vergent tectonics, and instead formed in response to diapiric flow of partially molten crust in the LISZ. A kilometer-scale overturned "mega-fold" similar to the FRA was documented in the Hospitalet gneiss dome of the Pyrenees by Denele et al. (2007). Recumbent folding and doming in the high-grade metamorphic infrastructure were accompanied by tight, upright folding in low-grade metasediments of the superstructure. A similar relationship may exist between the FRA and upright F_2 folds in the AMCC footwall, as the two deformations are largely coaxial and fold axes of mesoscopic folds from both generations are SW-oriented. Regional map patterns also support this interpretation, with tight F_2 folds more pronounced to the north at higher structural levels (Figure 2).

Folding was followed by high-angle normal faulting along the Spruce Creek fault and NW-trending normal faults. The Spruce Creek fault is sub-parallel to several other normal faults to the east, including the Page Creek and Dry Creek faults. While the timing of motion along these structures is not well constrained, the Page Creek fault cuts the 51.87 Ma granodiorite east of Carpp Ridge and does not cut Quaternary glacial till (Lidke and Wallace, 1992). These faults may be coincident with either core complex extension, subsequent Basin and Range extension, or both.

Tectonic Implications

Given evidence for 55-65 km thick crust across Cordilleran hinterland (Gibson et al., 2008; Chapman et al., 2015; Fan et al., 2017), mid-crustal rocks of the AMCC footwall were likely situated within the interior of a high-elevation orogenic plateau ("Nevadaplano" of DeCelles (2004)) comparable to the modern Andean Altiplano and Tibetan Plateau. Widespread evidence for Late Cretaceous syn-convergent extension, decompression, and exhumation has been documented throughout the Cordilleran hinterland. Wells and Hoisch (2008) related rapid Late Cretaceous cooling, decompression, and extension across the Mojave sector of the Cordilleran hinterland to delamination of lithospheric mantle prior to low-angle subduction of the Farallon plate. In a similar vein, DeCelles et al. (2009) and DeCelles and Graham (2015) explained this extension in terms of a broader Cordilleran cycle, part of which involves the foundering of an eclogitic arc root following high flux in the Cordilleran magmatic arc. This foundering results in gravitational instability and upper-crustal extension in the hinterland. Alternatively, Long and Kohn (2020) related decompression from some of the same localities considered by Wells and Hoisch (2008) to distributed ductile thinning above the basal Cordilleran decollement. Just west of the LISZ, Grice (2006) and Foster et al. (2010) documented rapid Late Cretaceous cooling in the 74.6 Ma Storm Lake stock using $^{40}Ar/^{39}Ar$ thermochronology, suggesting that the pluton had cooled below ~350ºC by ~74 Ma. This cooling path is similar to those observed in the Mojave region by Wells and Hoisch (2008). Further, the presence of relict and fresh kyanite as well as a low pressure, high temperature sillimanite-grade assemblage associated with ~74-75 Ma deformation and anatexis in the LISZ suggest an episode of Late Cretaceous decompression in the AMCC footwall. While the timing and P-T conditions of the earlier kyanite assemblage are poorly constrained, thermobarometric results of Grice (2006) suggest at most 4 kilobars of decompression during Late Cretaceous time, and this is both roughly coincident with and of similar magnitude to Late Cretaceous decompression observed in footwall rocks of the Ruby-East Humboldt MCC (McGrew et al., 2000; Henry et al., 2011; Hallett and Spear, 2014; Hallett and Spear, 2015; Long and Kohn, 2020). Decompression and cooling in the AMCC footwall may very well be related to larger-scale tectonic processes operating across the Cordilleran hinterland. Further, Teyssier and Whitney (2002) related decompression initiated by thinning of thickened crust to partial melting and diapirism of hot, crustal material. They describe a positive feedback cycle beginning with crustal thinning, which results in decompression and generation of partial melt. This process leads to buoyant rising of thick, hot crust, which results in further decompression and partial melt (Norlander et al., 2002; Teyssier and Whitney, 2002). Gneiss domes cored by migmatite ± granite are the geological signature of this feedback cycle, and migmatites of the AMCC footwall may very well have formed in this manner in response to Late Cretaceous decompression in the Cordilleran hinterland.

Evidence for both lithospheric delamination and thrust sub-parallel distributed ductile thinning exist across the North American Cordilleran orogen, and while the question of which process played a larger role at the orogen-scale is beyond the scope of this study, gneiss dome formation in the AMCC could theoretically accompany both. Late Cretaceous upper crustal extension triggered by either delamination of lithospheric mantle or an eclogitic arc root could result in thinning of the mid-lower crust, causing decompression, partial melting, and gneiss-dome generation as described by Teyssier and Whitney (2002), Wells and Hoisch (2008), and DeCelles et al. (2009). Inboard migration of the Cordilleran magmatic arc and intrusion of the Late Cretaceous Idaho batholith and coeval plutons of the Helena salient may have provided the conditions necessary for the generation on an eclogitic arc root. Shallow emplacement of the 83-74 Ma Boulder batholith and eruption of the equivalent Elkhorn Mountains volcanics could be reflective of ignimbrite eruptions predicted by DeCelles et al. (2009) and DeCelles and Graham (2015) during upper crustal extension following arc root foundering. Late Cretaceous gneiss-doming in the AMCC footwall could therefore be interpreted as the mid-lower crustal equivalent of upper crustal extension. A significant limitation of this model is the lack of considerable Cretaceous-aged normal faulting in the region. Most normal faults in SW Montana are associated with either MCC-related or subsequent Basin and Range extension. Long and Kohn (2020) encountered a similar problem in Ruby-East Humboldt MCC, leading them to propose thrust sub-parallel distributed ductile thinning as a more viable explanation for Late Cretaceous tectonic attenuation, decompression, and exhumation of mid-crustal rocks. This model also provides the same constraints necessary for gneiss-dome generation, although distributed ductile thinning-related deformation is coupled to thrust-subparallel motion along the basal Cordilleran decollement. We posit that gneiss-doming and related formation of the FRA is decoupled from regional east-vergent tectonics, although it may have been a response to decompression associated with hinterland-wide distributed ductile thinning as discussed by Long and Kohn (2020). Detailed regional work is needed to more confidently evaluate the two models proposed here.

CONCLUSION

High-resolution geologic mapping in the Carpp Ridge 7.5’ quadrangle strongly suggests that the FRA attenuated Belt strata in the western AMCC footwall. S_1 fabrics in Piegan and Snowslip strata that attenuate, mylonitize, and boudinage section are roughly axial planar to F_1 folds. Bedding-parallel structures originally interpreted as out-of-sequence thrusts by Lidke and Wallace (1992) and detachments by Lonn and McDonald (2004) are reinterpreted as ductile thrusts associated with the FRA, although it is also possible that they are passive features related to flow of incompetent Snowslip and Piegan strata during F_1 folding. F_2 upright folds subsequently refolded structures and fabrics related to F_1, however, due to their coaxial nature, the two folding events may have occurred synchronously at different structural levels in a manner similar to that proposed by Denele et al. (2007). U-Pb geochronology of intrusive rocks from this study and Grice (2006) suggest that F_1 and F_2 folding are Late Cretaceous in age and may have accompanied development of the 75-74 Ma LISZ and pre-74 Ma Mill Creek nappe in the eastern Anaconda Range. Evidence for doming associated with the FRA paired with further evidence for a Naxos-style gneiss dome in the LISZ suggest that the NW-verging FRA may have developed in response to buoyancy and/or isostasy driven flow of the Cordilleran middle crust during a Late Cretaceous episode of decompression documented in high-grade rocks of the AMCC footwall and across the North America Cordillera orogen. This decompression may have been driven by mantle delamination, arc-root foundering, or distributed ductile thinning. While we can confidently posit that the FRA is responsible for tectonic attenuation in the Carpp Ridge area, integrative regional work is needed to constrain the connection between the LISZ and FRA, and to further test tectonic models suggested here.

REFERENCES CITED

Allen, J. C., 1966, Structure and Petrology of the Royal Stock, Flint Creek Range, Central-Western Montana: Geological Society of America Bulletin, v. 77, no. 3, p. 291-301.

Baken, J. F., 1984, The structural geology and tectonic history of the northern Flint Creek Range, western Montana: Bozeman, Montana State University, M.S. thesis, 140 p., map scale 1:50,000.

Baty, J. B., 1973, Fission track age dates from three granitic plutons in the Flint Creek Range, western Montana: Missoula, University of Montana, M.S. thesis, 43 p.

Brown, R. L., and Lane, L. S., 1988, Tectonic interpretation of west-verging folds in the Selkirk Allochthon of the southern Canadian Cordillera: Canadian Journal of Earth Sciences, v. 25, no. 2, p. 292-300.

Buckley, S. N., 1990, Ductile extension in a Late Cretaceous fold and thrust belt, Granite County, west-central Montana: Missoula, University of Montana, M.S. thesis, 42 p., map scale 1:6,000.

Burmester, R. F., Lonn, J. D., Lewis, R. S., McFaddan, M. D., MacLean, J. S., and Sears, J. W., 2016, Stratigraphy of the Lemhi subbasin of the Belt Supergroup, Belt Basin: Window to Mesoproterozoic Earth, Volume 522, Geological Society of America, p. 121-137.

Chapman, J. B., Ducea, M. N., Decelles, P. G., and Profeta, L., 2015, Tracking changes in crustal thickness during orogenic evolution with Sr/Y: An example from the North American Cordillera: Geology, v. 43, no. 10, p. 919-922.

Colgan, J. P., Howard, K. A., Fleck, R. J., and Wooden, J. L., 2010, Rapid middle Miocene extension and unroofing of the southern Ruby Mountains, Nevada: Tectonics, v. 29, no. 6.

Coney, P. J., Crittenden, M. D., Jr., Coney, P. J., and Davis, G. H., 1980, Cordilleran metamorphic core complexes: An overview, Cordilleran Metamorphic Core Complexes, Geological Society of America Memoir 153, 493 p.

Crittenden, M. D., Jr., Crittenden, M. D., Jr., Coney, P. J., and Davis, G. H., 1980, Metamorphic core complexes of the North American Cordillera: Summary, Cordilleran Metamorphic Core Complexes, Geological Society of America Memoir 153, 493 p.

Csejtey, B., 1968, Geology of the southeast flank of the Flint Creek Range, western Montana: Princeton, NJ, Princeton University, Ph.D. dissertation, 175 p., map scale 1:62,500.

Davis, G. H., and Coney, P. J., 1979, Geologic development of the Cordilleran metamorphic core complexes: Geology, v. 7, no. 3, p. 120-124.

DeCelles, P. G., 2004, Late Jurassic to Eocene evolution of the Cordilleran thrust belt and foreland basin system, western U.S.A: American Journal of Science, v. 304, no. 2, p.105-168.

DeCelles, P. G., Ducea, M. N., Kapp, P., and Zandt, G., 2009, Cyclicity in Cordilleran orogenic systems: Nature Geoscience, v. 2, no. 4, p. 251-257.

DeCelles, P. G., and Graham, S. A., 2015, Cyclical processes in the North American Cordilleran orogenic system: Geology, v. 43, no. 6, p. 499-502.

Denele, Y., Olivier, P., Gleizes, G., and Barbey, P., 2007, The Hospitalet gneiss dome (Pyrenees) revisited: Lateral flow during Variscan transpression in the middle crust: Terra Nova, v. 19, p. 445-453.

Desmarais, N. R., 1983, Geology and geochronology of the Chief Joseph plutonic-metamorphic complex, Idaho-Montana: Seattle, University of Washington, Ph.D. dissertation, 150 p., map scale 1:50,000.

Donath, F. A., and Parker, R. B., 1964, Folds and Folding: GSA Bulletin, v. 75, no. 1, p. 45-62.

Dudás, F. Ö., Ispolatov, V. O., Harlan, S. S., and Snee, L. W., 2010, 40Ar/39Ar Geochronology and Geochemical Reconnaissance of the Eocene Lowland Creek Volcanic Field, West-Central Montana: The Journal of Geology, v. 118, no. 3, p. 295-304.

Elliott, C. G., and Lonn, J. D., in review, Geologic map of the Long Peak 7.5’ quadrangle, southwestern Montana: Montana Bureau of Mines and Geology Open-File Report, 1 sheet, scale 1:24,000.

Elliott, C. G., Smith, L. N., and Lonn, J. D., 2013, Geologic map of the Mount Powell 7.5' quadrangle, southwestern Montana: Montana Bureau of Mines and Geology Open-File Report 635, 22 p., 1 sheet, scale 1:24,000.

Emmons, W. H., and Calkins, F. C., 1913, Geology and ore deposits of the Philipsburg quadrangle, Montana: U.S. Geological Survey Professional Paper 78, 300 p.

Fan, M., Constenius, K. N., and Dettman, D. L., 2017, Prolonged high relief in the northern Cordilleran orogenic front during middle and late Eocene extension based on stable isotope paleoaltimetry: Earth and Planetary Science Letters, v. 457, p. 376-384.

Flood, R. E., 1974, Structural geology of the upper Fishtrap Creek area, central Anaconda Range, Deer Lodge County, Montana: Missoula, University of Montana, M.S. thesis, 71 p., map scale 1:62,500.

Foster, D. A., Doughty, P. T., Kalakay, T. J., Fanning, C. M., Coyner, S., Grice, W. C., Vogl, J., Roeske, S. M., Till, A. B., and Sample, J. C., 2007, Kinematics and timing of exhumation of metamorphic core complexes along the Lewis and Clark fault zone, northern Rocky Mountains, USA, Exhumation Associated with Continental Strike-Slip Fault Systems, Volume 434, Geological Society of America, p. 207-232.

Foster, D. A., Grice, W. C., Jr., and Kalakay, T. J., 2010, Extension of the Anaconda metamorphic core complex: 40Ar/39Ar thermochronology and implications for Eocene tectonics of the northern Rocky Mountains and the Boulder batholith: Lithosphere, v. 2, no. 4, p. 232-246.

Gehrels, G. E., Valencia, V. A., and Ruiz, J., 2008, Enhanced precision, accuracy, efficiency, and spatial resolution of U-Pb ages by laser ablation–multicollector–inductively coupled plasma–mass spectrometry: Geochemistry, Geophysics, Geosystems, v. 9, no. 3.

Gibson, H. D., Brown, R. L., and Carr, S. D., 2008, Tectonic evolution of the Selkirk fan, southeastern Canadian Cordillera: A composite Middle Jurassic-Cretaceous orogenic structure: Tectonics, v. 27, no. 6.

Grice, W. C., Jr., 2006, Exhumation and cooling history of the Middle Eocene Anaconda metamorphic core complex, western Montana: Gainesville, University of Florida, M.S. thesis, 260 p., map scale 1:100,000.

Hallett, B. W., and Spear, F. S., 2014, The P–T History of Anatectic Pelites of the Northern East Humboldt Range, Nevada: Evidence for Tectonic Loading, Decompression, and Anatexis: Journal of Petrology, v. 55, no. 1, p. 3-36.

Hallett, B. W., and Spear, F. S., 2015, Monazite, zircon, and garnet growth in migmatitic pelites as a record of metamorphism and partial melting in the East Humboldt Range, Nevada: American Mineralogist, v. 100, no. 4, p. 951-972.

Harrison, J. E., Griggs, A. B., and Wells, J. D., 1974, Tectonic features of the Precambrian Belt Basin and their influence on post-Belt structures: U.S. Geological Survey Professional Paper 866, 15 p.

Heise, B. A., 1983, Structural geology of the Mt. Haggin area, Deer Lodge County, Montana: Missoula, University of Montana, M.S. thesis, 77 p., map scale 1:12,000.

Henry, C. D., McGrew, A. J., Colgan, J. P., Snoke, A. W., Brueseke, M. E., Lee, J., and Evans, J. P., 2011, Timing, distribution, amount, and style of Cenozoic extension in the northern Great Basin, Geologic Field Trips to the Basin and Range, Rocky Mountains, Snake River Plain, and Terranes of the U.S. Cordillera, Volume Geological Society of America Field Guide 21, p. 27-66.

Hirth, G., and Tullis, J., 1992, Dislocation creep regimes in quartz aggregates: Journal of Structural Geology, v. 14, no. 2, p. 145-159.

Horstwood, M. S. A., Košler, J., Gehrels, G., Jackson, S. E., McLean, N. M., Paton, C., Pearson, N. J., Sircombe, K., Sylvester, P., Vermeesch, P., Bowring, J. F., Condon, D. J., and Schoene, B., 2016, Community-Derived Standards for LA - ICP - MS U-(Th-)Pb Geochronology – Uncertainty Propagation, Age Interpretation and Data Reporting: Geostandards and Geoanalytical Research, v. 40, no. 3, p. 311-332.

Howlett, C. J., Reynolds, A. N., and Laskowski, A. K., 2020, Geologic map of the northern half of the Pintler Lake 7.5' quadrangle and the southern half of the Warren Peak 7.5' quadrangle, southwestern Montana: Montana Bureau of Mines and Geology EDMAP portion of the National Geologic Mapping Program 13, 1 sheet, scale 1:24,000.

Howlett, C. J., Reynolds, A. N., and Laskowski, A. K., 2021, Magmatism and Extension in the Anaconda Metamorphic Core Complex of Western Montana and Relation to Regional Tectonics: Tectonics, v. 40, no. 9.

Hyndman, D. W., Crittenden, M. D., Jr., Coney, P. J., and Davis, G. H., 1980, Bitterroot dome-Sapphire tectonic block, an example of a plutonic-core gneiss-dome complex with its detached suprastructure, Cordilleran Metamorphic Core Complexes, Geological Society of America Memoir 153, 493 p.

Hyndman, D. W., Obradovich, J. D., and Ehinger, R., 1972, Potassium-Argon Age Determinations of the Philipsburg Batholith: GSA Bulletin, v. 83, no. 2, p. 473-474.

Kalakay, T. J., Foster, D. A., Lonn, J. D., Shaw, C. A., and Tikoff, B., 2014, Polyphase collapse of the Cordilleran hinterland: The Anaconda metamorphic core complex of western Montana—The Snoke symposium field trip, Exploring the Northern Rocky Mountains, Volume 37, Geological Society of America, p. 145-158.

Kalakay, T. J., John, B. E., and Lageson, D. R., 2001, Fault-controlled pluton emplacement in the Sevier fold-and-thrust belt of southwest Montana, USA: Journal of Structural Geology, v. 23, no. 6, p. 1151-1165.

Kruckenberg, S. C., Vanderhaeghe, O., Ferré, E. C., Teyssier, C., and Whitney, D. L., 2011, Flow of partially molten crust and the internal dynamics of a migmatite dome, Naxos, Greece: Tectonics, v. 30, no. 3.

Lageson, D. R., Schmitt, J. G., Horton, B. K., Kalakay, T. J., and Burton, B. R., 2001, Influence of Late Cretaceous magmatism on the Sevier orogenic wedge, western Montana: Geology, v. 29, no. 8, p. 723-726.

Lidke, D. J., and Wallace, C. A., 1992, Rocks and structure of the north-central part of the Anaconda Range, Deer Lodge and Granite Counties, Montana: U.S. Geological Survey Bulletin 1993, 31 p., scale 1:24,000.

Long, S. P., and Kohn, M. J., 2020, Distributed ductile thinning during thrust emplacement: A commonly overlooked exhumation mechanism: Geology, v. 48, no. 4, p. 368-373.

Lonn, J., and Johnson, L., 2010, Cretaceous structures and mineralization in the footwall of the Eocene Anaconda detachment fault, Montana: A field trip along Warm Springs Creek: Northwest Geology, v. 39, p. 57-68.

Lonn, J., and Lewis, R., 2009, Late Cretaceous extension and its relation to the thin stratigraphic section in the Philipsburg region: A field trip to Carpp Ridge: Northwest Geology, v. 38, p. 141-152.

Lonn, J., and McDonald, C., 2004, Geologic map of the Kelly Lake 7.5' quadrangle, western Montana: Montana Bureau of Mines and Geology Open-File Report 500, 15 p., 1 sheet, scale 1:24,000.

Lonn, J. D., McDonald, C., Lewis, R. S., Kalakay, T. J., O'Neill, J. M., Berg, R. B., and Hargrave, P., 2003, Geologic map of the Philipsburg 30' x 60' quadrangle, western Montana: Montana Bureau of Mines and Geology Open-File Report 483, 1 sheet, scale 1:100,000.

Maccready, T., Snoke, A. W., Wright, J. E., and Howard, K. A., 1997, Mid-crustal flow during Tertiary extension in the Ruby Mountains core complex, Nevada: Geological Society of America Bulletin, v. 109, no. 12, p. 1576-1594.

Mattinson, J. M., 2010, Analysis of the relative decay constants of 235U and 238U by multi-step CA-TIMS measurements of closed-system natural zircon samples: Chemical Geology, v. 275, no. 3, p. 186-198.

McGrew, A. J., Peters, M. T., and Wright, J. E., 2000, Thermobarometric constraints on the tectonothermal evolution of the East Humboldt Range metamorphic core complex, Nevada: Geological Society of America Bulletin, v. 112, p. 45-60.

Miller, E. L., and Gans, P. B., 1989, Cretaceous crustal structure and metamorphism in the hinterland of the Sevier thrust belt, western U.S. Cordillera: Geology, v. 17, no. 1, p. 59-62.

Naibert, T. J., Geissman, J. W., and Heizler, M. T., 2010, Magnetic fabric, paleomagnetic, and 40Ar/39Ar geochronologic data bearing on the emplacement of the Late Cretaceous Philipsburg Batholith, SW Montana fold-and-thrust belt: Lithosphere, v. 2, no. 5, p. 303-327.

Norlander, B. H., Whitney, D. L., Teyssier, C., and Vanderhaeghe, O., 2002, Partial melting and decompression of the Thor-Odin dome, Shuswap metamorphic core complex, Canadian Cordillera: Lithos, v. 61, no. 3, p. 103-125.

O'Neill, J. M., Schmidt, C. J., and Genovese, P. W., 1990, Dillon cutoff-Basement-involved tectonic link between the disturbed belt of west-central Montana and the overthrust belt of extreme southwestern Montana: Geology, v. 18, no. 11, p. 1107-1110.

O’Neill, J. M., Lonn, J. D., Lageson, D. R., and Kunk, M. J., 2004, Early Tertiary Anaconda Metamorphic Core Complex, southwestern Montana: Canadian Journal of Earth Sciences, v. 41, no. 1, p. 63-72.

Platt, J. P., Behr, W. M., and Cooper, F. J., 2015, Metamorphic core complexes: windows into the mechanics and rheology of the crust: Journal of the Geological Society, v. 172, no. 1, p. 9-27.

Poulter, G. J., 1956, Geologic map and sections of Georgetown trust area : Granite and Deer Lodge counties, Montana: Butte, MT : Montana Bureau of Mines and Geology Geologic Map GM 1, scale 1:48,000.

Ramsay, J. G., 1967, Folding and fracturing of rocks: Mc Graw Hill Book Company, v. 568.

Rey, P. F., Teyssier, C., Kruckenberg, S. C., and Whitney, D. L., 2011, Viscous collision in channel explains double domes in metamorphic core complexes: Geology, v. 39, no. 4, p. 387-390.

Schmidt, C. J., and O’Neill, J. M., 1982, Structural evolution of the southwest Montana transverse zone. In: Blake, R. (Ed.), Geologic Studies of the Cordilleran Thrust Belt 1, Rocky Mountain Association of Geologists Field Guidebook, vol. 1, p. 193-218.

Sloss, L. L., 1963, Sequences in the Cratonic Interior of North America: GSA Bulletin, v. 74, no. 2, p. 93-114.

Stipp, M., Stünitz, H., Heilbronner, R., and Schmid, S., 2002, Dynamic recrystallization of quartz: Correlation between natural and experimental conditions: Geological Society of London Special Publications, v. 200, p. 171-190.

Teyssier, C., and Whitney, D. L., 2002, Gneiss domes and orogeny: Geology, v. 30, no. 12, p. 1139-1142.

Wallace, C. A., Lidke, D. J., Elliott, J. E., Desmarais, N. R., Obradovich, J. D., Lopez, D. A., Zarske, S. E., Heise, B. A., Blaskowski, M. J., and Loen, J. S., 1992, Geologic map of the Anaconda-Pintlar wilderness and contiguous roadless area, Granite, Deer Lodge, Beaverhead, and Ravalli counties, western Montana: U.S. Geological Survey Miscellaneous Field Studies map MF-1633-C, 36 p., map scale 1:50,000.

Wallace, C. A., Lidke, D. J., and Schmidt, R. G., 1990, Faults of the central part of the Lewis and Clark line and fragmentation of the Late Cretaceous foreland basin in west-central Montana: GSA Bulletin, v. 102, no. 8, p. 1021-1037.

Wells, M. L., and Hoisch, T. D., 2008, The role of mantle delamination in widespread Late Cretaceous extension and magmatism in the Cordilleran orogen, western United States: Geological Society of America Bulletin, v. 120, no. 5-6, p. 515-530.

Wernicke, B., 1981, Low-angle normal faults in the Basin and Range Province: nappe tectonics in an extending orogen: Nature, v. 291, no. 5817, p. 645-648.

Winston, D., Smith, S. V., MacLean, J. S., and Sears, J. W., 2016, Crinkle cracks in the Proterozoic Piegan Group, Belt Supergroup, Montana and Idaho: A descriptive style of sand-filled cracks hypothetically formed by subaqueous solitary-like waves, Belt Basin: Window to Mesoproterozoic Earth, Volume 522, Geological Society of America, p. 57-69.

Wiswall, C. G., 1976, Structural styles of the southern boundary of the Sapphire tectonic block, Anaconda-Pintlar Wilderness Area, Montana: Missoula, University of Montana, M.S. thesis, 62 p., map scale 1:48,000.

Wrobel, A. J., Gans, P. B., and Womer, J. B., 2021, Late Cretaceous Crustal Shortening in the Northern Snake Range Metamorphic Core Complex: Constraints on the Structural Geometry and Magnitude of Pre-Extensional Footwall Burial: Tectonics, v. 40, no. 8.

Yonkee, A., 2005, Strain patterns within part of the Willard thrust sheet, Idaho–Utah–Wyoming thrust belt: Journal of Structural Geology, v. 27, no. 7, p. 1315-1343.

CHAPTER THREE

GENERAL CONCLUSION

New geologic mapping and structural analysis of the Belt-Paleozoic section in the Carpp Ridge 7.5’ quadrangle strongly suggest that the NW-vergent Fishtrap recumbent anticline (FRA) attenuated strata in the western footwall of the Anaconda metamorphic core complex (AMCC). Bedding-parallel fabrics in the Piegan-Missoula Group section previously interpreted in terms of out-of-sequence thrusting (Lidke and Wallace, 1992; Wallace et al., 1992) and detachment faulting during Late Cretaceous synorogenic extension (Lonn et al., 2003; Lonn and McDonald, 2004; Lonn and Lewis, 2009) are reinterpreted as S_1 fabrics with a demonstrated axial planar relationship to the F_1 FRA. These fabrics are sub-parallel to larger-scale bedding-parallel faults and shear zones that thin and omit section in the Missoula and Piegan groups, leading us to interpret them as either west-directed ductile nappe thrusts as suggested by the Cutaway nappe thrust (CNT), or passive surfaces that accommodated ductile flow of incompetent argillitic strata in the upper limb of the FRA. This ductile flow may have been enhanced by more competent quartzites of the Missoula and Ravalli groups that “sandwiched” argillites of the Piegan Group and Snowslip Formation during F_1 recumbent folding. S_1 fabrics and perhaps the FRA itself are refolded by a series of F_2 west-vergent upright folds, most notably the Rock Creek anticline (RCA). An S_2 axial planar cleavage is well-developed in the Mt. Shields Formation along the limbs of the RCA, and this cleavage is axial planar to mesoscopic west-verging folds in the Dexter Basin area. The >75 Ma Georgetown thrust (Naibert et al., 2010) is folded by the RCA, suggesting that the thrust may be folded by the FRA at deeper structural levels, although this relationship has never been observed. The Georgetown thrust and subsequent F_1 and F_2 folds are crosscut by a series of brittle normal faults likely associated with the larger Page Creek and Dry Creek faults to the east.

U-Pb zircon dates from cross-cutting igneous intrusions further constrain the timing of deformation in the Carpp Ridge area and the broader AMCC footwall. A 52.87 Ma granodiorite dike crosscuts the F_2 RCA, indicating that F_2 folding is older than ~53 Ma. In the FRA hinge zone just south of the field area, a slightly foliated 51.87 Ma granodiorite stock intrudes Piegan strata with well-developed S_1 fabrics. The granodiorite foliation is locally proto-mylonitic and sub-parallel to S_1 fabrics, initially suggesting a synkinematic relationship between the stock and the FRA. Detailed investigation of the granodiorite, however, reveals the intrusion to be largely non-foliated, and at one locality, the stock crosscuts S_1 mylonitic fabrics in the Piegan Group. Therefore, we posit that F_1 folding is older than ~52 Ma, and that the fabrics observed in the granodiorite are not reflective of regional tectonics. They may instead represent localized reactivation of the FRA during AMCC extension. While no upper limit on the age of deformation was identified in the field area, tectonic attenuation and nappe folding in the Lake of the Isle shear zone (LISZ) were dated to between 75-74 Ma and >74 Ma respectively by Grice (2006) on the basis of foliated and cross-cutting Late Cretaceous intrusions. Given the similarities between structural styles observed in the LISZ and the Carpp Ridge area, we infer that F_1 and F_2 folding are Late Cretaceous in age.

The FRA is clearly a kilometer-scale fold that involves the entire Belt Supergroup exposed in the AMCC footwall. Deformation associated with the fold extends north of the axial trace mapped by Flood (1974) and Wallace et al. (1992), and the overturned limb is exposed southeast of Carpp Ridge in the Prichard formation. Regional map patterns suggest that the Belt section in the AMCC footwall is part of a much larger north dipping homocline cored by the Prichard formation, and this geometry may reflect the FRA. Wallace et al. (1992) interpreted the fold as a domal structure, and cross sections perpendicular to the LISZ suggest that that FRA could be continuous with the southern sub-dome of a double-gneiss dome similar to those observed in the Aegean and the French Massif Central (Kruckenberg et al., 2011; Rey et al., 2011) (Jeff Lonn, *pers. comm.*). Kilometer-scale folding similar to the FRA has also been related to doming in the Hospitalet gneiss dome of the Pyrenees (Denele et al., 2007).

While gneiss domes often form during core complex extension, tectonic attenuation and doming in the LISZ is clearly Late Cretaceous in age, preceding development of the AMCC by ~20 Ma. High-grade metamorphic mineral assemblages and melt-present deformation in Belt-Paleozoic strata of the LISZ, as well as biotite $^{40}Ar/^{39}Ar$ thermochronology data from the Storm Lake stock clearly indicate a Late Cretaceous phase of decompression, migmatite generation, and exhumation in AMCC footwall rocks. This is consistent with crustal conditions amenable to gneiss doming described by Teyssier and Whitney (2002) and Norlander et al. (2002). This decompression may have been driven by upper crustal extension related to delamination of lithospheric mantle prior to the onset of flat-slab subduction (Wells and Hoisch, 2008), foundering of an eclogitic arc-root beneath the Cordilleran magmatic arc of SW Montana (DeCelles et al., 2009; DeCelles and Graham, 2015), and/or thrust sub-parallel distributed ductile thinning along the basal Cordilleran decollement (Long and Kohn, 2020). At this time, we prefer the former two interpretations, as west-vergent folding in the FRA is likely decoupled from regional east-vergent tectonics and may instead be related to doming in the LISZ.

Based on the conclusions we have come to in this contribution, several avenues for future research exist in the AMCC footwall. Further detailed mapping and structural analysis is needed to better constrain the connection between the FRA and the LISZ. The nature of planar and linear fabrics is variable throughout the AMCC footwall, and particular attention should be paid to how fabrics change and interact at different structural levels. Further, while thermobarometric and geochronologic work of Grice (2006) constrained the P-T-t conditions of amphibolite facies high-temperature metamorphism in the LISZ, no work has been done to constrain the conditions and timing of previous high pressure metamorphism suggested by relict and fresh kyanite. Continued metamorphic thermobarometry work paired with other methods such as monazite petrochronology may help to further refine the timing and magnitude of Late Cretaceous decompression in the LISZ. To further test ideas proposed here about lithospheric and asthenospheric dynamics in the Montana segment of the North American Cordillera, we recommend detailed geochemical study of Late Cretaceous magmatic arc rocks exposed in and around the AMCC footwall. Xenolith petrology and thermobarometry in particular are sorely needed to better constrain deep-crustal and mantle conditions in this region during Cordilleran orogenesis.

REFERENCES CITED

DeCelles, P. G., Ducea, M. N., Kapp, P., and Zandt, G., 2009, Cyclicity in Cordilleran orogenic systems: Nature Geoscience, v. 2, no. 4, p. 251-257.

DeCelles, P. G., and Graham, S. A., 2015, Cyclical processes in the North American Cordilleran orogenic system: Geology, v. 43, no. 6, p. 499-502.

Denele, Y., Olivier, P., Gleizes, G., and Barbey, P., 2007, The Hospitalet gneiss dome (Pyrenees) revisited: Lateral flow during Variscan transpression in the middle crust: Terra Nova, v. 19, p. 445-453.

Flood, R. E., 1974, Structural geology of the upper Fishtrap Creek area, central Anaconda Range, Deer Lodge County, Montana: Missoula, University of Montana, M.S. thesis, 71 p., map scale 1:62,500.

Grice, W. C., Jr., 2006, Exhumation and cooling history of the Middle Eocene Anaconda metamorphic core complex, western Montana: Gainesville, University of Florida, M.S. thesis, 260 p., map scale 1:100,000.

Kruckenberg, S. C., Vanderhaeghe, O., Ferré, E. C., Teyssier, C., and Whitney, D. L., 2011, Flow of partially molten crust and the internal dynamics of a migmatite dome, Naxos, Greece: Tectonics, v. 30, no. 3.

Lidke, D. J., and Wallace, C. A., 1992, Rocks and structure of the north-central part of the Anaconda Range, Deer Lodge and Granite Counties, Montana: U.S. Geological Survey Bulletin 1993, 31 p., scale 1:24,000.

Long, S. P., and Kohn, M. J., 2020, Distributed ductile thinning during thrust emplacement: A commonly overlooked exhumation mechanism: Geology, v. 48, no. 4, p. 368-373.

Lonn, J., and Lewis, R., 2009, Late Cretaceous extension and its relation to the thin stratigraphic section in the Philipsburg region: A field trip to Carpp Ridge: Northwest Geology, v. 38, p. 141-152.

Lonn, J., and McDonald, C., 2004, Geologic map of the Kelly Lake 7.5' quadrangle, western Montana: Montana Bureau of Mines and Geology Open-File Report 500, 15 p., 1 sheet, scale 1:24,000.

Lonn, J. D., McDonald, C., Lewis, R. S., Kalakay, T. J., O'Neill, J. M., Berg, R. B., and Hargrave, P., 2003, Geologic map of the Philipsburg 30' x 60' quadrangle, western Montana: Montana Bureau of Mines and Geology Open-File Report 483, 1 sheet, scale 1:100,000.

Naibert, T. J., Geissman, J. W., and Heizler, M. T., 2010, Magnetic fabric, paleomagnetic, and 40Ar/39Ar geochronologic data bearing on the emplacement of the Late Cretaceous Philipsburg Batholith, SW Montana fold-and-thrust belt: Lithosphere, v. 2, no. 5, p. 303-327.

Norlander, B. H., Whitney, D. L., Teyssier, C., and Vanderhaeghe, O., 2002, Partial melting and decompression of the Thor-Odin dome, Shuswap metamorphic core complex, Canadian Cordillera: Lithos, v. 61, no. 3, p. 103-125.

Rey, P. F., Teyssier, C., Kruckenberg, S. C., and Whitney, D. L., 2011, Viscous collision in channel explains double domes in metamorphic core complexes: Geology, v. 39, no. 4, p. 387-390.

Teyssier, C., and Whitney, D. L., 2002, Gneiss domes and orogeny: Geology, v. 30, no. 12, p. 1139-1142.

Wallace, C. A., Lidke, D. J., Elliott, J. E., Desmarais, N. R., Obradovich, J. D., Lopez, D. A., Zarske, S. E., Heise, B. A., Blaskowski, M. J., and Loen, J. S., 1992, Geologic map of the Anaconda-Pintlar wilderness and contiguous roadless area, Granite, Deer Lodge, Beaverhead, and Ravalli counties, western Montana: U.S. Geological Survey Miscellaneous Field Studies map MF-1633-C, 36 p., map scale 1:50,000.

Wells, M. L., and Hoisch, T. D., 2008, The role of mantle delamination in widespread Late Cretaceous extension and magmatism in the Cordilleran orogen, western United States: Geological Society of America Bulletin, v. 120, no. 5-6, p. 515-530.

CUMULATIVE REFERENCES CITED

Allen, J. C., 1966, Structure and Petrology of the Royal Stock, Flint Creek Range, Central-Western Montana: Geological Society of America Bulletin, v. 77, no. 3, p. 291-301.

Baken, J. F., 1984, The structural geology and tectonic history of the northern Flint Creek Range, western Montana: Bozeman, Montana State University, M.S. thesis, 140 p., map scale 1:50,000.

Baty, J. B., 1973, Fission track age dates from three granitic plutons in the Flint Creek Range, western Montana: Missoula, University of Montana, M.S. thesis, 43 p.

Brown, R. L., and Lane, L. S., 1988, Tectonic interpretation of west-verging folds in the Selkirk Allochthon of the southern Canadian Cordillera: Canadian Journal of Earth Sciences, v. 25, no. 2, p. 292-300.

Buckley, S. N., 1990, Ductile extension in a Late Cretaceous fold and thrust belt, Granite County, west-central Montana: Missoula, University of Montana, M.S. thesis, 42 p., map scale 1:6,000.

Burmester, R. F., Lonn, J. D., Lewis, R. S., McFaddan, M. D., MacLean, J. S., and Sears, J. W., 2016, Stratigraphy of the Lemhi subbasin of the Belt Supergroup, Belt Basin: Window to Mesoproterozoic Earth, Volume 522, Geological Society of America, p. 121-137.

Chapman, J. B., Ducea, M. N., Decelles, P. G., and Profeta, L., 2015, Tracking changes in crustal thickness during orogenic evolution with Sr/Y: An example from the North American Cordillera: Geology, v. 43, no. 10, p. 919-922.

Colgan, J. P., Howard, K. A., Fleck, R. J., and Wooden, J. L., 2010, Rapid middle Miocene extension and unroofing of the southern Ruby Mountains, Nevada: Tectonics, v. 29, no. 6.

Coney, P. J., Crittenden, M. D., Jr., Coney, P. J., and Davis, G. H., 1980, Cordilleran metamorphic core complexes: An overview, Cordilleran Metamorphic Core Complexes, Geological Society of America Memoir 153, 493 p.

Crittenden, M. D., Jr., Crittenden, M. D., Jr., Coney, P. J., and Davis, G. H., 1980, Metamorphic core complexes of the North American Cordillera: Summary, Cordilleran Metamorphic Core Complexes, Geological Society of America Memoir 153, 493 p.

Csejtey, B., 1968, Geology of the southeast flank of the Flint Creek Range, western Montana: Princeton, NJ, Princeton University, Ph.D. dissertation, 175 p., map scale 1:62,500.

Davis, G. H., and Coney, P. J., 1979, Geologic development of the Cordilleran metamorphic core complexes: Geology, v. 7, no. 3, p. 120-124.

DeCelles, P. G., 2004, Late Jurassic to Eocene evolution of the Cordilleran thrust belt and foreland basin system, western U.S.A: American Journal of Science, v. 304, no. 2, p.105-168.

DeCelles, P. G., Ducea, M. N., Kapp, P., and Zandt, G., 2009, Cyclicity in Cordilleran orogenic systems: Nature Geoscience, v. 2, no. 4, p. 251-257.

DeCelles, P. G., and Graham, S. A., 2015, Cyclical processes in the North American Cordilleran orogenic system: Geology, v. 43, no. 6, p. 499-502.

Denele, Y., Olivier, P., Gleizes, G., and Barbey, P., 2007, The Hospitalet gneiss dome (Pyrenees) revisited: Lateral flow during Variscan transpression in the middle crust: Terra Nova, v. 19, p. 445-453.

Desmarais, N. R., 1983, Geology and geochronology of the Chief Joseph plutonic-metamorphic complex, Idaho-Montana: Seattle, University of Washington, Ph.D. dissertation, 150 p., map scale 1:50,000.

Donath, F. A., and Parker, R. B., 1964, Folds and Folding: GSA Bulletin, v. 75, no. 1, p. 45-62.

Dudás, F. Ö., Ispolatov, V. O., Harlan, S. S., and Snee, L. W., 2010, 40Ar/39Ar Geochronology and Geochemical Reconnaissance of the Eocene Lowland Creek Volcanic Field, West-Central Montana: The Journal of Geology, v. 118, no. 3, p. 295-304.

Elliott, C. G., and Lonn, J. D., in review, Geologic map of the Long Peak 7.5’ quadrangle, southwestern Montana: Montana Bureau of Mines and Geology Open-File Report, 1 sheet, scale 1:24,000.

Elliott, C. G., Smith, L. N., and Lonn, J. D., 2013, Geologic map of the Mount Powell 7.5' quadrangle, southwestern Montana: Montana Bureau of Mines and Geology Open-File Report 635, 22 p., 1 sheet, scale 1:24,000.

Emmons, W. H., and Calkins, F. C., 1913, Geology and ore deposits of the Philipsburg quadrangle, Montana: U.S. Geological Survey Professional Paper 78, 300 p.

Fan, M., Constenius, K. N., and Dettman, D. L., 2017, Prolonged high relief in the northern Cordilleran orogenic front during middle and late Eocene extension based on stable isotope paleoaltimetry: Earth and Planetary Science Letters, v. 457, p. 376-384.

Flood, R. E., 1974, Structural geology of the upper Fishtrap Creek area, central Anaconda Range, Deer Lodge County, Montana: Missoula, University of Montana, M.S. thesis, 71 p., map scale 1:62,500.

Foster, D. A., Doughty, P. T., Kalakay, T. J., Fanning, C. M., Coyner, S., Grice, W. C., Vogl, J., Roeske, S. M., Till, A. B., and Sample, J. C., 2007, Kinematics and timing of exhumation of metamorphic core complexes along the Lewis and Clark fault zone, northern Rocky Mountains, USA, Exhumation Associated with Continental Strike-Slip Fault Systems, Volume 434, Geological Society of America, p. 207-232.

Foster, D. A., Grice, W. C., Jr., and Kalakay, T. J., 2010, Extension of the Anaconda metamorphic core complex: 40Ar/39Ar thermochronology and implications for Eocene tectonics of the northern Rocky Mountains and the Boulder batholith: Lithosphere, v. 2, no. 4, p. 232-246.

Gehrels, G. E., Valencia, V. A., and Ruiz, J., 2008, Enhanced precision, accuracy, efficiency, and spatial resolution of U-Pb ages by laser ablation–multicollector–inductively coupled plasma–mass spectrometry: Geochemistry, Geophysics, Geosystems, v. 9, no. 3.

Gibson, H. D., Brown, R. L., and Carr, S. D., 2008, Tectonic evolution of the Selkirk fan, southeastern Canadian Cordillera: A composite Middle Jurassic-Cretaceous orogenic structure: Tectonics, v. 27, no. 6.

Grice, W. C., Jr., 2006, Exhumation and cooling history of the Middle Eocene Anaconda metamorphic core complex, western Montana: Gainesville, University of Florida, M.S. thesis, 260 p., map scale 1:100,000.

Hallett, B. W., and Spear, F. S., 2014, The P–T History of Anatectic Pelites of the Northern East Humboldt Range, Nevada: Evidence for Tectonic Loading, Decompression, and Anatexis: Journal of Petrology, v. 55, no. 1, p. 3-36.

Hallett, B. W., and Spear, F. S., 2015, Monazite, zircon, and garnet growth in migmatitic pelites as a record of metamorphism and partial melting in the East Humboldt Range, Nevada: American Mineralogist, v. 100, no. 4, p. 951-972.

Harrison, J. E., Griggs, A. B., and Wells, J. D., 1974, Tectonic features of the Precambrian Belt Basin and their influence on post-Belt structures: U.S. Geological Survey Professional Paper 866, 15 p.

Heise, B. A., 1983, Structural geology of the Mt. Haggin area, Deer Lodge County, Montana: Missoula, University of Montana, M.S. thesis, 77 p., map scale 1:12,000.

Henry, C. D., McGrew, A. J., Colgan, J. P., Snoke, A. W., Brueseke, M. E., Lee, J., and Evans, J. P., 2011, Timing, distribution, amount, and style of Cenozoic extension in the northern Great Basin, Geologic Field Trips to the Basin and Range, Rocky Mountains, Snake River Plain, and Terranes of the U.S. Cordillera, Volume Geological Society of America Field Guide 21, p. 27-66.

Hirth, G., and Tullis, J., 1992, Dislocation creep regimes in quartz aggregates: Journal of Structural Geology, v. 14, no. 2, p. 145-159.

Horstwood, M. S. A., Košler, J., Gehrels, G., Jackson, S. E., McLean, N. M., Paton, C., Pearson, N. J., Sircombe, K., Sylvester, P., Vermeesch, P., Bowring, J. F., Condon, D. J., and Schoene, B., 2016, Community-Derived Standards for LA - ICP - MS U-(Th-)Pb Geochronology – Uncertainty Propagation, Age Interpretation and Data Reporting: Geostandards and Geoanalytical Research, v. 40, no. 3, p. 311-332.

Howlett, C. J., Reynolds, A. N., and Laskowski, A. K., 2020, Geologic map of the northern half of the Pintler Lake 7.5' quadrangle and the southern half of the Warren Peak 7.5' quadrangle, southwestern Montana: Montana Bureau of Mines and Geology EDMAP portion of the National Geologic Mapping Program 13, 1 sheet, scale 1:24,000.

Howlett, C. J., Reynolds, A. N., and Laskowski, A. K., 2021, Magmatism and Extension in the Anaconda Metamorphic Core Complex of Western Montana and Relation to Regional Tectonics: Tectonics, v. 40, no. 9.

Hyndman, D. W., Crittenden, M. D., Jr., Coney, P. J., and Davis, G. H., 1980, Bitterroot dome-Sapphire tectonic block, an example of a plutonic-core gneiss-dome complex with its detached suprastructure, Cordilleran Metamorphic Core Complexes, Geological Society of America Memoir 153, 493 p.

Hyndman, D. W., Obradovich, J. D., and Ehinger, R., 1972, Potassium-Argon Age Determinations of the Philipsburg Batholith: GSA Bulletin, v. 83, no. 2, p. 473-474.

Kalakay, T. J., Foster, D. A., Lonn, J. D., Shaw, C. A., and Tikoff, B., 2014, Polyphase collapse of the Cordilleran hinterland: The Anaconda metamorphic core complex of western Montana—The Snoke symposium field trip, Exploring the Northern Rocky Mountains, Volume 37, Geological Society of America, p. 145-158.

Kalakay, T. J., John, B. E., and Lageson, D. R., 2001, Fault-controlled pluton emplacement in the Sevier fold-and-thrust belt of southwest Montana, USA: Journal of Structural Geology, v. 23, no. 6, p. 1151-1165.

Kruckenberg, S. C., Vanderhaeghe, O., Ferré, E. C., Teyssier, C., and Whitney, D. L., 2011, Flow of partially molten crust and the internal dynamics of a migmatite dome, Naxos, Greece: Tectonics, v. 30, no. 3.

Lageson, D. R., Schmitt, J. G., Horton, B. K., Kalakay, T. J., and Burton, B. R., 2001, Influence of Late Cretaceous magmatism on the Sevier orogenic wedge, western Montana: Geology, v. 29, no. 8, p. 723-726.

Lidke, D. J., and Wallace, C. A., 1992, Rocks and structure of the north-central part of the Anaconda Range, Deer Lodge and Granite Counties, Montana: U.S. Geological Survey Bulletin 1993, 31 p., scale 1:24,000.

Long, S. P., and Kohn, M. J., 2020, Distributed ductile thinning during thrust emplacement: A commonly overlooked exhumation mechanism: Geology, v. 48, no. 4, p. 368-373.

Lonn, J., and Johnson, L., 2010, Cretaceous structures and mineralization in the footwall of the Eocene Anaconda detachment fault, Montana: A field trip along Warm Springs Creek: Northwest Geology, v. 39, p. 57-68.

Lonn, J., and Lewis, R., 2009, Late Cretaceous extension and its relation to the thin stratigraphic section in the Philipsburg region: A field trip to Carpp Ridge: Northwest Geology, v. 38, p. 141-152.

Lonn, J., and McDonald, C., 2004, Geologic map of the Kelly Lake 7.5' quadrangle, western Montana: Montana Bureau of Mines and Geology Open-File Report 500, 15 p., 1 sheet, scale 1:24,000.

Lonn, J. D., McDonald, C., Lewis, R. S., Kalakay, T. J., O'Neill, J. M., Berg, R. B., and Hargrave, P., 2003, Geologic map of the Philipsburg 30' x 60' quadrangle, western Montana: Montana Bureau of Mines and Geology Open-File Report 483, 1 sheet, scale 1:100,000.

Maccready, T., Snoke, A. W., Wright, J. E., and Howard, K. A., 1997, Mid-crustal flow during Tertiary extension in the Ruby Mountains core complex, Nevada: Geological Society of America Bulletin, v. 109, no. 12, p. 1576-1594.

Mattinson, J. M., 2010, Analysis of the relative decay constants of 235U and 238U by multi-step CA-TIMS measurements of closed-system natural zircon samples: Chemical Geology, v. 275, no. 3, p. 186-198.

McGrew, A. J., Peters, M. T., and Wright, J. E., 2000, Thermobarometric constraints on the tectonothermal evolution of the East Humboldt Range metamorphic core complex, Nevada: Geological Society of America Bulletin, v. 112, p. 45-60.

Miller, E. L., and Gans, P. B., 1989, Cretaceous crustal structure and metamorphism in the hinterland of the Sevier thrust belt, western U.S. Cordillera: Geology, v. 17, no. 1, p. 59-62.

Naibert, T. J., Geissman, J. W., and Heizler, M. T., 2010, Magnetic fabric, paleomagnetic, and 40Ar/39Ar geochronologic data bearing on the emplacement of the Late Cretaceous Philipsburg Batholith, SW Montana fold-and-thrust belt: Lithosphere, v. 2, no. 5, p. 303-327.

Norlander, B. H., Whitney, D. L., Teyssier, C., and Vanderhaeghe, O., 2002, Partial melting and decompression of the Thor-Odin dome, Shuswap metamorphic core complex, Canadian Cordillera: Lithos, v. 61, no. 3, p. 103-125.

O'Neill, J. M., Schmidt, C. J., and Genovese, P. W., 1990, Dillon cutoff-Basement-involved tectonic link between the disturbed belt of west-central Montana and the overthrust belt of extreme southwestern Montana: Geology, v. 18, no. 11, p. 1107-1110.

O’Neill, J. M., Lonn, J. D., Lageson, D. R., and Kunk, M. J., 2004, Early Tertiary Anaconda Metamorphic Core Complex, southwestern Montana: Canadian Journal of Earth Sciences, v. 41, no. 1, p. 63-72.

Platt, J. P., Behr, W. M., and Cooper, F. J., 2015, Metamorphic core complexes: windows into the mechanics and rheology of the crust: Journal of the Geological Society, v. 172, no. 1, p. 9-27.

Poulter, G. J., 1956, Geologic map and sections of Georgetown trust area : Granite and Deer Lodge counties, Montana: Butte, MT : Montana Bureau of Mines and Geology Geologic Map GM 1, scale 1:48,000.

Ramsay, J. G., 1967, Folding and fracturing of rocks: Mc Graw Hill Book Company, v. 568.

Rey, P. F., Teyssier, C., Kruckenberg, S. C., and Whitney, D. L., 2011, Viscous collision in channel explains double domes in metamorphic core complexes: Geology, v. 39, no. 4, p. 387-390.

Schmidt, C. J., and O'Neill, J. M., 1982, Structural evolution of the southwest Montana transverse zone. In: Blake, R. (Ed.), Geologic Studies of the Cordilleran Thrust Belt 1, Rocky Mountain Association of Geologists Field Guidebook, vol. 1, p. 193-218.

Sloss, L. L., 1963, Sequences in the Cratonic Interior of North America: GSA Bulletin, v. 74, no. 2, p. 93-114.

Stipp, M., Stünitz, H., Heilbronner, R., and Schmid, S., 2002, Dynamic recrystallization of quartz: Correlation between natural and experimental conditions: Geological Society of London Special Publications, v. 200, p. 171-190.

Teyssier, C., and Whitney, D. L., 2002, Gneiss domes and orogeny: Geology, v. 30, no. 12, p. 1139-1142.

Wallace, C. A., Lidke, D. J., Elliott, J. E., Desmarais, N. R., Obradovich, J. D., Lopez, D. A., Zarske, S. E., Heise, B. A., Blaskowski, M. J., and Loen, J. S., 1992, Geologic map of the Anaconda-Pintlar wilderness and contiguous roadless area, Granite, Deer Lodge, Beaverhead, and Ravalli counties, western Montana: U.S. Geological Survey Miscellaneous Field Studies map MF-1633-C, 36 p., map scale 1:50,000.

Wallace, C. A., Lidke, D. J., and Schmidt, R. G., 1990, Faults of the central part of the Lewis and Clark line and fragmentation of the Late Cretaceous foreland basin in west-central Montana: GSA Bulletin, v. 102, no. 8, p. 1021-1037.

Wells, M. L., and Hoisch, T. D., 2008, The role of mantle delamination in widespread Late Cretaceous extension and magmatism in the Cordilleran orogen, western United States: Geological Society of America Bulletin, v. 120, no. 5-6, p. 515-530.

Wernicke, B., 1981, Low-angle normal faults in the Basin and Range Province: nappe tectonics in an extending orogen: Nature, v. 291, no. 5817, p. 645-648.

Winston, D., Smith, S. V., MacLean, J. S., and Sears, J. W., 2016, Crinkle cracks in the Proterozoic Piegan Group, Belt Supergroup, Montana and Idaho: A descriptive style of sand-filled cracks hypothetically formed by subaqueous solitary-like waves, Belt Basin: Window to Mesoproterozoic Earth, Volume 522, Geological Society of America, p. 57-69.

Wiswall, C. G., 1976, Structural styles of the southern boundary of the Sapphire tectonic block, Anaconda-Pintlar Wilderness Area, Montana: Missoula, University of Montana, M.S. thesis, 62 p., map scale 1:48,000.

Wrobel, A. J., Gans, P. B., and Womer, J. B., 2021, Late Cretaceous Crustal Shortening in the Northern Snake Range Metamorphic Core Complex: Constraints on the Structural Geometry and Magnitude of Pre-Extensional Footwall Burial: Tectonics, v. 40, no. 8.

Yonkee, A., 2005, Strain patterns within part of the Willard thrust sheet, Idaho–Utah–Wyoming thrust belt: Journal of Structural Geology, v. 27, no. 7, p. 1315-1343.

APPENDICES

APPENDIX A

U-PB GEOCHRONOLOGY DATA TABLES

							Isotope Ratios						Apparent Ages						
Analysis	U ppm	206Pb 204Pb	U/Th	206Pb* 207Pb*	± (%)	207Pb* 235U	± (%)	206Pb* 238U	± (%)	error corr.	206Pb* 238U	± (Ma)	207Pb* 235U	± (Ma)	206Pb* 207Pb*	± (Ma)	Best age (Ma)	± (Ma)	Conc (%)
Sample 21CR12: (Lat/Long: 46.009, -113.439)--NAD 1983 coordinate system																			
21CR12 Spot 101	629.680653	126427.651	2.2502185	21.0501371	1.08498908	0.05275169	1.406872911	0.00811899	0.89536671	0.63642331	52.1270472	0.46484628	52.19819244	0.71580586	55.4692781	25.8814576	52.1270472	0.46484628	93.974627
21CR12 Spot 102	401.1100122	198268.806	3.78107001	21.034907	1.09770715	0.05194858	1.52567444	0.00797861	1.05957634	0.69449701	51.2293332	0.54066274	51.42330016	0.76501694	60.4702872	26.1631267	51.2293332	0.54066274	84.7181907
21CR12 Spot 103	498.2116538	32159.161	2.13926954	21.2814078	1.39315945	0.05091474	1.660336136	0.00797713	0.89825497	0.5410079	51.2198368	0.45826177	50.42489997	0.81677426	12.8215951	NA	51.2198368	0.45826177	399.481004
21CR12 Spot 104	653.7295546	70212.3925	1.09640143	21.1257429	1.2966266	0.05130591	1.644630761	0.00793682	1.01160689	0.61509666	50.9620502	0.51350319	50.80278008	0.81496081	43.3186289	30.9844979	50.9620502	0.51350319	117.644652
21CR12 Spot 105	222.1115441	20634.7993	2.40668516	20.6455756	1.62012736	0.0546128	1.964558579	0.00834289	1.10709537	0.5635339	53.5586296	0.59048874	53.99165504	1.03299072	73.2559349	38.5842463	53.5586296	0.59048874	73.1116594
21CR12 Spot 106	380.8432636	94140.3502	1.77809169	19.3237327	2.86009016	0.05703674	3.006039302	0.00805299	0.92525115	0.30779742	51.7049879	0.47648755	56.32275257	1.64698461	257.420045	65.7352866	51.7049879	0.47648755	20.0858437
21CR12 Spot 107	693.2351064	19385.2253	2.94275671	18.7395158	1.65029628	0.05786485	1.928419163	0.00801453	0.99387077	0.51538109	51.4590511	0.5094006	57.11791778	1.07106575	301.359911	37.682176	51.4590511	0.5094006	17.0756126
21CR12 Spot 108	677.6433764	33591.7182	1.38099292	19.8526689	1.22492144	0.05729798	1.379010169	0.00835938	0.62870529	0.45591055	53.66402	0.3359881	56.57367409	0.75882111	181.542626	28.579755	53.66402	0.3359881	29.5600109
21CR12 Spot 109	1327.31254	76741.7442	1.17821415	20.9478059	0.83924554	0.0517899	1.040635973	0.00793697	0.61455182	0.59055408	50.9630476	0.31195959	51.27011844	0.52028922	65.6661635	20.0138123	50.9630476	0.31195959	77.6092967
21CR12 Spot 110	1789.600852	13718.4158	1.20065475	14.9081622	3.60045686	0.07074668	4.11272306	0.00780743	1.89077723	0.45973853	50.1344962	0.9442551	69.40776174	2.75917824	797.444989	76.5838284	50.1344962	0.9442551	6.28689087
21CR12 Spot 111	964.629975	29954.7853	2.24310949	21.3255173	1.05556142	0.05359323	1.459436745	0.00842413	1.00157447	0.68627467	54.0779953	0.5393659	53.00953761	0.75379318	4.97059125	NA	54.0779953	0.5393659	1087.95901
21CR12 Spot 112	1229.203212	75003.3696	0.47223177	20.93822	1.34689164	0.05006889	1.910172396	0.00768253	1.34766652	0.70552089	49.3354994	0.66234028	49.60731962	0.92481048	62.7631971	32.247343	49.3354994	0.66234028	78.6057781
21CR12 Spot 113	243.4501338	7685.07329	2.48473034	19.752742	1.34689974	0.05359723	1.899061797	0.00802596	1.03688078	0.54599633	51.5321332	0.53219678	53.01339742	0.98092744	120.504085	37.5067623	51.5321332	0.53219678	42.7638059
21CR12 Spot 114	391.7342508	15509.0558	2.50397079	20.8046395	1.55234742	0.05175971	2.105827315	0.00801297	1.00057373	0.4751452	51.4490462	0.51273684	51.24098065	1.05227235	41.5425547	NA	51.4490462	0.51273684	123.846611
21CR12 Spot 115	1734.372292	242058.212	1.54499358	19.9688897	1.2557904	0.05386657	1.508682054	0.00785502	0.83601367	0.55413509	50.4388936	0.42003067	53.27293082	0.78299934	182.650257	29.2573905	50.4388936	0.42003067	27.6150137
21CR12 Spot 116	673.1573222	24731.4658	2.54930515	21.4319589	1.02767944	0.05247271	1.38342065	0.00831603	0.9051142	0.65425813	53.3869245	0.48121725	51.92908447	0.70033672	NA	NA	53.3869245	0.48121725	
21CR12 Spot 117	1764.161492	69280.4173	0.87509314	20.9952894	0.67519533	0.05318497	1.18550741	0.00818835	0.97111395	0.81915469	52.5705635	0.50844408	52.61601104	0.60788091	54.6954588	16.2449198	52.5705635	0.50844408	96.1150426
21CR12 Spot 118	1861.878157	287659.043	0.82961463	20.3207294	0.63614085	0.05347673	1.054821449	0.00793845	0.84139737	0.79766805	50.9725054	0.42719018	52.89725792	0.5436868	140.991542	14.9119348	50.9725054	0.42719018	36.1528817
21CR12 Spot 119	1366.135195	300113.6	1.37845864	21.0249918	0.91507773	0.05257029	1.144411382	0.0080743	0.68715713	0.6004459	51.8413027	0.35480265	52.02321569	0.58036519	60.4084915	21.8090154	51.8413027	0.35480265	85.8179064
21CR12 Spot 120	696.5868102	40548.741	3.76106193	20.450506	0.95658947	0.05360339	1.204848504	0.00805969	0.73100853	0.60672236	51.7478496	0.37676694	53.01932775	0.6224113	110.844247	22.6011349	51.7478496	0.37676694	46.6851919
21CR12 Spot 121	1423.302108	42083.0628	2.19986287	20.7460279	1.16688004	0.05407338	1.721788478	0.00824764	1.24619181	0.72377753	52.9496355	0.65715147	53.47217162	0.89685554	76.927713	28.2269275	52.9496355	0.65715147	68.8303779
21CR12 Spot 122	572.8634989	30297.4946	1.26572106	20.879534	1.26096083	0.05257515	1.465982609	0.00809438	0.68030643	0.46406173	51.969702	0.35213191	52.02791241	0.74350903	54.7093009	30.9899301	51.969702	0.35213191	94.9924439
21CR12 Spot 123	390.026263	22144.4366	2.45329087	21.4720671	1.37472075	0.04973195	1.754666528	0.00790105	1.06289802	0.605755	50.7332802	0.53712667	49.28146455	0.84407632	NA	NA	50.7332802	0.53712667	
21CR12 Spot 124	918.1591089	84712.8109	1.6579811	21.4105242	1.09981407	0.05337988	1.284757866	0.00836622	0.65941	0.51325625	53.7077711	0.3526832	52.80390511	0.66106447	11.9509183	NA	53.7077711	0.3526832	449.402881
21CR12 Spot 125	1038.710094	78963.7134	1.72232959	20.8780214	0.70874816	0.05307815	1.012608238	0.00811117	0.72061444	0.71164189	52.077057	0.37376305	52.51302013	0.51823482	72.4611147	16.9263388	52.077057	0.37376305	71.8689702
21CR12 Spot 126	2147.670606	38150.3053	1.79361505	21.1337834	0.60250709	0.05115757	0.809968904	0.00794002	0.54107351	0.66801763	50.9825457	0.2747651	50.6594938	0.4002583	35.3780312	14.4541734	50.9825457	0.2747651	144.107922
21CR12 Spot 127	211.1167446	10590.2509	1.50005504	15.5897542	4.43147805	0.07177522	4.542544794	0.00832794	0.97176312	0.21392483	53.4630361	0.51738564	70.38265225	3.08888168	691.552097	94.6567178	53.4630361	0.51738564	7.73087615
21CR12 Spot 128	805.6453949	40332.7249	1.48526898	21.0763027	1.0639915	0.05138724	1.542463136	0.00795025	1.11165293	0.72069984	51.0479276	0.56523484	50.88132902	0.76548628	43.0190173	25.5789584	51.0479276	0.56523484	118.66363
21CR12 Spot 129	348.3469505	47291.5381	1.48003814	20.9694219	1.35337701	0.05213922	1.638910877	0.00801621	0.92339327	0.56341884	51.4697961	0.47337634	51.60729821	0.82466335	57.9750115	32.2750812	51.4697961	0.47337634	88.7792771
21CR12 Spot 130	444.0756287	50465.1009	1.48964446	19.421558	2.01996665	0.0572824	2.28908842	0.00814955	1.07343104	0.46893385	52.3224354	0.55937211	56.55870549	1.25928171	239.856302	46.5941557	52.3224354	0.55937211	21.8140758
21CR12 Spot 131	368.0186024	29764.5666	6.357277	21.0329248	1.09915177	0.05163457	1.529435825	0.00800073	1.06022867	0.69321553	51.37076	0.54248316	51.12015978	0.76249497	39.4101499	26.3842588	51.37076	0.54248316	130.34906
21CR12 Spot 132	1026.019709	89499.6243	3.70884288	20.9403362	0.90458406	0.05162979	1.428826915	0.00790892	1.10107608	0.77061544	50.7836379	0.55696976	51.11554147	0.71227398	66.6821053	21.6980478	50.7836379	0.55696976	76.1578202
21CR12 Spot 133	437.9660565	11990.4919	3.79281852	21.822027	1.39477126	0.04947268	1.803329313	0.0080885	1.0859743	0.60220521	51.9320461	0.56170311	49.03063852	0.86317593	NA	NA	51.9320461	0.56170311	
21CR12 Spot 135	981.712687	28540.7406	2.74293252	21.0295483	0.96616037	0.05208532	1.223654656	0.00807291	0.74947299	0.61248734	51.8323921	0.38691221	51.55527184	0.61511054	38.6687218	23.1293227	51.8323921	0.38691221	134.042166
21CR12 Spot 136	880.9968601	54067.7122	1.13858953	21.2908629	1.12980998	0.05291454	1.512688652	0.00825278	1.00549571	0.66470764	52.9825205	0.5305537	52.35525668	0.77190077	23.7162465	NA	52.9825205	0.5305537	223.401795
21CR12 Spot 137	584.0633488	49423.7628	1.12567403	21.1440621	1.18310378	0.05270269	1.57275976	0.00816718	1.03298265	0.65679621	52.4351759	0.53944935	52.1509302	0.79950173	39.131846	28.3767208	52.4351759	0.53944935	133.996173
21CR12 Spot 138	1823.941929	125705.919	1.11185268	21.2522906	0.66526688	0.05099003	1.081467406	0.00791178	0.85051741	0.78644757	50.8018789	0.43038076	50.4976478	0.53275812	36.0580733	15.9899325	50.8018789	0.43038076	140.889055
21CR12 Spot 139	1118.147159	246661.719	1.46915426	21.0344019	0.95504418	0.05299554	1.263114046	0.00812855	0.82654945	0.65437436	52.1881965	0.42961987	52.43336603	0.6454838	63.6657845	22.7483482	52.1881965	0.42961987	81.9721252
21CR12 Spot 140	1436.061015	63870.601	2.28828535	21.4173907	0.78337353	0.05251724	1.139702885	0.00823235	0.82531961	0.72415331	52.8518802	0.4344137	51.9720414	0.57742325	11.6018049	NA	52.8518802	0.4344137	455.548775
21CR12 Spot 141	1278.294469	67634.1468	2.86279958	21.0136752	0.9125118	0.05232691	1.538519424	0.00803409	1.23092104	0.80006857	51.5841392	0.63242632	51.78841299	0.77679676	61.2478127	21.969216	51.5841392	0.63242632	84.2220105
21CR12 Spot 142	611.5154933	84042.9386	1.4968525	21.3581959	1.35471512	0.05215286	1.730638538	0.00813185	1.0736942	0.6204035	52.209294	0.55830427	51.62046073	0.87103519	24.383936	NA	52.209294	0.55830427	214.11348
21CR12 Spot 143	865.7605451	59500.1925	1.49420872	21.1917143	0.97038715	0.05255299	1.458626851	0.00814268	1.0875992	0.74563136	52.2785479	0.56628177	52.00653247	0.73948296	39.5121456	23.2500285	52.2785479	0.56628177	132.310071
21CR12 Spot 144	1158.638663	26943.1022	2.46302085	21.2506714	0.90641397	0.05192498	1.189221491	0.00812	0.76964247	0.64718177	52.1334836	0.39962334	51.4005145	0.59605214	17.3331316	NA	52.1334836	0.39962334	300.773599
21CR12 Spot 145	1145.780067	573460.729	2.16383128	21.2889971	0.6992887	0.05164511	1.073499545	0.00800082	0.81449117	0.75872521	51.3713827	0.41675262	51.13033231	0.53529329	39.8682141	16.7188969	51.3713827	0.41675262	128.852982
21CR12 Spot 146	887.029571	45167.7568	0.89791226	20.0526405	0.93951871	0.05658057	1.332843902	0.00829685	0.89618094	0.67238252	53.2642862	0.47537775	55.88446391	0.72472619	169.664747	23.0386875	53.2642862	0.47537775	31.3938441
21CR12 Spot 147	542.461158	144439.011	2.67956405	21.4432725	1.27921985	0.05090946	1.623608146	0.0079482	0.99981738	0.61579968	51.0348618	0.50824095	50.41979887	0.79862773	21.2574541	NA	51.0348618	0.50824095	240.07984
21CR12 Spot 148	1138.231044	64673.1292	2.10499527	20.1083692	1.14677611	0.0544703	1.377804487	0.00799384	0.74540292	0.54100776	51.3267213	0.38107181	53.85444864	0.72267491	167.784809	27.0685889	51.3267213	0.38107181	30.5908036
21CR12 Spot 149	964.1279048	86719.9898	2.15545722	21.4263927	1.10397474	0.05234607	1.531401762	0.00817801	1.06012873	0.69226036	52.5044575	0.55435424	51.80689805	0.77347206	19.6396179	NA	52.5044575	0.55435424	267.339506
21CR12 Spot 150	673.9719803	2089087.6	3.13889565	20.7794156	1.19180806	0.05526822	1.447120251	0.00834445	0.82082309	0.56721139	53.5685712	0.43788132	54.62250231	0.76956841	101.103322	28.2004569	53.5685712	0.43788132	52.983987

				Isotope Ratios							Apparent Ages								
Analysis	U ppm	206Pb 204Pb	U/Th	206Pb* 207Pb*	± (%)	207Pb* 235U	± (%)	206Pb* 238U	± (%)	error corr.	206Pb* 238U	± (Ma)	207Pb* 235U	± (Ma)	206Pb* 207Pb*	± (Ma)	Best age (Ma)	± (Ma)	Conc (%)
Sample 21CR33: (Lat/Long: 46.035, -113.413)--NAD 1983 coordinate system																			
21CR33 Spot 51	156.707102	4020.66606	2.73233785	20.8939636	2.24593487	0.05212458	2.85511302	0.00863175	1.69498074	0.59366502	55.4050611	0.93508099	51.59316393	1.4362462	NA	NA	55.4050611	0.93508099	
21CR33 Spot 52	681.713742	46625.284	3.37988892	21.3502227	1.22220215	0.05190881	1.439705244	0.0081624	0.75993042	0.5278375	52.4046575	0.39662461	51.38490879	0.72138407	4.09954873	NA	52.4046575	0.39662461	1278.30307
21CR33 Spot 53	115.409326	13527.7514	3.4643723	21.9106148	3.04812183	0.04946381	3.348448684	0.00811761	1.28286382	0.38312184	52.1182472	0.66591062	49.02206131	1.60248518	NA	NA	52.1182472	0.66591062	
21CR33 Spot 54	1118.3309	108570.783	4.36599485	21.1686811	0.85628478	0.05311464	1.225957242	0.00824314	0.87724791	0.71556158	52.920874	0.46234688	52.54820452	0.62783265	35.5628097	20.4892406	52.920874	0.46234688	148.809597
21CR33 Spot 55	38.0177441	11523.9322	2.64205025	19.0016774	4.01162655	0.0677026	4.175736482	0.00963788	1.15667602	0.27699929	61.8322814	0.71178012	66.51697187	2.68855591	238.436108	92.5404962	61.8322814	0.71178012	25.932432
21CR33 Spot 56	135.325882	16007.6479	4.07427029	20.5311822	2.22218269	0.055543	2.66169994	0.00849722	1.39392111	0.52369581	54.5452001	0.75710947	54.88686111	1.42214108	69.8472219	53.9384896	54.5452001	0.75710947	78.092154
21CR33 Spot 57	697.637061	46025.3414	3.66580229	20.5494081	1.26344899	0.05527592	1.603663716	0.00835867	0.98703509	0.61548757	53.6594707	0.52743958	54.62990868	0.85292972	97.3739551	29.9131134	53.6594707	0.52743958	55.1065946
21CR33 Spot 58	522.425767	40618.2146	2.57172393	19.5540738	1.61505524	0.05824833	1.888566773	0.00838406	0.972966	0.51518751	53.821789	0.5214877	57.48593652	1.05550019	212.913762	37.5027729	53.821789	0.5214877	25.2786802
21CR33 Spot 59	219.415519	12560.961	9.56972823	20.7502185	2.15478468	0.06351385	2.416943413	0.00987349	1.05332148	0.43580726	63.3364471	0.66386978	62.52564267	1.46562204	31.6177678	NA	63.3364471	0.66386978	200.319161
21CR33 Spot 60	202.103318	3772.09077	3.71948237	10.812116	4.79689618	0.10381651	4.921099232	0.00854689	1.09681126	0.22287932	54.8627045	0.59918699	100.2931749	4.69964107	1384.56335	92.1882673	54.8627045	0.59918699	3.96245534
21CR33 Spot 61	1035.22974	57923.3801	1.70714169	20.7853584	1.02247058	0.05265415	1.410399625	0.00804164	0.97056331	0.68814774	51.632394	0.49912355	52.10411782	0.71633983	73.8603845	24.3131927	51.632394	0.49912355	69.9053957
21CR33 Spot 62	853.835588	9863.69078	3.42993996	13.1320556	3.22042041	0.08426575	3.336709179	0.00823896	0.86942372	0.26056323	52.8941648	0.45799288	82.14756864	2.63308336	1046.34253	64.9695279	52.8941648	0.45799288	5.05514812
21CR33 Spot 63	628.458039	55245.2621	3.54747181	20.3211625	0.87240871	0.15061982	1.618445551	0.02247778	1.34995628	0.8341067	143.296532	1.9130988	142.4590222	2.15119073	128.554122	20.9978412	143.296532	1.9130988	111.467862
21CR33 Spot 64	132.851648	157865.193	3.02411628	9.33155814	0.57710467	4.19391247	1.336770344	0.28607994	1.20574242	0.90198172	1621.91	17.28993	1672.830645	10.9604483	1737.30519	10.5820653	1737.30519	10.5820653	93.3578057
21CR33 Spot 66	484.037037	45412.0774	4.93414049	19.7025777	1.44993327	0.05630334	1.745520023	0.00816082	0.94538486	0.54160642	52.3945334	0.49332248	55.61801395	0.94471411	196.734013	34.0970944	52.3945334	0.49332248	26.6321683
21CR33 Spot 67	207.131588	128431.152	2.47549729	21.3225071	1.98301527	0.05468814	2.230087196	0.00854464	1.02005997	0.45740811	54.8482993	0.55711214	54.06419567	1.17414316	19.4406846	NA	54.8482993	0.55711214	282.131521
21CR33 Spot 68	609.376831	8998.29955	3.03806203	11.5209015	8.53631523	0.09673168	8.914732991	0.00829549	2.40030475	0.26925145	53.2555517	1.27302989	93.75494242	7.98390818	1305.72005	167.006187	53.2555517	1.27302989	4.07863474
21CR33 Spot 69	1123.49996	3928.81046	2.6291744	8.26923711	7.08747826	0.14757115	7.161074797	0.00918003	1.0205878	0.1425188	58.9082924	0.59847222	139.7651064	9.35065936	1904.55055	127.500072	58.9082924	0.59847222	3.09302856
21CR33 Spot 70	310.866443	24651.7002	2.58031791	21.2985963	1.81274904	0.052932	2.391900723	0.00834737	1.55537965	0.65026932	53.5872771	0.83003092	52.37208949	1.22093133	NA	NA	53.5872771	0.83003092	
21CR33 Spot 71	258.022192	76951.1012	3.66213418	21.5196227	1.61383879	0.05147509	1.806608286	0.00813149	0.8119754	0.4494474	52.2069873	0.42219599	50.9661637	0.8980327	NA	NA	52.2069873	0.42219599	
21CR33 Spot 72	484.576187	50457.7033	2.09927294	19.6946995	1.48134323	0.05686016	1.661431452	0.00823266	0.73766647	0.44399452	52.8538626	0.38829125	56.15311988	0.90761782	199.234436	34.5996846	52.8538626	0.38829125	26.5284776
21CR33 Spot 73	767.180503	66617.9591	2.9042306	20.581846	0.89961736	0.05320815	1.216162236	0.00804133	0.81572678	0.67073845	51.6304413	0.41948124	52.63836241	0.62385759	98.7550768	21.3607189	51.6304413	0.41948124	52.2813034
21CR33 Spot 74	435.137528	289987.827	8.48302353	20.3567052	0.98835692	0.06679149	1.490976506	0.00994855	1.11631431	0.74871355	63.8155341	0.70886748	65.65013758	0.94785616	133.050995	23.23011	63.8155341	0.70886748	47.9632145
21CR33 Spot 75	385.417088	29225.9393	3.85453273	20.9213312	1.57671457	0.05415119	1.820114998	0.00836943	0.896103	0.49233318	53.7282747	0.47945985	53.54712522	0.94936668	45.4703697	37.8621647	53.7282747	0.47945985	118.161069
21CR33 Spot 76	219.681378	15151.8077	2.58259088	19.7561552	2.01007529	0.05899078	2.550818672	0.00867637	1.22747717	0.48120911	55.6902455	0.68064081	58.19806247	1.44278548	162.626157	52.2964473	55.6902455	0.68064081	34.2443347
21CR33 Spot 77	458.432827	32853.1855	4.61525686	15.4243216	2.26815304	0.07474551	2.501051812	0.00847576	1.05126435	0.4203289	54.408007	0.56956503	73.19276491	1.76616992	740.271814	47.9952118	54.408007	0.56956503	7.3497337
21CR33 Spot 78	408.098649	54340.8973	3.4627938	20.1489673	1.65936164	0.05578727	2.027881851	0.00825273	1.16530545	0.57464169	52.982181	0.614874	55.12181194	1.08800632	149.106953	38.8838783	52.982181	0.614874	35.5330049
21CR33 Spot 79	675.541799	36812.2932	2.28284318	21.4683877	1.40357455	0.05121819	1.752706221	0.00809874	1.0317954	0.58868702	51.9975314	0.53435018	50.71805	0.86710261	NA	NA	51.9975314	0.53435018	
21CR33 Spot 80	105.271486	4270.39145	3.56980157	21.3712432	2.96997151	0.04961909	3.509590617	0.00836448	1.40425931	0.40012054	53.6966129	0.75090793	49.17228946	1.68462742	NA	NA	53.6966129	0.75090793	
21CR33 Spot 81	536.52413	6273.38588	4.50864649	14.6585166	1.43874384	0.07446702	1.693280626	0.00825614	0.89238634	0.52701621	53.0039738	0.47106098	72.92963072	1.19159852	787.733658	30.2327294	53.0039738	0.47106098	6.72866689
21CR33 Spot 82	418.901027	97168.3148	2.74414498	16.6374868	2.39282765	0.07169337	2.617937883	0.0087394	1.06205817	0.40568501	56.0930503	0.59315643	70.30510851	1.7782718	585.355281	51.940209	56.0930503	0.59315643	9.58273584
21CR33 Spot 83	95.4209699	5904.08251	3.37269681	17.7358373	2.62730785	0.07351275	3.192425628	0.00996756	1.3546136	0.42432111	63.9369022	0.86181707	72.02743424	2.21976436	349.648784	65.3543739	63.9369022	0.86181707	18.2860359
21CR33 Spot 84	184.672471	15109.9809	4.17637359	19.4613494	2.75571107	0.05681645	3.075587012	0.00823739	1.35978525	0.44212218	52.884088	0.71616842	56.11112767	1.67893115	196.157509	64.125558	52.884088	0.71616842	26.960012
21CR33 Spot 85	432.632705	25052.3684	1.57495267	17.2598862	2.50412047	0.0727349	2.933660603	0.00927048	1.50363394	0.51254529	59.4860202	0.89033776	71.29143035	2.01971814	487.776336	55.5956415	59.4860202	0.89033776	12.1953477
21CR33 Spot 86	419.684635	50447.9527	3.34456569	19.7846428	1.68866092	0.057392	2.152770185	0.00834932	1.33463112	0.61995987	53.599728	0.7123929	56.66395666	1.1864327	188.163816	39.3053518	53.599728	0.7123929	28.4856723
21CR33 Spot 87	264.788188	10060.7927	3.21027468	21.3543849	1.59741092	0.05168775	2.14300666	0.0083317	1.11879769	0.52206916	53.4871073	0.5959368	51.17149964	1.06943496	NA	NA	53.4871073	0.5959368	
21CR33 Spot 88	286.447136	10352.1607	2.95474998	11.190837	10.4768191	0.10274445	10.6208305	0.0085357	1.72635061	0.16254384	54.7911379	0.94187874	99.30651873	10.0481486	1367.12503	202.285047	54.7911379	0.94187874	4.00776349
21CR33 Spot 89	573.680575	42098.4533	4.38644285	20.3600444	1.30795633	0.05510919	1.773051287	0.00826229	1.19548708	0.67425409	53.0433079	0.63152413	54.46947256	0.94032495	117.644559	30.87333	53.0433079	0.63152413	45.0877698
21CR33 Spot 90	445.366107	24382.4468	3.00957464	20.4481044	1.55231412	0.05481628	2.060566499	0.00829773	1.20149102	0.58308772	53.269884	0.63739569	54.18755065	1.08730014	94.9360113	39.6494533	53.269884	0.63739569	56.1113567
21CR33 Spot 91	525.444125	43258.1195	4.01135657	18.5625661	2.43625911	0.06142509	2.625012452	0.00838896	0.94794169	0.36111893	53.8531176	0.50836974	60.52945174	1.54247478	333.288221	55.4826327	53.8531176	0.50836974	16.158122
21CR33 Spot 92	258.846497	33290.0916	2.10106302	21.7680282	1.59424644	0.05251114	2.068139899	0.00844126	1.30929585	0.63307896	54.1874466	0.70650047	51.96616265	1.04769473	NA	NA	54.1874466	0.70650047	
21CR33 Spot 93	397.014157	52915.8233	6.86597895	19.9656463	1.31795278	0.05840125	1.799212016	0.00857229	1.22423214	0.68042683	55.0250195	0.67076715	57.63265196	1.00805496	167.35996	30.7896261	55.0250195	0.67076715	32.8782461
21CR33 Spot 94	1450.76361	170202.022	5.51086642	17.7819045	1.58293385	0.09824996	1.954092867	0.0127922	1.14541622	0.58616263	81.940853	0.93262394	95.15963954	1.77503432	440.564535	35.2340542	81.940853	0.93262394	18.5990579
21CR33 Spot 95	240.660827	5647.82422	2.9525585	15.7481581	3.57636521	0.07000605	4.000372347	0.00840007	1.16846218	0.29208836	53.9241837	0.62745571	68.7051893	2.65754531	619.477024	82.5842453	53.9241837	0.62745571	8.70479156
21CR33 Spot 96	509.230577	192070.703	4.63177259	9.72091252	0.91858138	1.21644473	1.90423667	0.08647108	1.6680153	0.87594957	534.632731	8.55797869	808.14788	10.6121193	1661.3276	17.0056287	1661.3276	17.0056287	32.1810539
21CR33 Spot 97	753.830032	31523.2401	1.25546392	21.2304441	1.0883504	0.05722243	1.480910461	0.00896687	0.99413194	0.6712978	57.5465559	0.56954278	56.5011084	0.81387687	12.4202205	NA	57.5465559	0.56954278	463.329584
21CR33 Spot 98	1205.71693	4862474.68	10.2571375	11.7085027	0.61551	2.59040896	1.32073128	0.2216431	1.16853693	0.88476509	1290.55121	13.6669363	1297.929747	9.67568974	1310.13371	11.9441775	1310.13371	11.9441775	98.5053053
21CR33 Spot 100	677.381887	411383.385	4.32833688	19.1683511	1.9621401	0.06323746	2.362128578	0.00886393	1.31515718	0.55676782	56.8887925	0.74488545	62.26172324	1.42651998	274.022694	44.9844405	56.8887925	0.74488545	20.7606136

Analysis	U ppm	206Pb 204Pb	U/Th	206Pb* 207Pb*	± (%)	207Pb* 235U	± (%)	206Pb* 238U	± (%)	error corr.	206Pb* 238U	± (Ma)	207Pb* 235U	± (Ma)	206Pb* 207Pb*	± (Ma)	Best age (Ma)	± (Ma)	Conc (%)
				Isotope Ratios							Apparent Ages								
Sample 21CR35: (Lat/Long: 45.992, -113.441)--NAD 1983 coordinate system																			
21CR35 Spot 2	623.656238	96310.6726	2.64710393	21.2481747	1.08563137	0.05377057	1.445649902	0.00837153	0.95157498	0.65823335	53.7417168	0.50926698	53.1804304	0.74901698	27.961914	26.0842566	53.7417168	0.50926698	192.196131
21CR35 Spot 3	364.901169	16006.7051	3.30869958	10.4075918	3.6990531	0.11623308	4.430088124	0.00891531	2.43349038	0.5493097	57.217119	1.38621213	111.6512116	4.68403591	1519.24085	69.8358897	57.217119	1.38621213	3.76616513
21CR35 Spot 4	966.294143	2879560.57	2.48433471	18.8960472	0.907357	0.07919916	1.381665947	0.01093084	1.04197124	0.75414122	70.0823912	0.7262833	77.39173066	1.029561	309.362634	20.6464166	70.0823912	0.7262833	22.6537996
21CR35 Spot 6	128.042094	3962.57941	3.14892509	21.6854806	2.30343796	0.05474869	2.933381216	0.0094477	1.1689929	0.3985138	60.617913	0.70529782	54.12248584	1.54604985	NA	NA	60.617913	0.70529782	
21CR35 Spot 7	873.286378	60367.677	2.43957339	20.9453105	0.76115503	0.05147682	1.222169273	0.00790537	0.95530997	0.78165111	50.7608822	0.48301956	50.96783273	0.60753782	60.7202113	18.1500502	50.7608822	0.48301956	83.5979999
21CR35 Spot 9	408.081217	44719.3971	4.07058897	20.8147947	1.25469454	0.06299719	1.782894975	0.00963119	1.26622533	0.71020747	61.7895809	0.77865761	62.0322425	1.07286452	71.3828886	29.8503909	61.7895809	0.77865761	86.5607739
21CR35 Spot 10	707.595663	40994.6134	2.71634308	21.3299205	0.93525172	0.05112599	1.214727822	0.00801637	0.77412078	0.63727921	51.4707903	0.39685963	50.62898924	0.59992352	10.9491611	NA	51.4707903	0.39685963	470.088895
21CR35 Spot 12	1673.98998	41163.0544	4.30851725	19.7212737	1.16949093	0.0603829	1.627074979	0.00873527	1.130847	0.69501837	56.0666409	0.63127873	59.53198107	0.94078172	201.23106	27.1847382	56.0666409	0.63127873	27.8618226
21CR35 Spot 13	621.993728	61800.1494	2.12853141	20.9971828	0.94004167	0.05325488	1.389984541	0.00818578	1.0192476	0.73327981	52.5541422	0.53347929	52.68340781	0.71361813	58.5907787	22.5301283	52.5541422	0.53347929	89.6969513
21CR35 Spot 14	779.411132	28180.6853	2.52653836	17.9900067	1.92037329	0.06347991	2.096575195	0.00839647	0.74652376	0.3560682	53.9011544	0.40070735	62.49324026	1.2707134	405.37944	43.8599391	53.9011544	0.40070735	13.2964697
21CR35 Spot 15	275.008394	172508.298	2.83177929	21.108161	1.72504992	0.05300028	2.067645763	0.00816336	1.13987979	0.55129356	52.4107867	0.59499796	52.4379366	1.05671021	53.6659981	41.1767872	52.4107867	0.59499796	97.6610675
21CR35 Spot 16	381.269327	20635.4856	3.92949393	21.1461193	1.47897013	0.05150535	1.757406711	0.00806102	0.85665787	0.48745567	51.7563407	0.44159966	50.99538428	0.87406384	15.3718143	NA	51.7563407	0.44159966	336.696369
21CR35 Spot 17	572.885049	20164.7924	3.14069643	20.6109611	1.52142082	0.05521047	1.699303018	0.00842169	0.72623947	0.42737491	54.0623505	0.39098037	54.5669305	0.9027826	76.7541927	36.4926895	54.0623505	0.39098037	70.4356968
21CR35 Spot 18	837.397299	21943.3901	3.59260498	20.4311577	1.28842895	0.05425534	1.474587094	0.00819255	0.71581968	0.48543737	52.5974051	0.37497077	53.64744125	0.77054345	100.810099	30.5006927	52.5974051	0.37497077	52.1747381
21CR35 Spot 19	189.957676	5364.87156	3.27442306	21.0504585	2.58521239	0.05132099	4.145083804	0.00836086	0.96728379	0.23335687	53.6734755	0.51701946	50.81733758	2.05458197	NA	NA	53.6734755	0.51701946	
21CR35 Spot 20	253.016159	18455.3302	2.73951033	18.4685911	2.99471472	0.05952026	3.215687897	0.00813192	0.96660391	0.30059009	52.2097141	0.50262301	58.70561094	1.8342555	332.404018	69.5574512	52.2097141	0.50262301	15.7067037
21CR35 Spot 21	339.646433	68637.6764	2.90628142	21.2623443	1.26416796	0.05170039	1.571016734	0.00805125	0.93263721	0.59365199	51.6938991	0.48018865	51.18370204	0.78417421	27.3810896	NA	51.6938991	0.48018865	188.794164
21CR35 Spot 22	323.022115	166706.908	3.6934013	21.2505384	1.58055528	0.05594992	2.007850274	0.00868468	1.23824103	0.61669988	55.7433253	0.68726101	55.27822571	1.08023328	35.1439634	NA	55.7433253	0.68726101	158.614225
21CR35 Spot 23	327.834848	72372.8375	3.01129405	20.0542647	1.90258187	0.05399254	2.021998708	0.00792651	0.67480069	0.33372954	50.8961216	0.34209514	53.39429828	1.05173707	166.962729	44.5361118	50.8961216	0.34209514	30.4835227
21CR35 Spot 24	879.787023	42676.4742	3.21613518	20.7361875	1.33103119	0.05340577	2.283851508	0.00813221	1.85200031	0.810911	52.2115993	0.96305368	52.82885875	1.1756835	80.8944546	31.7316524	52.2115993	0.96305368	64.5428659
21CR35 Spot 25	678.067455	11364.4008	3.18773136	14.6140255	3.16139159	0.07805602	3.378006711	0.00847344	1.06035835	0.3139006	54.3931892	0.57433627	76.31561827	2.48345533	831.876024	66.8766428	54.3931892	0.57433627	6.53861725
21CR35 Spot 26	789.674806	50111.1668	2.03137736	19.5283313	1.23914787	0.05733282	1.462962919	0.00820847	0.77249906	0.52803735	52.6992107	0.40544142	56.60712933	0.8054803	225.232483	28.7053689	52.6992107	0.40544142	23.3976956
21CR35 Spot 27	445.211961	11707.0824	2.59376889	20.6701116	1.28959839	0.05208487	1.694263115	0.0080581	1.09635382	0.64709773	51.7377066	0.56495817	51.55484521	0.8516707	43.0645982	30.8867158	51.7377066	0.56495817	120.139764
21CR35 Spot 28	343.76524	74747.1554	3.5634937	21.5398073	1.77020254	0.05203749	1.997603175	0.00820562	0.92559192	0.46335125	52.6809726	0.48562383	51.50911422	1.00328519	NA	NA	52.6809726	0.48562383	
21CR35 Spot 29	174.826313	8037.70883	2.97783383	20.7147313	1.77626236	0.05443452	2.160623764	0.00854529	1.21244263	0.56115398	54.852469	0.66223326	53.81999495	1.13256728	8.06923813	NA	54.852469	0.66223326	679.77259
21CR35 Spot 30	1287.01296	29148.0407	2.64595024	21.3786477	1.16223349	0.05119422	1.467159314	0.00806528	0.89265141	0.6084216	51.7835757	0.46039518	50.69489486	0.725513	-0.4580664	NA	51.7835757	0.46039518	-11304.819
21CR35 Spot 31	219.521972	13303.7488	3.39427028	22.0236912	1.86003824	0.04958574	2.557621832	0.00817297	1.22318203	0.47824976	52.4722019	0.63922545	49.14002258	1.22688912	NA	NA	52.4722019	0.63922545	
21CR35 Spot 32	554.337412	41264.2824	2.3188348	14.4746947	5.05411924	0.12319749	6.043148345	0.01308474	3.30647659	0.5471447	83.8025744	2.75297971	117.9667135	6.73046787	877.268252	104.769213	83.8025744	2.75297971	9.55267379
21CR35 Spot 33	1570.38452	167274.811	64.7901272	15.2868872	1.88255163	0.1420834	2.086186374	0.01587797	0.89871881	0.43079507	101.55188	0.90551473	134.8978416	2.63529668	771.087296	39.6348712	101.55188	0.90551473	13.1699589
21CR35 Spot 34	782.192539	36560.6958	1.43828616	20.9334567	1.2511211	0.05197784	1.518613435	0.00801138	0.78822361	0.51904164	51.4389205	0.40384036	51.45154058	0.76188403	52.0237267	30.9603688	51.4389205	0.40384036	98.8758856
21CR35 Spot 35	524.326234	52836.8277	3.33999095	19.5121924	1.56318934	0.06125004	1.961357469	0.00877277	1.18451224	0.60392471	56.3062645	0.6640503	60.3619768	1.14941135	224.365347	36.1503277	56.3062645	0.6640503	25.0957936
21CR35 Spot 36	2425.69891	3193.38939	2.03260909	7.43392139	7.10407377	0.15362944	7.155473363	0.00860458	0.84963683	0.11873943	55.2314249	0.46726197	145.1114463	9.67585929	2091.06869	125.070601	55.2314249	0.46726197	2.64130131
21CR35 Spot 37	486.990387	15580.738	3.85585845	20.3831576	1.05565364	0.05545849	1.360447207	0.0084133	0.85746641	0.63028275	54.0087356	0.46117219	54.80556711	0.72583613	89.7947825	25.0240812	54.0087356	0.46117219	60.1468527
21CR35 Spot 38	699.349382	27811.4658	4.91063137	21.1422278	1.09384027	0.06322215	1.330380623	0.00986706	0.74559033	0.56043385	63.2954231	0.46961528	62.24710944	0.80325084	22.1392356	NA	63.2954231	0.46961528	285.897057
21CR35 Spot 39	828.197325	35094.2424	3.44190811	19.9120419	1.33883847	0.05509984	1.697660756	0.00807552	0.95498197	0.56252816	51.8490934	0.49316356	54.46047718	0.90019737	170.878241	32.747895	51.8490934	0.49316356	30.3427126
21CR35 Spot 40	1251.25661	166178.026	2.36115683	20.4226257	1.13058119	0.05630735	1.390519147	0.00840862	0.80946477	0.58213134	53.9788366	0.43511541	55.62186467	0.75263038	126.990163	26.5929462	53.9788366	0.43511541	42.5063134
21CR35 Spot 41	141.4634	25098.4644	2.95013595	21.9878411	2.01979345	0.06043489	2.342431188	0.00983244	1.18547217	0.50608623	63.074407	0.7440834	59.58176401	1.35550386	NA	NA	63.074407	0.7440834	
21CR35 Spot 42	466.936637	20189.7509	2.74689193	20.9164884	1.60002343	0.05161088	1.979126161	0.00800579	1.05566691	0.53340051	51.4031726	0.54048852	51.0972791	0.98625605	36.7487107	NA	51.4031726	0.54048852	139.877486
21CR35 Spot 43	1455.9455	39454.3546	1.98298129	21.062314	1.12576992	0.05253916	1.437680698	0.00814522	0.89345983	0.62145915	52.2948008	0.465343	51.99319021	0.72868075	38.0895256	26.9638287	52.2948008	0.465343	137.29444
21CR35 Spot 44	347.503873	56712.7574	3.77200876	20.8127366	1.23706484	0.05608241	1.608536569	0.00857017	1.02733972	0.63867974	55.0114942	0.56275036	55.40561383	0.86734083	72.4741597	29.434833	55.0114942	0.56275036	75.9049769
21CR35 Spot 45	1854.47743	159068.212	11.0674603	20.7241491	0.81382674	0.06487814	1.137486347	0.00983751	0.79384024	0.6978899	63.1067712	0.49852283	63.8273566	0.70367912	90.9333602	19.2976665	63.1067712	0.49852283	69.3989215
21CR35 Spot 46	703.333375	14340.6634	1.43007582	20.0951477	1.61706307	0.05355845	1.942213614	0.0080349	1.07280966	0.5523644	51.5893026	0.55124633	52.97602319	1.00252781	116.170055	38.2084157	51.5893026	0.55124633	44.4084344
21CR35 Spot 47	783.652681	18278.5899	2.76740641	17.3454672	1.65273222	0.06648618	2.026216037	0.00855002	1.16131326	0.57314385	54.8826884	0.63465449	65.35950137	1.28260246	468.068055	36.767926	54.8826884	0.63465449	11.7253651
21CR35 Spot 48	846.147997	34425.5656	1.48917567	20.7672322	0.98469654	0.05354019	1.43492357	0.00820233	1.02622859	0.71517997	52.6599579	0.53821027	52.95841868	0.740436	66.4896482	23.8827023	52.6599579	0.53821027	79.2002354
21CR35 Spot 49	261.947249	16532.1359	10.8488155	20.9243443	1.90825975	0.0637781	2.355938346	0.00994298	1.37744137	0.58466783	63.7800262	0.87420072	62.77790002	1.43421626	24.7487778	NA	63.7800262	0.87420072	257.709801
21CR35 Spot 50	177.207166	23334.186	5.11703795	19.1312127	2.36657901	0.06106253	2.824358293	0.00864517	1.4773486	0.52307407	55.4908115	0.81627444	60.1825622	1.65037989	251.086061	55.3772566	55.4908115	0.81627444	22.1003154

APPENDIX B

U-PB GEOCHRONOLOGY CONCORDIA PLOTS

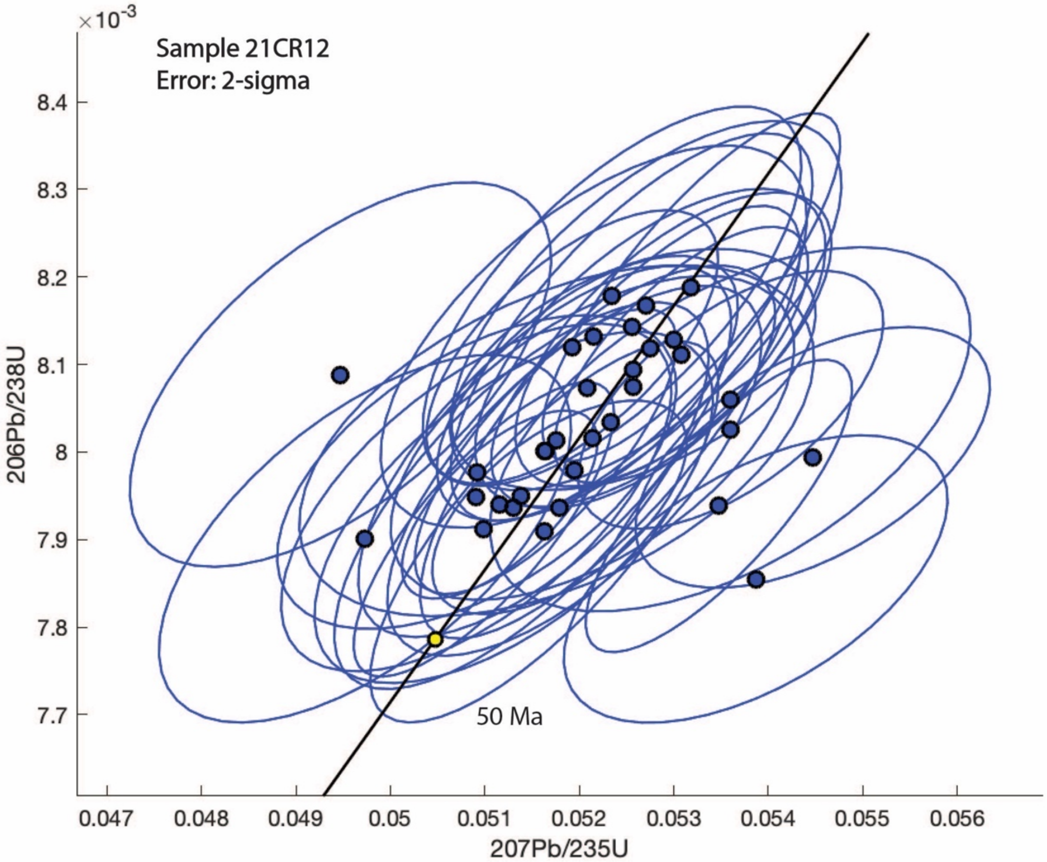
×10^-3
Sample 21CR12
Error: 2-sigma
8.4
8.3
8.2
8.1
8
7.9
7.8
7.7
206Pb/238U
50 Ma
0.047
0.048
0.049
0.05
0.051
0.052
0.053
0.054
0.055
0.056
207Pb/235U

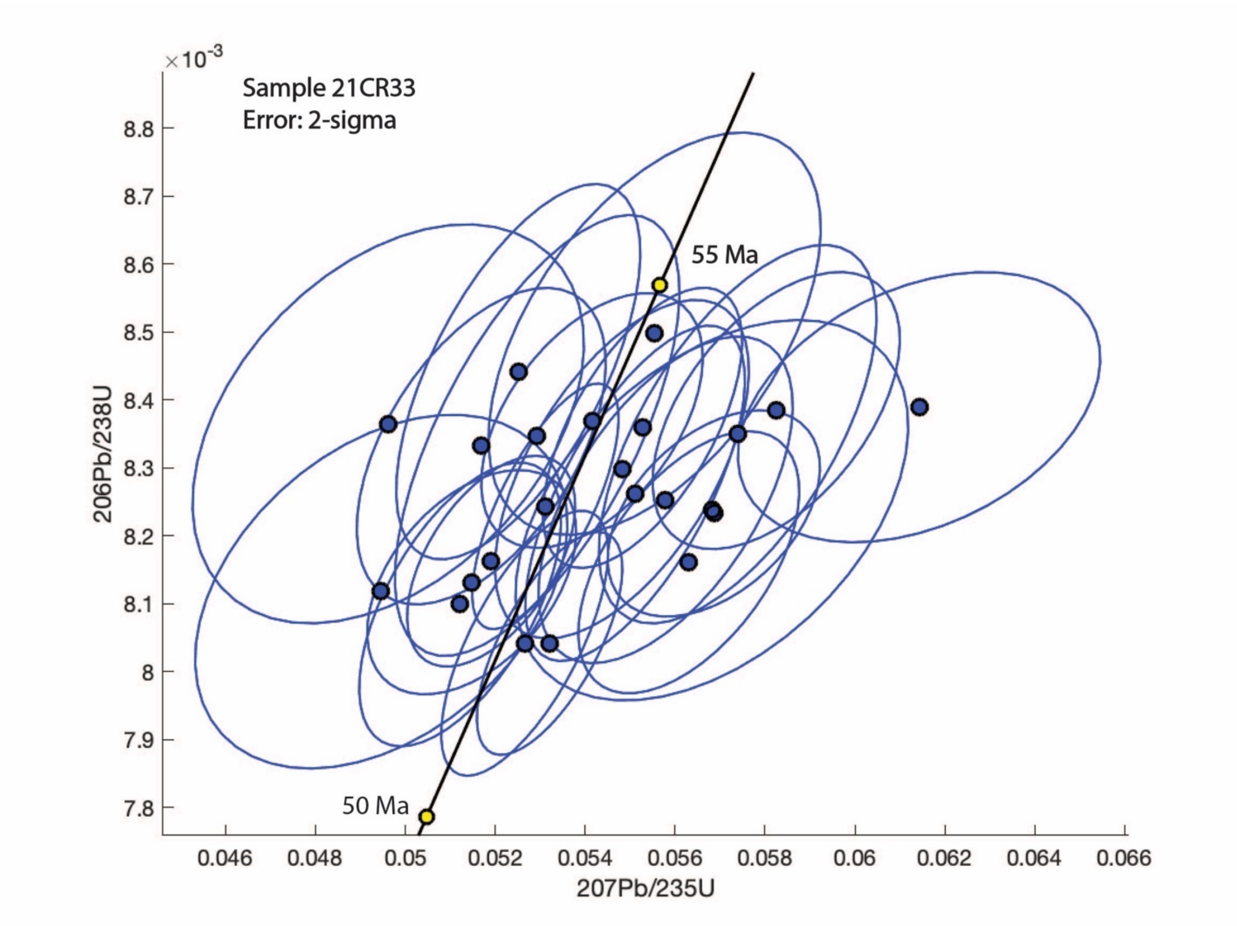
×10^-3
Sample 21CR33
Error: 2-sigma
55 Ma
50 Ma
206Pb/238U
207Pb/235U
8.8
8.7
8.6
8.5
8.4
8.3
8.2
8.1
8
7.9
7.8
0.046
0.048
0.05
0.052
0.054
0.056
0.058
0.06
0.062
0.064
0.066

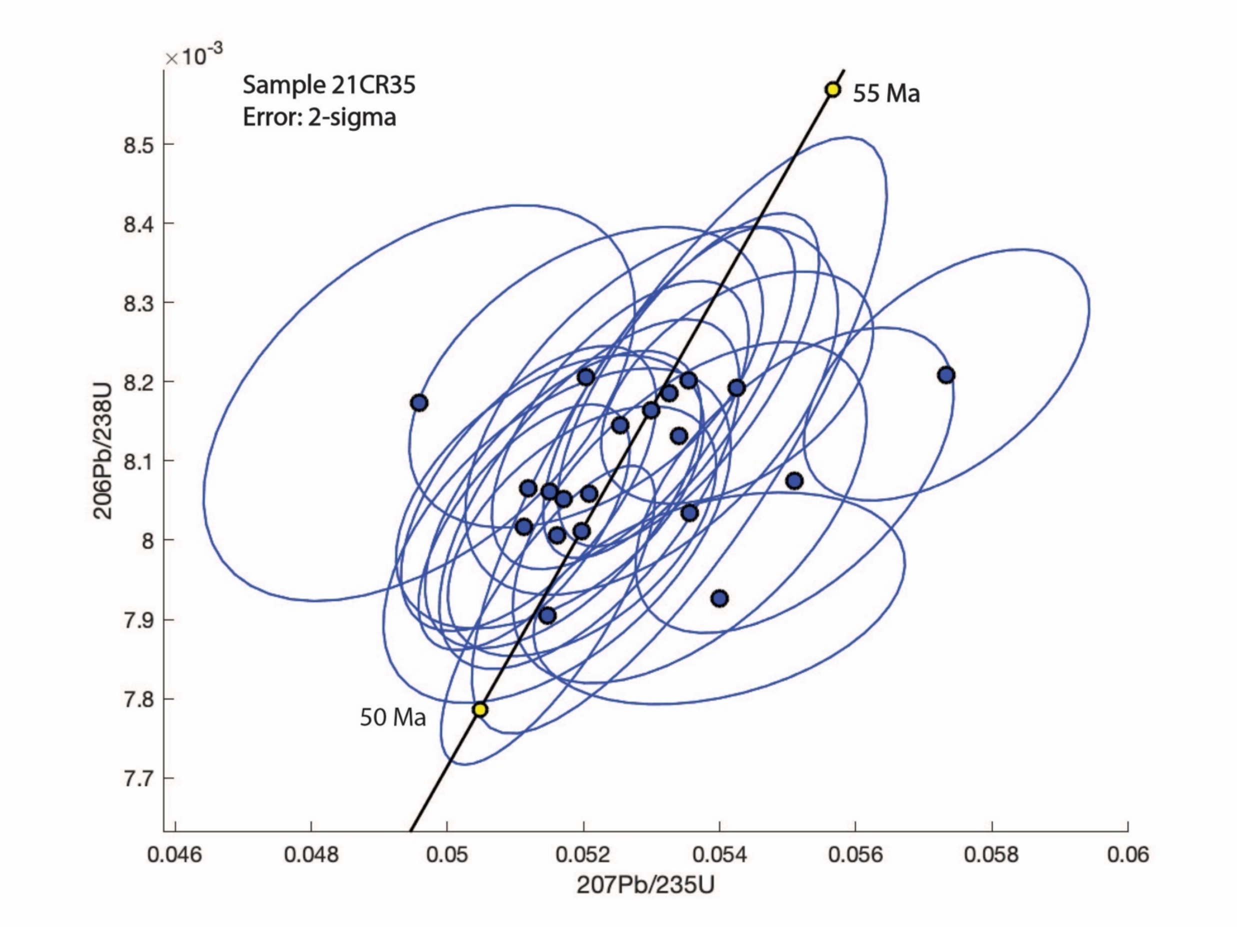
Sample 21CR35
Error: 2-sigma
55 Ma
50 Ma
×10⁻³
8.5
8.4
8.3
8.2
8.1
8
7.9
7.8
7.7
206Pb/238U
0.046
0.048
0.05
0.052
0.054
0.056
0.058
0.06
207Pb/235U